

# A *Herschel*\* AND APEX CENSUS OF THE REDDEST SOURCES IN ORION: SEARCHING FOR THE YOUNGEST PROTOSTARS\*\*

AMELIA M. STUTZ<sup>3</sup>, JOHN J. TOBIN<sup>4</sup>, THOMAS STANKE<sup>5</sup>, S. THOMAS MEGEATH<sup>6</sup>, WILLIAM J. FISCHER<sup>6</sup>, THOMAS ROBITAILLE<sup>3</sup>, THOMAS HENNING<sup>3</sup>, BABAR ALI<sup>7</sup>, JAMES DI FRANCESCO<sup>8</sup>, ELISE FURLAN<sup>9,7</sup>, LEE HARTMANN<sup>10</sup>, MAYRA OSORIO<sup>11</sup>, THOMAS L. WILSON<sup>12</sup>, LORI ALLEN<sup>9</sup>, OLIVER KRAUSE<sup>3</sup>, P. MANOJ<sup>13</sup>

*Draft version February 7, 2013*

## ABSTRACT

We perform a census of the reddest, and potentially youngest, protostars in the Orion molecular clouds using data obtained with the PACS instrument onboard the *Herschel* Space Observatory and the LABOCA and SABOCA instruments on APEX as part of the *Herschel* Orion Protostar Survey (HOPS). A total of 55 new protostar candidates are detected at 70  $\mu\text{m}$  and 160  $\mu\text{m}$  that are either too faint ( $m_{24} > 7$  mag) to be reliably classified as protostars or undetected in the *Spitzer*/MIPS 24  $\mu\text{m}$  band. We find that the 11 reddest protostar candidates with  $\log \lambda F_{\lambda} 70 / \lambda F_{\lambda} 24 > 1.65$  are free of contamination and can thus be reliably explained as protostars. The remaining 44 sources have less extreme 70/24 colors, fainter 70  $\mu\text{m}$  fluxes, and higher levels of contamination. Taking the previously known sample of *Spitzer* protostars and the new sample together, we find 18 sources that have  $\log \lambda F_{\lambda} 70 / \lambda F_{\lambda} 24 > 1.65$ ; we name these sources "PACS Bright Red sources", or PBRs. Our analysis reveals that the PBRs sample is composed of Class 0 like sources characterized by very red SEDs ( $T_{\text{bol}} < 45$  K) and large values of sub-millimeter fluxes ( $L_{\text{submm}}/L_{\text{bol}} > 0.6\%$ ). Modified black-body fits to the SEDs provide lower limits to the envelope masses of 0.2  $M_{\odot}$  to 2  $M_{\odot}$  and luminosities of 0.7  $L_{\odot}$  to 10  $L_{\odot}$ . Based on these properties, and a comparison of the SEDs with radiative transfer models of protostars, we conclude that the PBRs are most likely extreme Class 0 objects distinguished by higher than typical envelope densities and hence, high mass infall rates.

*Subject headings:* ISM: Clouds, Stars: Formation

## 1. INTRODUCTION

The onset of the star formation process is broadly characterized by a dense collapsing cloud envelope surrounding the nascent protostar. The dense cloud or protostellar envelope is opaque to radiation shortward of about

$\sim 10$   $\mu\text{m}$  and most of the radiation from these sources is reprocessed and emitted in the far-infrared (FIR). Furthermore, bipolar outflows from the protostar and disk carve out envelope cavities that enable a fraction of the protostellar luminosity to escape in the form of scattered light emission, predominantly at wavelengths shortward of  $\sim 10$   $\mu\text{m}$ .

The earliest phase of protostellar evolution, the Class 0 phase (André et al. 1993), is thought to be short compared to the Class I phase (Lada 1987), with combined Class 0 and Class I lifetimes of  $\sim 0.5$  Myr (Evans et al. 2009); these estimates assume a constant star formation rate and a typical age for Class II objects (pre-main sequence stars with disks) of 2 Myr. At the onset of collapse and immediately before the Class 0 phase, protostars may go through a brief first hydrostatic core (FHSC) phase where the forming protostellar object becomes opaque to its own radiation for the first time (Larson 1969). The FHSC are expected to be very low-luminosity and deeply embedded. A population of very low luminosity protostars (VeLLOs) were also recently identified by *Spitzer* (e.g., Dunham et al. 2008; Bourke et al. 2006), defined to have model-estimated internal source luminosities of less than 0.1  $L_{\odot}$ . VeLLOs, however, appear more evolved than FHSCs with features consistent with Class 0 and I protostars. Furthermore, while several FHSC candidates have been identified recently (e.g., see Enoch et al. 2010; Chen et al. 2010; Pineda et al. 2011; Pezzuto et al. 2012), it has proven observationally difficult to distinguish such sources from the young Class 0 protostellar phase. It is therefore currently difficult to identify the very earliest phases of the formation of a protostar.

\* *Herschel* is an ESA space observatory with science instruments provided by European-led Principal Investigator consortia and with important participation from NASA.

\*\*Based (in part) on observations collected at the European Organisation for Astronomical Research in the Southern Hemisphere, Chile, proposals E-284.C-0515, E-086.C-0848, E-088.C-0994, and E-090.C-0894.

<sup>3</sup> Max Planck Institute for Astronomy, Königstuhl 17, D-69117 Heidelberg, Germany; stutz@mpia.de

<sup>4</sup> Hubble Fellow, National Radio Astronomy Observatory, Charlottesville, VA 22903, USA

<sup>5</sup> ESO, Karl-Schwarzschild-Strasse 2, 85748 Garching bei München, Germany

<sup>6</sup> Department of Physics and Astronomy, University of Toledo, 2801 W. Bancroft St., Toledo, OH 43606, USA

<sup>7</sup> NHSC/IPAC/Caltech, 770 S. Wilson Avenue, Pasadena, CA 91125, USA

<sup>8</sup> National Research Council of Canada, Herzberg Institute of Astrophysics, 5071 West Saanich Rd., Victoria, BC, V9E 2E7, Canada; University of Victoria, Department of Physics and Astronomy, PO Box 3055, STN CSC, Victoria, BC, V8W 3P6, Canada

<sup>9</sup> National Optical Astronomy Observatory, 950 N. Cherry Avenue, Tucson, AZ, 85719, USA

<sup>10</sup> Department of Astronomy, University of Michigan, 830 Dennison Building, 500 Church Street, Ann Arbor, MI 48109, USA

<sup>11</sup> Instituto de Astrofísica de Andalucía, CSIC, Camino Bajo de Huétor 50, E-18008, Granada, Spain

<sup>12</sup> Naval Research Laboratory, 4555 Overlook Ave. SW, Washington, DC 20375, USA

<sup>13</sup> Department of Physics and Astronomy, 500 Wilson Blvd., University of Rochester, Rochester, NY 14627, USA

Before the launch of *Spitzer* and the advent of extremely sensitive mid-infrared surveys, conventional wisdom held that a Class 0 protostar should not be detectable at wavelengths shortward of  $10\ \mu\text{m}$  due to the envelope opacity (Williams & Cieza 2011). Outflows, however, can carve out cavities in the protostellar envelopes at a very early age and are expected to widen with evolution (Arce & Sargent 2006). Indeed, recent simulations have shown that even the extremely young FHSC sources may be capable of driving outflows (Commerçon et al. 2012; Price et al. 2012). Regardless of evolutionary state, the outflow cavities enable near-to mid-infrared light from the protostar and disk to escape and scatter off dust grains in the cavity or on the cavity walls. This phenomenon has been well-known for Class I sources (Kenyon et al. 1993; Padgett et al. 1999), but Class 0 protostars were only well-detected in the mid-infrared with *Spitzer* (Noriega-Crespo et al. 2004; Jørgensen et al. 2007; Stutz et al. 2008). The scattered light from Class 0 protostars is often brightest at wavelengths  $\sim 3.6\ \mu\text{m}$  or  $4.5\ \mu\text{m}$  due to the dense envelope obscuration at shorter wavelengths (e.g., Whitney et al. 2003a; Tobin et al. 2007).

The combination of results from recent space-based and ground-based surveys have resulted in well-sampled spectral energy distributions from the near-infrared to the (sub)millimeter for large samples of protostellar objects (e.g., Hatchell et al. 2007; Enoch et al. 2009; Launhardt et al. 2010; Fischer et al. 2010; Launhardt et al. 2012). These SEDs are dominated by scattered light between  $\sim 1\ \mu\text{m}$  and  $10\ \mu\text{m}$ , optically thick thermal dust emission from  $\sim 10$  to  $\sim 160\ \mu\text{m}$ , and optically thin dust emission at wavelengths longward of  $\sim 160\ \mu\text{m}$ . Radiative transfer models of protostellar collapse have become increasingly important to interpret these data since these can account for the varying temperature and density profiles in the envelopes surrounding the protostar (e.g., Whitney et al. 2003a,b).

The large number of free model parameters — such as the combination of outflow cavities, rotationally flattened envelopes (Ulrich 1976; Cassen & Moosman 1981; Terebey et al. 1984), and varying viewing angles — can however make the best-fit SED model parameters highly degenerate (e.g., Whitney et al. 2003a). For example, sources viewed at nearly edge-on orientations can be substantially more obscured than sources at the same evolutionary state viewed from a less extreme vantage point. Thus, standard diagnostics such as bolometric temperature or mid-infrared spectral index can yield vastly different results depending on the source inclination (e.g., Dunham et al. 2010). Radiative transfer models can help break some of these degeneracies but ambiguities can remain as to whether a source has a very dense envelope or if it is simply viewed edge-on.

While much has been learned about the Class 0 phase from observations and modeling, there are relatively few Class 0 objects present in nearby star-forming clouds and globules (Evans et al. 2009) compared to the numbers of Class I and Class II sources. One of the principal goals of recent star formation surveys has been to understand the evolution of protostellar sources. Young & Evans (2005) generated models for the smooth luminosity evolution of protostellar objects that will become  $0.3\ M_{\odot}$ ,  $1\ M_{\odot}$  and  $3\ M_{\odot}$  stars. These models, however, over

predict the luminosities of most protostars located in nearby star-forming regions, a fact that is taken as evidence for episodic accretion (Kenyon & Hartmann 1990; Evans et al. 2009; Dunham et al. 2010). However, Offner & McKee (2011) show that the observed luminosity functions of protostars can be explained through a dependence of the mass accretion rate on the instantaneous and final mass of the protostar. The low resolutions and sensitivities of previous FIR instrumentation have made the detection of protostars in more distant and richer star-forming regions difficult and subject to substantial confusion. Thus, studies of protostellar evolution have been limited to combining all known Class 0 protostars from the nearby regions into a single analysis (e.g., Myers et al. 1998; Evans et al. 2009) to achieve a more robust sample size.

The advent of the *Herschel Space Observatory* (Pilbratt et al. 2010) has tremendously improved resolution and sensitivity to FIR radiation, where protostars emit the bulk of their energy. These improvements enable the study of protostellar populations to be extended to more distant, richer regions of star formation that have more statistically significant samples of protostars in the Class 0 and I phases (e.g., Ragan et al. 2012). The *Herschel* Orion Protostar Survey (HOPS) is a *Herschel* Open Time Key Programme (OTKP) (e.g., Stanke et al. 2010; Fischer et al. 2010; Ali et al. 2010; Manoj et al. 2012) targeting  $\sim 300$  of the *Spitzer* identified Orion protostars with PACS (Poglitsch et al. 2010)  $70\ \mu\text{m}$  and  $160\ \mu\text{m}$  photometry and PACS spectroscopy ( $53\ \mu\text{m}$  to  $200\ \mu\text{m}$ ; Manoj et al. 2012) for a subset of 30 protostars. Orion is the richest star-forming region within 500 pc of the Sun (Megeath et al. 2012), at a distance of  $\sim 420$  pc (average value; Menten et al. 2007; Hirota et al. 2007; Sandstrom et al. 2007). The large sample of protostars in Orion enables studies of protostellar evolution to be carried out for a single star forming complex where all protostars lie at nearly the same distance with a statistically significant sample, comparable to or larger than all the nearby regions combined. The large sample may also enable short timescale phenomena (e.g., Fischer et al. 2012) to be detected such as brief periods of high envelope infall rate in the earliest phases of star formation. Even with the increased numbers of protostars in Orion, however, it is unclear if we would expect to detect FHSCs given the faintness of these sources and short lifetimes of less than 10 kyr (Commerçon et al. 2012).

The PACS imaging of the HOPS program has the potential to identify protostars that were not detected by *Spitzer* due to a combination of opacity of the envelope and/or confusion with nearby sources. Indeed, the PACS  $70\ \mu\text{m}$  band of *Herschel* is ideal for detecting such protostars, with the highest angular resolution, limiting the blending of sources. Also, the lower opacity relative to MIPS  $24\ \mu\text{m}$  allows the reprocessed warm inner envelope radiation to escape. Finally, and most importantly, a  $70\ \mu\text{m}$  point source is strong evidence for an embedded protostar because external heating cannot raise temperatures high enough to emit at this wavelength. Thus, some cores in sub-millimeter surveys that were previously identified as starless may in reality be protostellar.

Using *Herschel*, we have serendipitously identified a sample of  $70\ \mu\text{m}$  point sources that were not identified in the previous *Spitzer* protostar sample (Megeath et al.

2012). Furthermore, we have identified a subset of these that have the reddest  $70\ \mu\text{m}$  to  $24\ \mu\text{m}$  colors of all protostars in the combined Orion sample. These sources may have the densest envelopes and are possibly the youngest detected Orion protostars and we name them “PACS Bright Red sources” or PBRs.

We will describe the methodology of identifying these sources and classify them as either being protostellar, extragalactic contamination, or spurious detections coincident with extended emission. We will discuss the observations and data reduction in § 2, the source finding and classification methods in § 3, the observed properties of the new sources in § 4, the PBRs in § 5, the comparison of the cold PBRs to models in § 6, some relevant model degeneracies in § 7, and, finally, our results in § 8. Throughout this work, all positions are given in the J2000 system.

## 2. OBSERVATIONS, DATA REDUCTION, AND PHOTOMETRY

In this work, we present *Herschel* scan map observations of a sub-set of the HOPS fields containing candidate protostars. In addition, we present a subset of our APEX LABOCA and SABOCA observations of these fields. A summary of the HOPS *Herschel* PACS survey observations is presented in Tables 1 and 2. Here we discuss the observations, data processing, and photometry extraction.

### 2.1. *Herschel* PACS

The PACS data were acquired simultaneously at  $70\ \mu\text{m}$  and  $160\ \mu\text{m}$  over  $5' \times 5'$  or  $8' \times 8'$  field sizes. The field sizes and centers were chosen to maximize observing efficiency by allowing each field to include as many of the target *Spitzer*-selected protostars (Megeath et al. 2012) as possible while minimizing redundant coverage. The observations were acquired at medium scan speed ( $20''\ \text{sec}^{-1}$ ), and are composed of two orthogonal scans with homogeneous coverage.

The PACS data were reduced using the *Herschel* Interactive Processing Environment (HIPE) version 8.0 build 248 and 9.0 build 215. We used a custom built pipeline to process data from their raw form (the so-called Level 0 data) to fully calibrated time lines (Level 1) just prior to the map-making step. Our pipeline uses the same processing steps as described by Poglitsch et al. (2010) but also include the following additions and modifications. First, we used a spatial redundancy based algorithm to identify and mask cosmic ray hits. Second, we mitigated instrument cross-talk artifacts by masking (flagging as unusable) detector array columns affected by cross-talk noise. This technique is effective but at the expense of loss of signal from the affected detector array columns. Third, we used the “FM6” version of the instrument responsivity, which has a direct bearing on the absolute calibration of the final mosaics.

The Level 1 data were processed with “Scanamorphos” (Roussel 2012) version 14.0. The final maps were produced using the *galactic* option and included the turn-around (non-zero acceleration) data. The final map pixel scales used in this work are  $1.0''/\text{pix}$  at  $70\ \mu\text{m}$  and  $2.0''/\text{pix}$  at  $160\ \mu\text{m}$ .

The photometry was performed in the following fashion. We first derived customized aperture corrections

to the  $70\ \mu\text{m}$  and  $160\ \mu\text{m}$  data using the *Herschel* Science Center (HSC) provided observations of Vesta (to be discussed in more detail in Fischer et al., in preparation). At  $70\ \mu\text{m}$ , we used radii of sizes  $9.6''$ ,  $9.6''$ , and  $19.2''$ , for the aperture and sky annuli respectively. For these parameters we derived an aperture correction of 0.7331, where the measured flux in the aperture is divided by this correction to obtain a total point-source flux. At  $160\ \mu\text{m}$ , we used aperture radii of  $12.8''$ ,  $12.8''$ , and  $25.6''$ , for the aperture and sky annuli respectively. Similarly, we derived an aperture correction of 0.6602. The encircled energy fractions provided by the `photApertureCorrectionPointSource` task in HIPE do not account for the effect of applying an inner sky annulus that is close to the size of the source aperture and small compare to the PSF. Our apertures therefore account for 3–4% of the source flux that is removed. Furthermore, our adopted aperture sizes are smaller than the PACS instrument team recommendation but were chosen to minimize contribution from nebulosity (extended, non point-like emission) often surrounding the protostars in Orion. Given the complex structure in the images and at times crowded fields, our aperture photometry may suffer from blending and contamination. The photometric errors include a 10% systematic error floor added in quadrature to the standard photometric uncertainties. These errors represent systematic uncertainties in our photometry and aperture correction, as well as the overall calibration uncertainty of PACS. We note that the reported HSC point-source calibration uncertainties for PACS are  $\sim 3\%$  at  $70\ \mu\text{m}$  and  $\sim 5\%$  at  $160\ \mu\text{m}$ , and were derived from isolated photometric standards. Therefore, our final uncertainties are conservative.

We include the  $100\ \mu\text{m}$  Gould Belt Survey (GBS; e.g., André et al. 2010; Könyves et al. 2010; Men'shchikov et al. 2010, see also Schneider et al., in preparation, for Orion B, and Roy et al., in preparation, and Polychroni et al., in preparation, for Orion A) data of Orion in this work for the PBRs analysis. Given the sparsely covered SEDs of our sources, these data provide important information regarding the shape of the thermal SED of cold envelope sources. These data were acquired using the medium scan speed ( $20''\ \text{sec}^{-1}$ ) and cover an area much larger than the HOPS fields. These data were processed in a similar way to the HOPS processing described above. Following the above  $70\ \mu\text{m}$  and  $160\ \mu\text{m}$  analysis, we used aperture radii of sizes  $9.6''$ ,  $9.6''$ , and  $19.2''$ , for the aperture and sky annuli respectively. For these parameters, we derived an aperture correction of 0.6944. As with the  $70\ \mu\text{m}$  and  $160\ \mu\text{m}$  data, we also assume a conservative 10% systematic error floor.

### 2.2. APEX SABOCA and LABOCA

We obtained sub-millimeter (smm) continuum maps using the LABOCA and SABOCA bolometer arrays on the APEX telescope. LABOCA (Siringo et al. 2009) is a  $\sim 250$  bolometer array operating at  $870\ \mu\text{m}$ , with a spatial resolution of  $\sim 19''$  at FWHM. We used a combination of spiral and straight on-the-fly scans to recover extended emission. Data reduction was done with the BOA software (Schuller et al. 2012) following standard procedures, including iterative source modeling. SABOCA (Siringo et al. 2010) is a 37 bolometer array operating at  $350\ \mu\text{m}$ , with a resolution of  $\sim 7.3''$  FWHM. The observ-

ing and data reduction procedures were similar to those used for LABOCA. For both cameras, observations were carried out between 2009 November and 2012 June, and are still ongoing to complete our Submillimeter Orion Survey. Conditions were generally fair over the course of our observing campaign. The observations will be summarized in more detail by Stanke et al. 2013, in preparation.

The beam sizes of the final reduced maps are  $7.34''$  and  $19.0''$  FWHM for the SABOCA and LABOCA observations, respectively. The photometry was extracted in the same way for both wavelengths. When possible, if there was a strong source detection, we re-centered using the  $70\ \mu\text{m}$  catalog source coordinates. Given the contributions of flux due to surrounding cold material, such as filaments and other extended envelope structure, it is likely that a single photometric measure can suffer from large systematic effects. We have measured source fluxes in three ways:

1. We measured the source peak flux per beam.
2. We measured source flux over an aperture with radius equal to the FWHM at the corresponding wavelength ( $r = 7.34''$  and  $19.0''$  at  $350\ \mu\text{m}$  and  $870\ \mu\text{m}$ , respectively), using a sky annulus with inner and outer radii equal to  $[1.5, 2.0] \times \text{FWHM}$ , corresponding to  $11.0''$  and  $14.7''$  at  $350\ \mu\text{m}$ , and  $28.5''$  and  $38.0''$  at  $870\ \mu\text{m}$ .
3. We measured the flux over the same aperture size as the previous method without any sky subtraction. In the case that a source was not strongly detected and we were not able to re-center, the  $70\ \mu\text{m}$  catalog source coordinates was used, along with method 3, and the photometric point was flagged as an upper limit. By re-centering whenever possible, we accounted for possible pointing offsets between data-sets, which can be significant. The calibration error dominated the error budget for well detected sources; we therefore adopted a flux error equal to 20% and 40% of the measured flux for LABOCA and SABOCA respectively. The photometric fluxes are presented in Table 5.

### 2.3. *Spitzer* IRAC and MIPS

The IRAC and MIPS imaging and photometry presented here are taken from the 9 degree<sup>2</sup> survey of the Orion A and B cloud obtained during the cryogenic *Spitzer* mission. The data analysis, extraction of the IRAC  $3.6\ \mu\text{m}$ ,  $4.5\ \mu\text{m}$ ,  $5.8\ \mu\text{m}$ , and  $8\ \mu\text{m}$  and MIPS  $24\ \mu\text{m}$  photometry, and the compilation of a point source catalog containing the combined 2MASS, IRAC and MIPS photometry are described in Megeath et al. (2012); also see Kryukova et al. (2012) for a detailed description of the MIPS  $24\ \mu\text{m}$  photometry. In total, 298405 point sources were detected in at least one of the *Spitzer* bands, and 8021 sources were detected at  $24\ \mu\text{m}$  with uncertainties  $\leq 0.25\ \text{mag}$ . The *Spitzer* images used in this work are taken from the mosaics generated from the Orion Survey data using Cluster Grinder for the IRAC data (Gutermuth et al. 2009) and the MIPS instrument team’s Data Analysis Tool for the  $24\ \mu\text{m}$  data (Gordon et al. 2005). The MIPS data are saturated toward the Orion Nebula and parts in the NGC2024 region; we exclude these saturated regions from our analysis.

The identification of protostars with the *Spitzer* data was based primarily on the presence of a flat or rising spectral energy distributions between  $4.5\ \mu\text{m}$  and  $24\ \mu\text{m}$

(Kryukova et al. 2012; Megeath et al. 2012). In addition, Megeath et al. identified objects which have point source detections only at  $24\ \mu\text{m}$  but which also showed other indicators of protostellar nature such as the presence of jets in the IRAC bands. To minimize contamination from galaxies, the *Spitzer*-identified protostars were required to have  $24\ \mu\text{m}$  magnitudes brighter than 7th magnitude; fainter than 7 magnitudes, the number of background galaxies begins to dominate over the number of embedded sources (Kryukova et al. 2012). Given the imposed  $24\ \mu\text{m}$  magnitude threshold, the faintest and reddest protostars may not be included in the *Spitzer* sample. In total, the Megeath et al. (2012) catalog contains 488 protostars. Of these, 428 are classified as bona fide protostars, 50 are faint candidate protostars, and 10 are red candidate protostars. The faint candidate protostars are sources with  $24\ \mu\text{m}$  magnitudes higher than 7.0. The red protostars are sources that are only detected as a point source at  $24\ \mu\text{m}$  and are thus not classifiable. Due to their location within high extinction regions and/or association with jets or compact scattered light nebulae in the IRAC bands, they have been included in the catalog. (Indeed, this last category was added to the Megeath et al. catalog after the *Herschel* data revealed that a relatively large number of such sources would likely be confirmed as protostars.) In addition, the Megeath et al. catalog identified 2992 objects as pre-main sequence stars with disks. In what follows, we use the protostar catalog of 488 *Spitzer* sources to catalog previously identified sources in the HOPS images.

In contrast to the full Megeath et al. catalog, the HOPS protostar sample represents a sub-set of that catalog. The HOPS sample is not a complete representation of the Megeath et al. catalog because the HOPS survey targeted a smaller area than the *Spitzer* survey and required an extrapolated  $70\ \mu\text{m}$  flux that would be detectable with PACS. However, the HOPS catalog represents our best pre-*Herschel* knowledge of the protostellar content within the HOPS fields. The HOPS sample is therefore the best one against which to benchmark and compare the new *Herschel* protostellar candidates. The HOPS sample constitutes  $\sim 300$  previously identified *Spitzer* protostars all having *Herschel* PACS  $70\ \mu\text{m}$  detections. Of these,  $\sim 250$  HOPS sources have PACS  $160\ \mu\text{m}$  detections. This sample will be analyzed in detail in Fischer et al., in preparation.

In contrast to the full Megeath et al. catalog, the HOPS protostar sample are those protostars specifically targeted by the HOPS program. The majority of the HOPS sample consists of *Spitzer*-identified protostars with  $24\ \mu\text{m}$  detections; hence, protostars in regions that are saturated in the  $24\ \mu\text{m}$  images of Orion, namely the brightest regions of the Orion Nebula and NGC2024, are not included. These protostars were also required to have a predicted  $70\ \mu\text{m}$  flux  $> 20\ \text{mJy}$  as extrapolated from their  $3\ \mu\text{m}$  to  $24\ \mu\text{m}$  SEDs. In addition, protostar candidates with only  $24\ \mu\text{m}$  detections were included if there was independent information of their protostellar nature. The HOPS sample represents the best pre-*Herschel* catalog of protostars that were expected to be detected with *Herschel*/PACS and were not found in bright nebulous regions. There are  $\sim 300$  protostars in the HOPS catalog which have been detected at  $70\ \mu\text{m}$  and  $\sim 250$  protostars detected at  $160\ \mu\text{m}$ . The uncertainty in their absolute

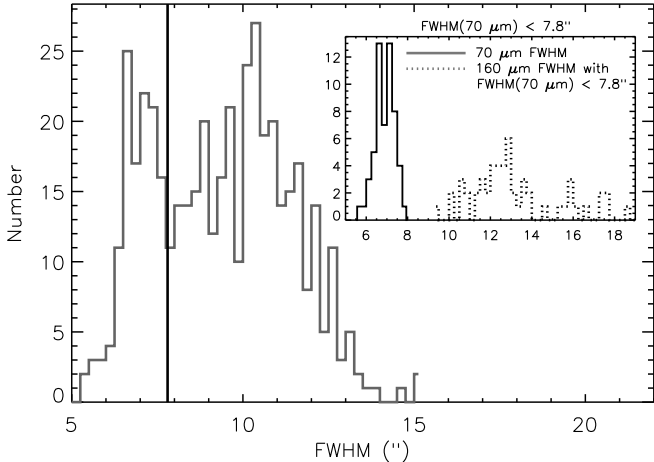


FIG. 1.— Frequency of  $70\ \mu\text{m}$  FWHM values for all sources detected in our HOPS images that have not been previously identified in the *Spitzer* catalog. The black line shows our adopted  $7.8''$  FWHM threshold, above which we reject all sources. *Inset*: Same as above for the subset of sources with both  $\text{FWHM}(70\ \mu\text{m}) < 7.8''$  and  $160\ \mu\text{m}$  detections (see § 3). The dotted histogram indicates the  $160\ \mu\text{m}$  FWHM distribution.

number of protostars is due to the ongoing process of eliminating contamination from the sample.

### 3. IDENTIFICATION OF NEW CANDIDATE *Herschel* PROTOSTARS

To find protostars which were not reliably identified with *Spitzer*, we must first isolate a sample of sources that are detected in the PACS  $70\ \mu\text{m}$  band but are either fainter than 7.0 magnitudes or undetected in MIPS  $24\ \mu\text{m}$  waveband. To identify such sources in each HOPS field we first generate a  $70\ \mu\text{m}$  source catalog using the PhotVis tool (Gutermuth et al. 2008). The PhotVis tool uses a sunken Gaussian filtering to extract sources that are of order the size of the Gaussian FWHM, an input parameter. We choose this parameter to be the size of the  $70\ \mu\text{m}$  PSF FWHM, or  $5''$ . PhotVis also requires a SNR threshold as input; we adopt a low value of 7 to balance the recovery of as many candidate sources as possible while still rejecting noise spikes.

Furthermore, we must reject unreliable sources near the edges of maps where the lower coverage causes elevated noise levels. The Scanamorphos scan map image cubes include a weight map for each field. Within Scanamorphos, the weight map is computed over the same projection as the sky map, and is defined as one over the variance in the white noise (Roussel 2012). Each weight map is then normalized by the average map value (Roussel 2012). We find that for the HOPS data-set, weight map values of  $\sim 20$  are confined to the outer higher noise edges of our scan maps. We therefore use the weight maps to reject edge sources from the catalog at this phase of the analysis. We accomplish this by requiring that the mean value of the weight map in a  $9 \times 9$  pixel area centered on the candidate source have a value of at least 20. For reference, all HOPS  $70\ \mu\text{m}$  scan maps have weight map values greater than 60 over most of the map areas.

The resulting preliminary source catalog includes all sources in the  $70\ \mu\text{m}$  images, i.e., previously identified *Spitzer* sources, new candidate protostars, nebulosity, and other undesirable features and artifacts in the im-

ages. We then cross-correlate this PACS  $70\ \mu\text{m}$  preliminary catalog with the existing *Spitzer* catalog to eliminate all previously identified protostars in each field that are brighter than the previously adopted  $24\ \mu\text{m}$  cutoff of 7 mag (Megeath et al. 2012). Therefore our sample includes by definition only sources that are faint or undetected in the previous *Spitzer* catalog.

To identify previous source detections, we require that a source be matched to within a positional offset of  $8''$  when cross-correlated with the *Spitzer* catalog. This threshold is conservatively large compared to the *Spitzer* astrometry and is meant to encompass two main sources of astrometric error. First, it is possible that the absolute coordinates of a source may shift as function of wavelength (although this effect is expected to be relatively small) since different wavelengths may trace different material near the protostars. Second, the *Herschel* pointing accuracy, which is of order  $\sim 2''$  ( $1\sigma$ ), dominates the positional accuracy for most sources when comparing the *Spitzer* catalog source coordinates to the *Herschel*  $70\ \mu\text{m}$  coordinates. To match coordinates robustly, we therefore adopt a conservatively large  $8''$  threshold. We find that inspection of the matched sources by eye shows that this threshold works well and provides a low rate of mismatched or duplicate sources.

Our final goal is to obtain a sample of previously unidentified and uncharacterized *Herschel* protostar candidates. These sources should be characterized by a point-like appearance at  $70\ \mu\text{m}$ . Therefore, after rejecting all *Spitzer* protostars as described above, we next apply a simple FWHM (or apparent size) filter to the remaining  $70\ \mu\text{m}$  sources. The distribution of  $70\ \mu\text{m}$  azimuthally averaged FWHM values is shown in Figure 1 as the solid black histogram. We find a clear peak in the distribution at low FWHM values, indicating a population of point-like sources. Based on this distribution, we adopt a FWHM threshold of  $7.8''$ , meant to select  $70\ \mu\text{m}$  point-sources. We find 127 sources that fulfill the criteria listed here: 85 of these have  $24\ \mu\text{m}$  detections while 42 do not.

In a further step, we then require that all  $70\ \mu\text{m}$  sources also have a  $160\ \mu\text{m}$  detection and not upper limits. The  $70\ \mu\text{m}$  FWHM distribution of this sub-set of sources is shown in the inset of Figure 1 along with the corresponding  $160\ \mu\text{m}$  FWHM distribution. Our final sample consists of 55 candidate *Herschel* protostars with both  $70\ \mu\text{m}$  and  $160\ \mu\text{m}$  detections. Of these, 34 have *Spitzer*  $24\ \mu\text{m}$  detections fainter than 7.0 magnitudes and 21 do not have any  $24\ \mu\text{m}$  detection.

#### 3.1. *Spitzer* non-detections

A search for newly detected protostars using *Herschel* requires us to determine upper limits at  $24\ \mu\text{m}$  for those sources that are not detected by *Spitzer*. To determine these limits, we adapt the method developed by Megeath et al. to assess the spatially varying completeness of the *Spitzer* Orion Survey data. The completeness of the  $24\ \mu\text{m}$  data depends strongly on the presence of nebulosity and point source crowding. To account for these factors, we measure the fluctuations of the  $24\ \mu\text{m}$  signal in an annulus centered on the position of the *Herschel* point-source using the the root median square deviation, or RMEDSQ (see Equation 1 of Megeath et al. 2012). We then use the results from the artificial star tests (see

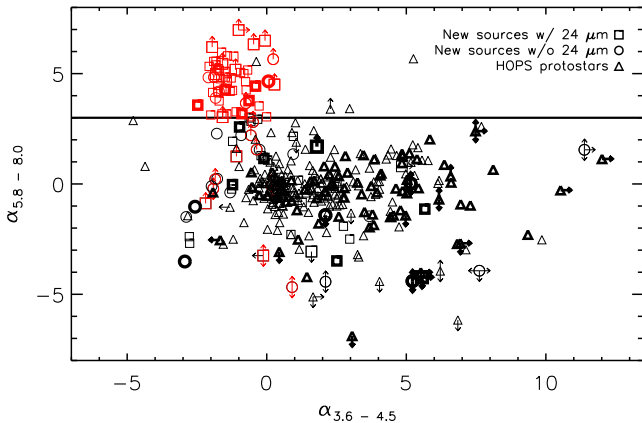


FIG. 2.— IRAC color indices  $\alpha_{3.6-4.5}$  and  $\alpha_{5.8-8.0}$  for sources detected in at least one IRAC band. The *Herschel* protostar candidate sample is shown as squares (sources with  $24\ \mu\text{m}$  detections) and circles (sources without  $24\ \mu\text{m}$  detections), while the HOPS protostar sample is shown as triangles. Thick bold points are sources with robust  $870\ \mu\text{m}$  detections. Candidate protostars with  $\alpha_{5.8-8.0} > 3.0$  or upper limits consistent with this threshold are flagged as possible extragalactic contamination and highlighted in red. Note that some candidate protostars have both  $\alpha_{5.8-8.0} > 3.0$  and a robust  $870\ \mu\text{m}$  detection; these sources are not considered extragalactic contamination.

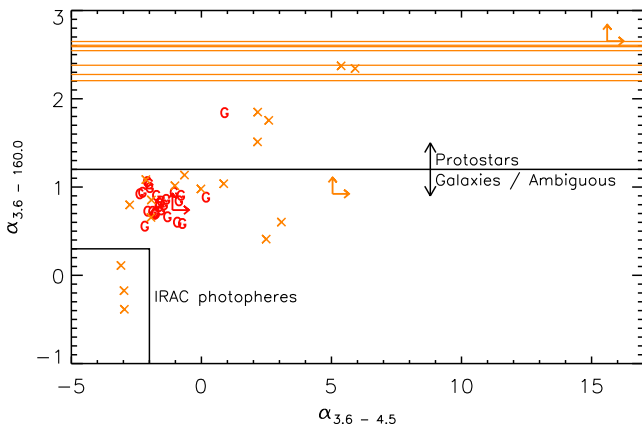


FIG. 3.— IRAC and PACS  $160\ \mu\text{m}$  color indices  $\alpha_{3.6-4.5}$  and  $\alpha_{3.6-160}$  for the candidate protostar sample. Sources previously characterized as extragalactic based on their  $\alpha_{5.8-8.0} > 3$  index (or limit) are indicated in red with a “G”. Sources with  $\alpha_{5.8-8.0} < 3$  are indicated in orange. The orange lines indicate the lower limits of  $\alpha_{3.6-160}$  for sources with no IRAC detections. Sources with  $\alpha_{3.6-160} > 1.2$  are considered highly probable protostars, while other sources are flagged as described in the text.

Appendix of Megeath et al. 2012) to determine the magnitude at which 90% of the point sources would be detected for the observed level of fluctuations. We convert this magnitude into a flux density to obtain  $24\ \mu\text{m}$  upper limits.

Several of the identified protostars show IRAC emission but are not included in the Megeath et al. point source catalog because they are spatially extended. To obtain homogeneously extracted IRAC fluxes for the entire sample of sources, we measure fluxes using an aper-

ture of 2 pixels, with a sky annulus of 2 to 6 pixels, corresponding to aperture radii of  $2.44''$ ,  $2.44''$ , and  $7.33''$ , respectively, with a pixel scale of  $1.22''\ \text{pixel}^{-1}$ . We use the PACS  $70\ \mu\text{m}$  source coordinates as starting guesses, and attempt to re-center at each IRAC wavelength. If the re-centering fails, as for sources with no IRAC detections, we take the integrated flux in that aperture at the original PACS  $70\ \mu\text{m}$  source coordinate to be the upper limit. The aperture corrections and photometric zero-points are those given by Kryukova et al.

### 3.2. Contamination in the sample

Galaxies often exhibit infrared colors similar to those of young stellar objects (YSOs) due to the presence of dust and hydrocarbons in the galaxies (Stern et al. 2005). Extensive work has been done towards characterizing the extragalactic “contamination” in *Spitzer* surveys of star-forming regions and mitigating it through photometric criteria designed to separate galaxies from bona fide YSOs (Gutermuth et al. 2009, 2008; Harvey et al. 2007). These authors show that star-forming galaxies can be distinguished from YSOs by the galaxies’ stellar-like emission in the IRAC  $3.6\ \mu\text{m}$  and  $4.5\ \mu\text{m}$  bands and their bright polycyclic aromatic hydrocarbon (PAH) emission in the IRAC  $5.8\ \mu\text{m}$  and  $8.0\ \mu\text{m}$  bands (Gutermuth et al. 2009, 2008; Winston et al. 2007; Stern et al. 2005). However, we note that some Active Galactic Nuclei (AGN) dominated galaxies may not exhibit PAH emission; therefore an analysis based only on the IRAC colors may not capture all possible sources of contamination (Robitaille et al. 2008).

To analyze the IRAC colors of our sample, we define  $\alpha = d\log(\lambda F_\lambda)/d\log(\lambda)$ . In Figure 2, we plot  $\alpha_{5.8-8}$  vs.  $\alpha_{3.6-4.5}$  for the sample of new *Herschel* sources with coverage in all four of the *Spitzer*/IRAC bands and detections in at least one band, compared to the HOPS protostar sample. This color index is relatively insensitive to reddening since the extinction in the  $5.8\ \mu\text{m}$  and  $8\ \mu\text{m}$  bands of IRAC are very similar (e.g., Flaherty et al. 2007; Gutermuth et al. 2008). Figure 2 shows a cluster of sources with high values of  $\alpha_{5.8-8}$  (i.e.,  $\alpha_{5.8-8} \geq 3$ ; solid horizontal line) yet  $\alpha_{3.6-4.5}$  values of an SED that is declining or flat with increasing wavelength. These sources show the characteristics of star-forming galaxies with bright PAH emission (resulting in high values of  $\alpha_{5.8-8}$ ) but values of  $\alpha_{3.6-4.5}$  that are dominated by starlight. In our adopted scheme,  $\alpha_{5.8-8} \geq 3$  corresponds to a color of  $[5.8] - [8] \geq 2.17$ ; this threshold is higher than the  $[5.8] - [8] \geq 1$  threshold used by Gutermuth et al. (2008) to isolate galaxies and thus ensures that most protostellar candidates will be less likely to be miss-identified extragalactic sources (Allen et al. 2004; Megeath et al. 2004). We identify the cluster of sources with  $\alpha_{5.8-8} \geq 3$  and  $\alpha_{3.6-4.5} \leq 0.5$  as likely extragalactic contamination. We note that nebular contamination of the photometry can cause PAH-like  $\alpha_{5.8-8}$  values, and thus may cause us to over-estimate the extragalactic contamination. Of the 55 sources identified here as protostellar candidates we flag 23 as possible extragalactic contamination based on this criteria. However, other sources of contamination, such as AGN lacking PAH emission, may remain in our sample.

Inspection of the SEDs of the remaining 32 sources show a range of SED slopes and shapes. It is possi-

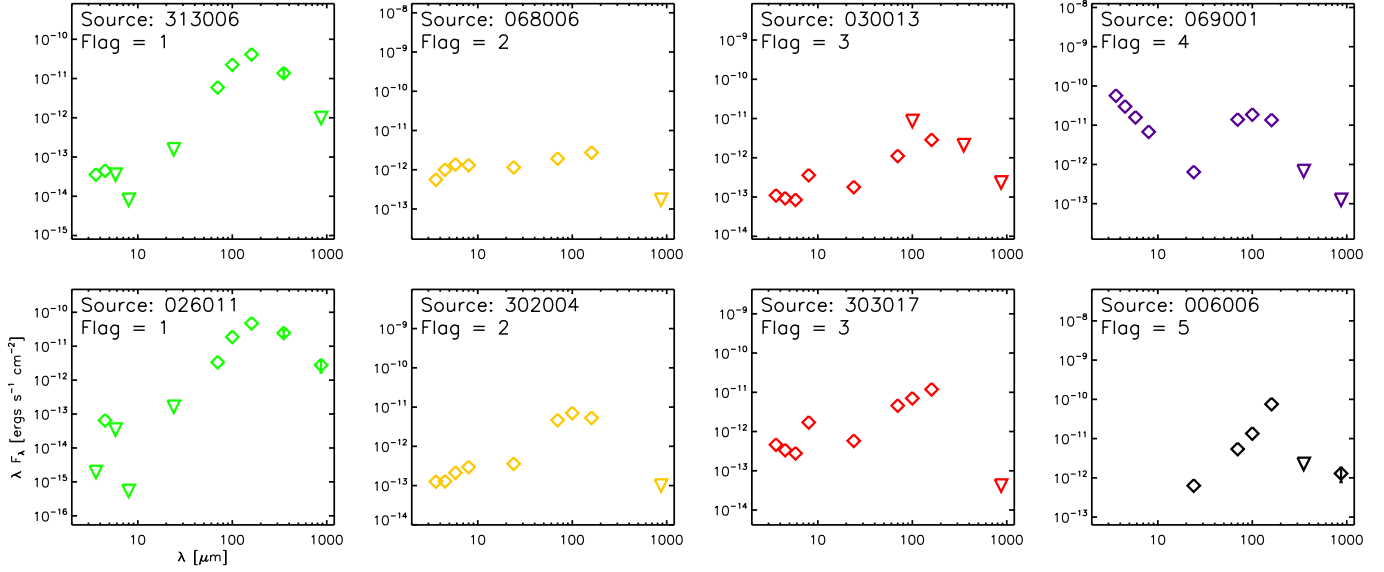


FIG. 4.— Example SEDs for each of the 5 categories described in § 3.2: green SEDs (flag = 1) are considered to be reliable protostar candidates, yellow SEDs (flag = 2) are less likely to be protostellar, red SEDs (flag = 3) are considered extragalactic contamination based on the  $8\ \mu\text{m}$  PAH feature, the purple SED (flag = 4) is an example of one of 3 sources that may be explained as transition disks, and, finally, the black SED (flag = 5) is unclassifiable due to the lack of IRAC coverage. Errors are smaller than the size of the points, except for the  $350\ \mu\text{m}$  and  $870\ \mu\text{m}$  points; upper limits are indicated with triangles.

ble that such sources may also be extragalactic contamination by AGN, for example. To address this, we further refine the analysis presented above by analyzing the  $3.6\ \mu\text{m}$  to  $160\ \mu\text{m}$  SED shapes with the spectral index  $\alpha_{3.6-160}$ . As illustrated in Figure 3, the sources flagged as extragalactic based on the  $\alpha_{5.8-8}$  index (red points) generally have  $\alpha_{3.6-160} \lesssim 1.2$ . We therefore calibrate the  $\alpha_{3.6-160}$  relative the reliable extragalactic candidates with robust IRAC detections and expect that extragalactic sources will have  $\alpha_{3.6-160} \lesssim 1.2$ . Using this criterion, we refine our source classification as follows. All sources with  $\alpha_{3.6-160} > 1.2$  (and  $\alpha_{5.8-8} < 3$  when IRAC detections exist) are flagged as high probability protostars (flag = 1 in Table 3). Sources having values of  $0.5 \lesssim \alpha_{3.6-160} \lesssim 1.2$  but that originally classified as candidate protostars based on a low value of  $\alpha_{5.8-8}$  are flagged as less likely to be of a protostellar nature (flag = 2 in Table 3). Furthermore, by definition, sources originally classified as extragalactic based on their PAH signature at  $8\ \mu\text{m}$  remain classified as such (flag = 3 in Table 3). Sources with  $\alpha_{3.6-160} < 0.3$  and  $\alpha_{3.6-4.5} \sim -3$  are flagged as “other” (flag = 4 in Table 3) since their SEDs are consistent with a stellar photosphere at shorter wavelengths. Finally, one source has no IRAC coverage and therefore is flagged with a value of 5. In Figure 4 we show example SEDs of each category.

Only one source (313006) originally flagged as extragalactic based on its  $\alpha_{5.8-8}$  limit (non-detection at  $5.8\ \mu\text{m}$  and  $8\ \mu\text{m}$ ) was revised to a highly probable protostar (see Figure 3 and top left panel of Figure 4). In addition, as we note above, we find three sources with SEDs that we label “other” (flag value = 4) which are inconsistent with the categories described above. Source 069001 (see Figure 4, top right panel) was previously characterized by Fang et al. (2009) as a K7 star with a debris disk, with a very poorly constrained age of  $\sim 0.06^{+4.66}_{-0.03}$  Myr. These authors only include data up to  $24\ \mu\text{m}$ . The SED

we observe with *Herschel* may be consistent with a transition disk but not a debris disk. The remaining two sources in this category have similar SEDs as that of 069001; while a transition disk explanation for all three sources may appear likely depending on the age of the sources, we cannot currently rule out other possibilities. Nevertheless, all of these sources have SEDs consistent with a stellar photosphere in the IRAC bands, and hence these are likely to be fully formed stars surrounded by circumstellar dust.

Interestingly, we find that the most reliable SED classification criterion by far is that of sources that have neither IRAC nor MIPS  $24\ \mu\text{m}$  detections. Of these, we find that all 6 sources have strong sub-millimeter detections and reside in dense and filamentary environments. This finding points to the critical importance of obtaining high resolution sub-millimeter data to constrain the properties of such sources. In the following text, we include all 55 *Herschel*-detected sources in our analysis and figures.

#### 4. *Herschel* PROTOSTAR CANDIDATES

We present the *Herschel* protostar candidate catalog in Table 3. Here we include the PACS  $70\ \mu\text{m}$  coordinates and flux measurements at  $24\ \mu\text{m}$ ,  $70\ \mu\text{m}$ , and  $160\ \mu\text{m}$ . We indicate which sources are flagged as reliable protostellar candidates and which are likely contamination, based on the results from the previous section. We also indicate if the sources have a robust  $870\ \mu\text{m}$  detection. Furthermore, we present the values of  $L_{\text{bol}}$  and  $T_{\text{bol}}$  and their corresponding estimated statistical errors (see discussion in § 5.1). In Figure 5, we show the  $70\ \mu\text{m}$  flux distributions for the sample compared to the distribution of HOPS protostars. The majority of the new candidate protostars have  $70\ \mu\text{m}$  fluxes that are lower than the previously identified *Spitzer* HOPS sample; this is not surprising since the new candidate protostar sample is

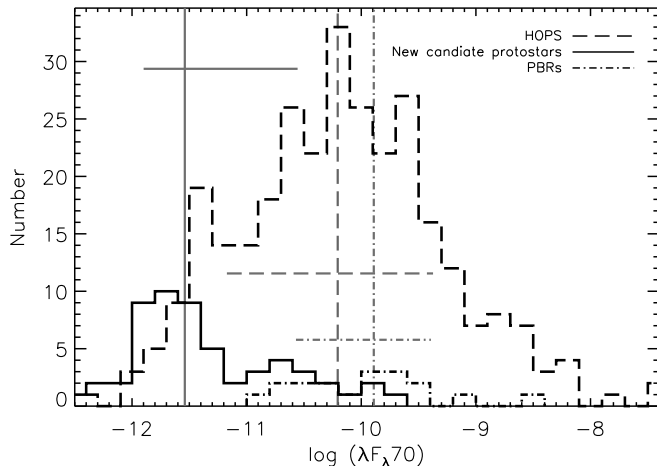


FIG. 5.— Distributions of  $70\ \mu\text{m}$  fluxes for the HOPS protostars (dashed histogram), new candidate protostars (solid histogram), and the 18 reddest sources drawn from both combined samples (dot-dashed histogram). The corresponding grey lines indicate the median flux values (vertical lines) and the 68% interval (horizontal lines).

selected to be faint or undetected at  $24\ \mu\text{m}$ . Furthermore, the peak at low  $70\ \mu\text{m}$  flux values is dominated by extragalactic contamination, as discussed above.

In Figure 6, we show the MIPS  $24\ \mu\text{m}$ , PACS  $70\ \mu\text{m}$ , and PACS  $160\ \mu\text{m}$  colors of the new *Herschel* sources compared to the HOPS sample of  $70\ \mu\text{m}$  detected protostars. The top panel shows the  $70\ \mu\text{m}$  flux vs. the  $\log(\lambda F_{\lambda 70}/\lambda F_{\lambda 24})$  color (henceforth 70/24 color), while the bottom panel shows the  $\log(\lambda F_{\lambda 160}/\lambda F_{\lambda 70})$  color (henceforth 160/70 color) vs. the 70/24 color, for our sample of new protostar candidates compared to the colors of the *Spitzer*-identified HOPS sample. The *Spitzer*  $24\ \mu\text{m}$  7 magnitude limit, imposed on the HOPS sample for a reliable protostellar identification, is apparent in the top panel as the diagonal line approximately separating the new protostellar candidates at fainter  $70\ \mu\text{m}$  fluxes and redder 70/24 colors from the population of *Spitzer*-identified HOPS sources.

For comparison, in the top panel of Figure 6, we also show the fluxes and colors of presumably typical and well-studied Class 0 sources: VLA1632–243 (J. Green and DIGIT team, private communication, 2012, and Green et al., in prep.), IRAS16293 (Evans et al. 2009), B335 (Stutz et al. 2008; Launhardt et al. 2012), CB68 (Launhardt et al. 2012), and CB244 (Stutz et al. 2010; Launhardt et al. 2012). Furthermore, we also show the colors of various VeLLOs: L673–7 (Dunham et al. 2008), IRAM04191 (Dunham et al. 2006), and CB130 (Launhardt et al. 2012). We find that the observed colors of our sample of candidate protostars appear consistent with the colors of more near-by Class 0 and VeLLO sources but not with FHSC candidate colors proposed in the literature (e.g., Commerçon et al. 2012). We find that the majority of these previously known Class 0 and VeLLO sources do not appear as red in their 70/24 colors as the reddest sources in our sample. The only exceptions to this trend are IRAS16293 and VLA1632–243, perhaps representing an extrema in the 70/24 color distribution that may be driven by their comparatively large envelope densities.

We also show in Figure 6 the colors of two FHSC candidates in Perseus: Per-Bolo 58 (Enoch et al. 2010) and B1-bS (Pezzuto et al. 2012). In this diagram, the 70/24 color of Per-Bolo 58 appears generally consistent with that of a VeLLO, as Enoch et al. (2010) point out. As such, this source may be an extremely low-mass protostar. On the other hand, the 70/24 color of B1-bS is comparable to the very reddest sources we find in Orion while the  $70\ \mu\text{m}$  flux is consistent with VeLLOs and fainter than the reddest sources in Orion by more than one order of magnitude. The faint but robust detection of a  $70\ \mu\text{m}$  point-source by Pezzuto et al. (2012) may indeed point to the possible Class 0 or VeLLO nature of B1-bS. We do however note that Pezzuto et al. also detect a source with no  $70\ \mu\text{m}$  counterpart, B1-bN, which may therefore represent a more robust FHSC candidate. Regardless of the elusive nature of FHSC candidates, when comparing our new candidate protostar colors to FHSC models by Commerçon et al. (2012), we find that our sources do not appear to be consistent with predicted or expected FHSC colors, with the caveat that distinguishing FHSCs from VeLLOs with continuum observations alone is likely difficult.

## 5. PACS BRIGHT RED SOURCES

Up to this point, we have discussed two distinct and well-defined samples of sources in Orion: i) the sample of candidate protostars identified with *Herschel* that have PACS  $70\ \mu\text{m}$  and  $160\ \mu\text{m}$  detections but MIPS  $24\ \mu\text{m}$  magnitudes greater than 7.0 mag, ii) the sample of protostars that were reliably identified with *Spitzer* ( $24\ \mu\text{m}$  magnitudes  $\leq 7.0$  mag Megeath et al. 2012; Kryukova et al. 2012). The protostar catalog target list used for the HOPS program consists mostly of the *Spitzer* identified protostars, but also contains some of the previously known protostars with  $m(24) > 7.0$  mag (Fischer et al., in preparation).

In what follows, we focus our analysis on the Orion protostars that have  $70/24 > 1.65$ . Of the 18 known protostars that satisfy this limit, 11 are identified with *Herschel*; hence this color regime is dominated by our newly identified protostars. Accordingly, *Herschel* has provided us for the first time with a far more complete sample of these red sources within the field of the HOPS survey. Given their red colors and their brightness in the PACS wavelength bands, we refer to this sample of protostars as PACS Bright Red sources, or PBRs. The coordinates, *Spitzer* photometry, and *Herschel* photometry of the sample are listed in Table 4, while the APEX  $350\ \mu\text{m}$  and  $870\ \mu\text{m}$  photometry are presented in Table 5. Since the APEX photometry are non-trivial to extract due in large part to contamination by cold surrounding material and, at  $870\ \mu\text{m}$  specifically, by the large beam size, we present three measures of the source flux, as described above.

### 5.1. Observed properties PBRs

As discussed above, we select 18 PBRs in Orion with observed 70/24 colors greater than 1.65. We show  $4.5\ \mu\text{m}$  to  $870\ \mu\text{m}$  images of 5 example PBRs in Figures 7 to 8 (see Appendix for the full sample images). Furthermore, in Figure 9 we show the full set of 18 PBRs observed SEDs from  $24\ \mu\text{m}$  to  $870\ \mu\text{m}$ . Inspection of the observed SEDs confirms that the PBRs sample is com-

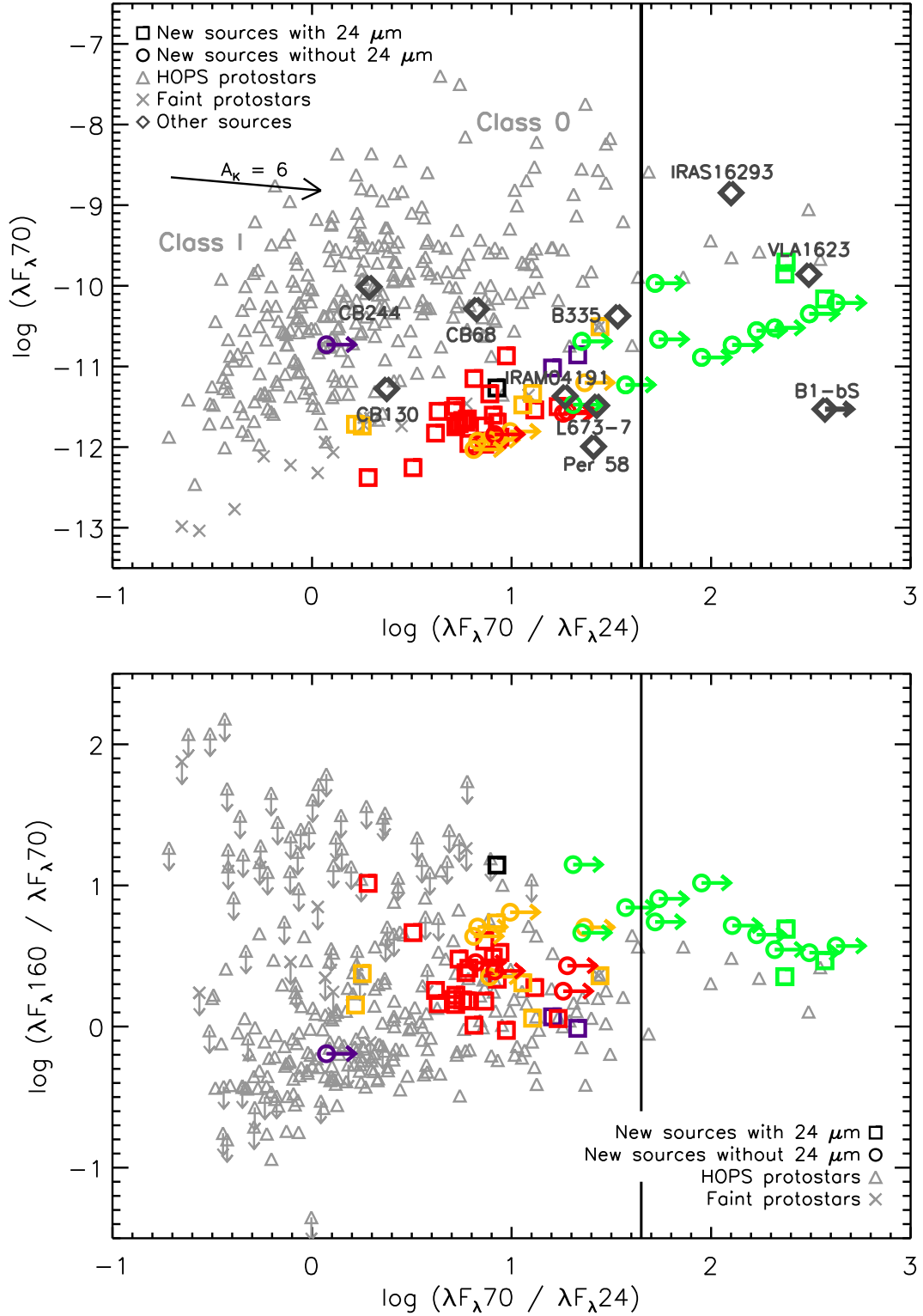


FIG. 6.— *Top*: 70  $\mu\text{m}$  flux vs. 70  $\mu\text{m}$  to 24  $\mu\text{m}$  flux ratio for HOPS-detected Orion protostars. Open squares and open circles indicate the new candidate protostars with and without MIPS 24  $\mu\text{m}$  detections, respectively. The color of the symbols indicates the flag values shown in Table 3 and discussed in § 3.2: here, green indicates sources that are reliable protostar candidates (flag = 1), orange indicates less reliable sources (flag = 2), red indicates extragalactic contamination (flag = 3), purple indicates other sources (flag = 4), and black indicates the single source without IRAC coverage. The solid vertical line indicates a 70  $\mu\text{m}$  to 24  $\mu\text{m}$  flux ratio of 1.65, our PBRs selection criterion (see § 5). Triangles and  $\times$  symbols indicate previously detected and characterized *Spitzer* protostars and faint protostellar candidates from Megeath et al. (2012), respectively. The arrow indicates the extinction vector for a value of  $A_K = 6$ . For comparison, we also indicate as large diamonds the scaled observed measurements for some well-known Class 0 sources, VeLLOs, and two FHSC candidates (see text). *Bottom*: 160  $\mu\text{m}$  to 70  $\mu\text{m}$  flux ratio vs. 70  $\mu\text{m}$  to 24  $\mu\text{m}$  flux ratio for HOPS-detected Orion protostars. The symbol and color type is the same as in the top panel. The reddest sources are distinguished from the bulk of *Spitzer*-identified HOPS sources (triangles) both by brighter 160  $\mu\text{m}$  fluxes and redder 70  $\mu\text{m}$  to 24  $\mu\text{m}$  flux ratios.

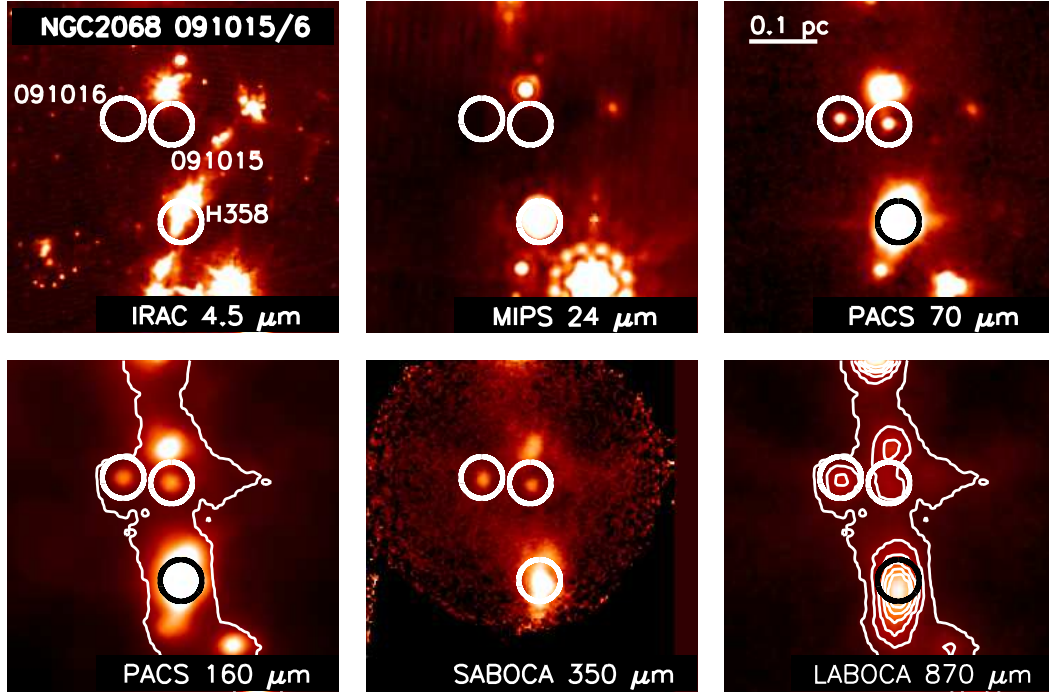


FIG. 7.—  $4' \times 4'$  images of three PBR sources, 091015 and 091016 (top), and HOPS358 (bottom), at the indicated wavelengths, shown on a log scale. North is up, east is to the left. The circles indicate the location of the PACS  $70 \mu\text{m}$  point-sources. Contours indicate the  $870 \mu\text{m}$  emission levels at  $\{0.25, 0.5, 0.75, 1.0, 1.25\} \text{ Jy beam}^{-1}$ . The lowest  $870 \mu\text{m}$  contour is over-plotted on the  $160 \mu\text{m}$  image. No IRAC emission coincident with 091015 or 091016 is detected; however, these sources clearly reside in dense filamentary material traced by the sub-mm emission. The HOPS358 photometry is likely blended.

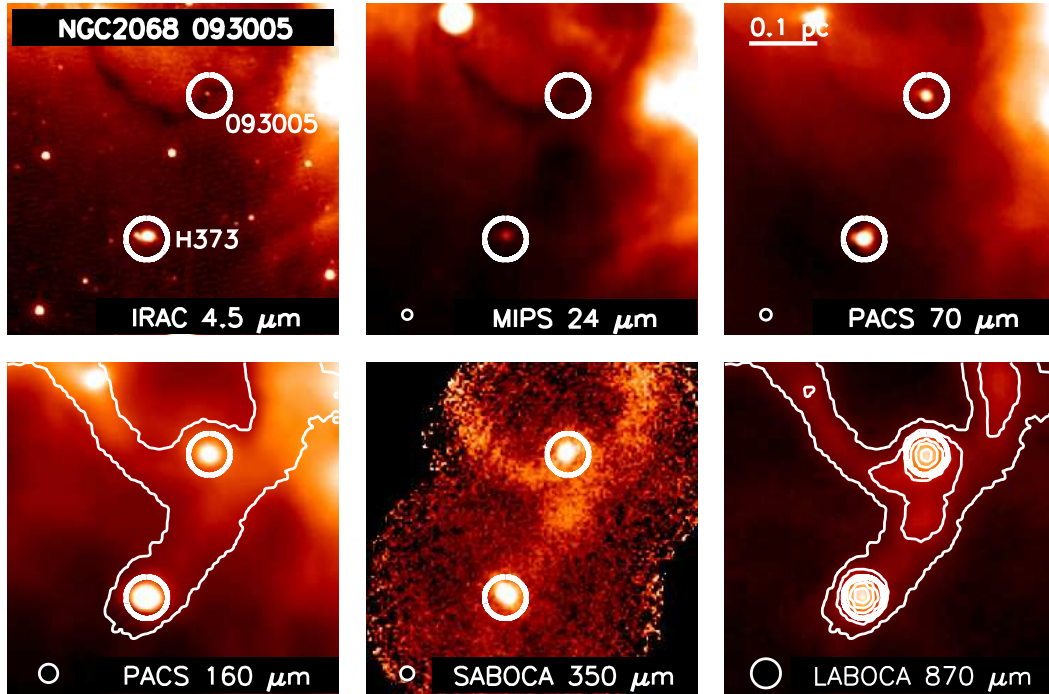


FIG. 8.— Same as Figure 7, showing  $4' \times 4'$  images two PBRs: 093005 (top) and HOPS373 (bottom). Contours indicate the  $870 \mu\text{m}$  emission levels at  $\{0.25, 0.5, 0.75, 1.0, 1.25, 1.5\} \text{ Jy beam}^{-1}$ . Source 093005 is the reddest PBRs shown in Figure 6 and lies at the intersection of three filaments traced by an 8 and  $24 \mu\text{m}$  absorption feature and the  $870 \mu\text{m}$  emission.

posed of cold, envelope dominated sources with peak emission always located at  $\lambda > 70 \mu\text{m}$ . In addition, the peak of the SEDs, and thus the temperatures, are well-constrained for all PBRs because we have obtained APEX sub-millimeter coverage for all sources.

In Table 6, we present some basic properties of the PBRs. In particular, we find that 12/18 sources exhibit *Spitzer*  $4.5 \mu\text{m}$  emission indicative of outflow activity. We also include some references to previous detections (see Appendix). Furthermore, 4/18 sources have significant levels of  $4.5 \mu\text{m}$  emission that are indeed consistent with a high inclination. The majority of sources, however, do not give clear indications of their inclinations at any observed wavelength, and therefore we cannot make any statements about their possible orientations based on their appearance in the images. We find indications from the  $4.5 \mu\text{m}$  image morphology that two sources (HOPS341 and HOPS354) are binaries, while seven sources have a nearby source within  $30''$ . Two reside in more crowded regions, and seven sources appear truly isolated. We find that a significant fraction (13/18) of sources appear to reside in filamentary regions, i.e., the extended  $870 \mu\text{m}$  emission appears significantly elongated.

The four sources with significant indications of a high inclination orientation are HOPS169, 302002, HOPS341, and HOPS354 (see Appendix for Figures 17, 21, 23, and 25). Inspection of their  $4.5 \mu\text{m}$  images reveals that their outflows appear well collimated and relatively narrow. Indeed, we might expect that sources that have denser envelopes, and are therefore presumably younger, may have more narrow cavity opening angles (e.g., Arce & Sargent 2006). As an additional check on our density analysis (see above), we use this inclination information for an independent check of the envelope densities of these four sources. Despite the relatively sparsely sampled SEDs, we fix the inclination to  $87^\circ$  and fit the source SEDs. We find that even when we fix the model inclination to  $\theta = 87^\circ$ , we still obtain envelope densities significantly above the  $\rho_1$  value found in the previous section.

### 5.2. Observational evolutionary diagnostics

We calculate  $L_{\text{bol}}$ ,  $T_{\text{bol}}$  (Myers & Ladd 1993), and  $L_{\text{submm}}/L_{\text{bol}}$  (André et al. 1993, 2000). The errors in  $L_{\text{bol}}$  and  $T_{\text{bol}}$  are derived with the same Monte Carlo method as described in § 6.2 for the modified black-body parameters. We exclude the IRAC upper limits from this analysis; including these limits has an effect on our  $L_{\text{bol}}$  and  $T_{\text{bol}}$  estimates that is smaller than our estimated errors. We do, however, include the  $24 \mu\text{m}$  upper limits; therefore the  $L_{\text{bol}}$  and  $T_{\text{bol}}$  values should be considered upper limits for sources not detected at this wavelength. Furthermore, we investigate the effect of applying an average foreground reddening correction to all the new *Herschel* candidate protostars. We find that dereddening the observed fluxes with extinction levels of  $A_V = 40$  magnitudes has no effect on the derived parameters because the observed SEDs are extremely red and cold.

### 5.3. Spatial distribution of the three samples

We show the locations of the *Herschel* protostar candidates compared to the locations of the HOPS sample in

Figure 10; these positions are overlaid on the extinction map of Orion. It is immediately apparent that the spatial distribution of the new candidate protostars and PBRs is non-uniform. To investigate this distribution further, we show the relative fraction of new sources as a function of individual region in Table 7. The over-all number of new candidate protostars and PBRs is dominated by the Orion A cloud, and in particular L1641. This is not surprising since the L1641 region is quite large and contains more protostars compared to other Orion regions. The fractions of new candidate protostars and PBRs compared to the total number of HOPS and new candidate protostars is, however, 2 times larger in Orion B. This result is even more pronounced when we consider only the fractions of PBRs, with fractions that are more than 10 times larger in Orion B. The NGC2068 (also containing the NGC2071 nebula) and NGC2024 (also containing the Horsehead or NGC2023 nebula) fields in Orion B have not only the largest fraction of new candidate protostars, but also of PBRs. While these numbers and fractions are subject to counting statistics and other possibly large sources of errors, the differences between Orion A and Orion B appear to be significant.

About 5% of the combined protostars and candidate protostars in Orion are PBRs. If we consider the PBRs as representing a distinct phase in the evolution of a protostar, and we assume a constant rate of star formation, the fraction the variation suggests that the protostars spend 5% of their lifetime in the PBRs phase (approximately 25,000 years with the 0.5 Myr protostellar lifetime of Evans et al. 2009), averaging over all Orion regions. However, the assumed duration of the PBRs phase would vary greatly with location, from 5,000 years in the Orion A cloud to 80,000 years in the Orion B cloud. There are two alternative explanations. First, there might be environmental reasons which would favor the formations of PBRs, or perhaps extend the duration of the PBRs phase, in the Orion B cloud. Second, the ages of all the protostars in the Orion B cloud may be systematically younger than those in the Orion A cloud. In this case, the regions containing the PBRs in the Orion B could be undergoing very recent bursts of star formation.

Studies of pre-main sequence stars in the Orion molecular clouds show little evidence for significant age differences between the Orion A and B clouds. Flaherty & Muzerolle (2008) determined an age of  $\sim 2$  Myr for NGC2068 and NGC2071, while Reggiani et al. (2011), Hsu et al. (2012) and Da Rio et al. (2012) determine ages for the ONC and L1641 of  $\sim 2 - 3$  Myr. However, most of the protostars associated the NGC2068 and NGC2071 regions are outside the clusters of pre-main sequence stars and in dense filaments gas neighboring these clusters (Motte et al. 2001). A number of PBRs are in the LBS 23 clump (directly south of NGC2068) and in the NGC2023 clump (in the NGC2024 field); these are two of the 5 most massive, dense clumps found in Orion (Lada et al. 1991a). Compared to the other massive clumps, both of these regions have 1/10 the numbers of young stars per unit gas mass and hence may be quite young (Lada et al. 1991b; Lada 1992). Alternatively, the gas in the LBS 23 and NGC2023 clumps may have dense gas filling factors that are much higher than the other massive clumps (Lada et al. 1997); hence, they sources in these regions may be forming in a very

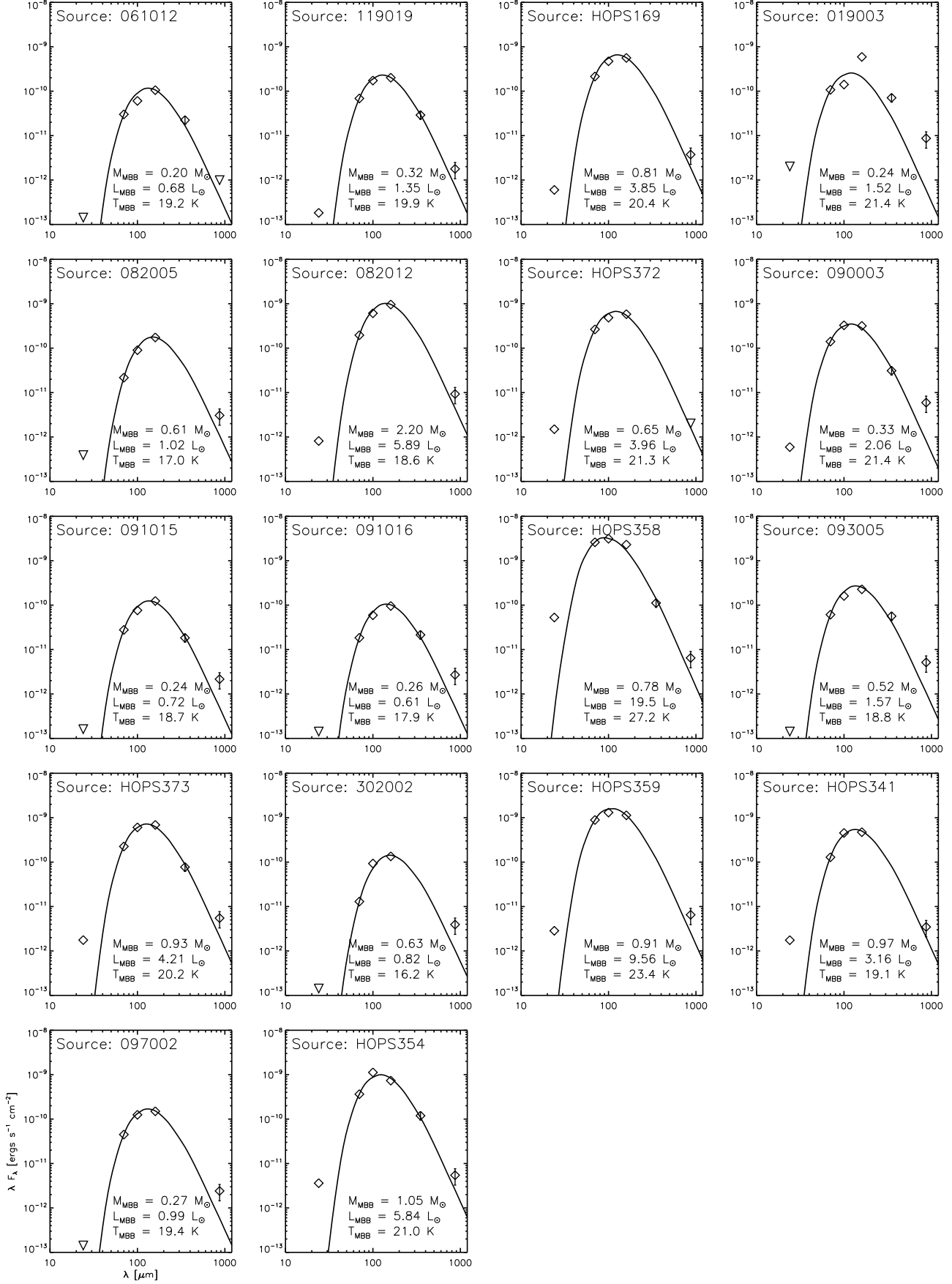


FIG. 9.— SEDs of the 18 PBRs are shown. The errors are smaller than the symbol size except for the 350 and 870  $\mu\text{m}$  data points. The black curve shows the modified black-body fit to the observed SED, with the indicated best fit parameters (see § 6.2). Note that PBRs 19003 (shown in the top right) is located in a complex field where the photometry may be strongly contaminated.

different birth environment. The regions bordering the southern rim of the NGC2068 nebula and the northern rim of the NGC2071 nebula are also rich in protostars (see Megeath et al. 2012). Thus, the PBRs are found concentrated in sub-regions which may indeed be quite young. We will investigate these possibilities in future work.

## 6. DETERMINING THE PHYSICAL PROPERTIES OF PBRs THROUGH MODELS

In this section we describe our analysis of the physical properties of the PBRs as inferred from their colors and SEDs. We first compare the 70/24 colors of the PBRs sample with those derived from a grid of models which adopt the solution for a rotating envelope undergoing collapse (Ulrich 1976; Terebey et al. 1984) with outflow cavities along the rotation axis of the envelope (Whitney et al. 2003a). This analysis puts a constraint on the minimum inner density of the protostellar envelope. Next, we compare the observed SEDs to model SEDs generated using the Hyperion (Robitaille 2011) radiative transfer code. This set of models assumes radial power-law gradients consistent with either a collapsing core with a constant infall rate and a static isothermal core. The models also encompass various combinations of internal and external heating. Given the prohibitively large computational time needed to explore the full range of parameters space using radiative transfer models, and given our inability to distinguish between models purely from five to six photometry points, we do not provide individual model fits to each protostars. Instead we fit a single temperature modified black-body function to the observed SEDs at 70  $\mu\text{m}$  and longer wavelengths. The modified black-body fits provide luminosities and an initial characterization of the envelope masses of the PBRs sample.

### 6.1. Axisymmetric models: interpreting the 70/24 color

We begin our analysis by using a simplified version of the Ali et al. (2010) protostellar envelope model grid to predict observed fluxes and colors for comparison with our PBRs. The density distribution of these models is that of the collapse of a spherical cloud in uniform rotation (Ulrich 1976), which is the inner region of the Terebey et al. (1984) model of the collapse of the slowly-rotating isothermal sphere. This model is then modified by the inclusion of outflow cavities of various shapes (Whitney et al. 2003a,b). This schematic model envelope captures the dependence of the short wavelength (24  $\mu\text{m}$  and 70  $\mu\text{m}$ ) fluxes on inclination due to rotation and bipolar cavities.

The model fluxes depend upon the mass infall rate, the angular momentum of the mass currently falling in, the outflow cavity properties, the inclination of the rotation axis to the line of sight, and the luminosity of the central source, as well as the assumed dust properties. The thermal emission of the dusty envelope does not depend directly on the mass infall rate but instead on the density of the envelope. The model assumes free-fall at a constant rate, which results in a density profile with shape  $\rho \propto r^{-3/2}$  (Terebey et al. 1984). The overall scaling of the density is characterized by  $\rho_1$ , the density at 1 AU

in the limit of no rotation:

$$\rho_1 = 7.4 \times 10^{-15} \left( \frac{\dot{M}_{\text{env}}}{10^{-6} M_{\odot} \text{ yr}^{-1}} \right) \left( \frac{M_*}{0.5 M_{\odot}} \right)^{-1/2} \text{ g cm}^{-3}, \quad (1)$$

The envelope mass infall  $\dot{M}_{\text{env}}$  rate is related to  $\rho_1$  via the free-fall velocity, which in turn depends upon the unknown central mass  $M_*$ . The actual model density structure departs from  $r^{-3/2}$  on small scales because of the angular momentum of the infalling material. This enters into the model through the parameter  $R_{\text{disk}}$ , the outer disk radius at which infalling material currently lands (see Ulrich 1976).

The rotation leads to a significant dependence of the SED on the inclination of the rotation axis relative to the line of sight (Kenyon et al. 1993). This dependence is significantly enhanced by the inclusion of outflow cavities (Whitney et al. 2003a) which are assumed to be aligned along the rotation axis. Finally, the overall shape of the SED is only weakly affected by the luminosity of the central source ( $L_*$ ; Kenyon et al. 1993) and so this is easily scaled.

To roughly compare observed PBRs colors with those predicted by our model grid in Figure 11 we show the effects of varying the model inclination, envelope density, and cavity opening angle on the 70/24 color and 70  $\mu\text{m}$  flux. As stated above, these model tracks are based on a simplified version of the Ali et al. (2010) model grid; we refer the reader to that publication for details. In brief, the model tracks that we consider here have the same fixed parameters as those listed in Table 1 of Ali et al. (2010), including a fixed central mass of  $0.5 M_{\odot}$ ; in addition we have fixed the cavity shape exponent to a value of  $b = 1.5$ , and the envelope outer radius to  $R_{\text{env,max}} = 1 \times 10^4 \text{ AU}$ . We have, however, expanded the envelope infall rate grid relative to the Ali et al. (2010) grid to larger values (up to  $\dot{M}_{\text{env}} = 10^{-3} M_{\odot} \text{ yr}^{-1}$  on a pseudo-logarithmic grid) and included a model with no envelope. As described above, for our model grid we assume that the envelope density falls off as  $\rho(r) \propto r^{-3/2}$ . In addition, while our model grid is parametrized in terms of  $\dot{M}_{\text{env}}$ , with a fixed central mass of  $M_* = 0.5 M_{\odot}$ , we will refer to  $\rho_1$  throughout this section.

We note that the assumed central masses of protostellar sources remain largely unconstrained observationally (however see Tobin et al. 2012), but may be lower than our assumed value. The effect of a lower central mass would be to lower  $\dot{M}_{\text{env}}$  for a given value of  $\rho_1$ . For example, if the central mass is  $0.2 M_{\odot}$ , the infall rates reported for our models would be reduced by a factor of 0.6. The assumed central mass, however, does not change the value of  $\rho_1$  corresponding to a given model SED. Furthermore, our small assumed disk radius does not strongly affect the trends shown here.

With this model grid we isolate the effects, albeit in a simplified fashion, of varying the model inclination (viewing angle to the protostar), envelope density ( $\rho_1$ ), and cavity opening angle ( $\theta_C$ ) on the 70  $\mu\text{m}$  fluxes and 70/24 colors. In Figure 11, we show model tracks through 70  $\mu\text{m}$  flux vs. 70/24 color space for high inclination ( $87^\circ$ ) viewing angles as a function of both  $\theta_C$  and envelope density ( $\rho_1$ ). By analyzing only the high inclination models

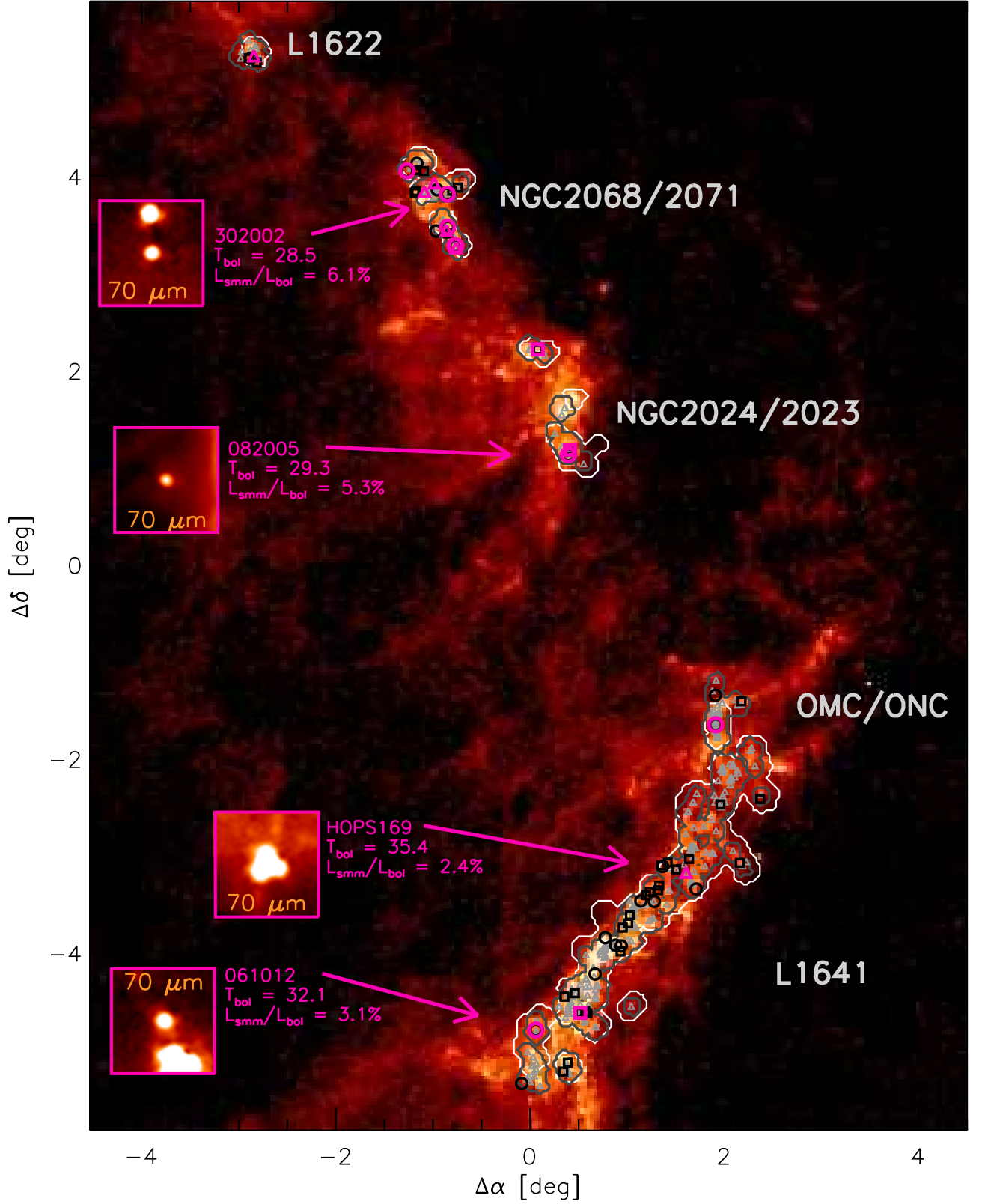


FIG. 10.— The distribution of red protostars overlaid on the extinction map of Orion. The dark grey contour shows the HOPS PACS coverage and the white contour shows the LABOCA  $870\ \mu\text{m}$  coverage. The triangles (light grey) indicate the positions of the HOPS protostars while the black points (squares and circles) indicate the positions of the new candidate protostars. The PBRs are highlighted in fuchsia and the properties of four selected PBRs are shown along with their corresponding  $1' \times 1'$  HOPS  $70\ \mu\text{m}$  images.

we obtain a lower limit on the envelope density required to reproduce the red 70/24 colors.

We assume a fixed disk accretion rate of  $\dot{M}_{\text{disk}} = 1.0 \times 10^{-8} M_{\odot} \text{ yr}^{-1}$ , a disk outer radius of  $R_{\text{disk,max}} = 5 \text{ AU}$ , and a central source luminosity of  $1 L_{\odot}$ . Increasing  $\dot{M}_{\text{disk}}$  and  $R_{\text{disk,max}}$  drives the models to both bluer 70/24 colors and brighter  $70 \mu\text{m}$  fluxes, while decreasing the inclination drives the models to bluer 70/24 colors. Therefore, we find that no model in our grid can explain 70/24 colors with envelope densities less than  $\log \rho_1 / (\text{g cm}^{-3}) \sim -13.4$  (or equivalently an envelope infall rate of  $\dot{M}_{\text{env}} = 5.4 \times 10^{-6} M_{\odot} \text{ yr}^{-1}$ ). While models with larger values of  $\rho_1$  and other combinations of parameters can be found for bluer 70/24 colors, this analysis sets an approximate lower limit on the expected envelope densities of sources with  $70/24 > 1.65$  of  $\log \rho_1 / (\text{g cm}^{-3}) \gtrsim -13.4$ . That is, high source inclinations alone cannot explain the red 70/24 colors of the PBRs, which also require dense envelopes.

We expect that this value of  $\rho_1$  should lie well within the Class 0 range; e.g., Furlan et al. (2008) found for a sample of 22 Class I sources in Taurus  $\log \rho_1 / (\text{g cm}^{-3}) \leq -13.2$ , while over half had  $\rho_1$  values that are lower than  $\log \rho_1 / (\text{g cm}^{-3}) = -13.4$ . Note that the Furlan et al. (2008) data-set included far better sampling of the source SEDs and, most critically, *Spitzer* IRS spectroscopy, allowing for a more robust estimate of the parameters of sources in their sample. In contrast, our SEDs generally are envelope dominated with few sources having robust detections shortward of  $24 \mu\text{m}$ . Therefore, any estimate of the value of the envelope density will be necessarily imprecise and have a back of the envelope character. That said, our comparison with the model grid and previous derived values of the envelope density leads us to conclude that the  $70/24 > 1.65$  color cut, while not uniformly selecting a unique envelope density threshold, will preferentially select Class 0 sources with  $\log \rho_1 / (\text{g cm}^{-3}) \gtrsim -13.4$ , irrespective of source inclination.

Having demonstrated that the very red 70/24 colors require large values of  $\rho_1$ , as expected for SEDs peaking at long wavelengths, we proceed by analyzing the PBRs in the context of more simplified models. In what follows, we carry out two independent analyses of the source SEDs: a qualitative model image comparison using 1D models generated with the Hyperion (Robitaille 2011) radiative transfer code, and modified black-body fitting to the observed SEDs at  $70 \mu\text{m}$  and longer wavelengths. We attempt to maintain consistency by using similar envelope dust models throughout the analysis presented here. For the Hyperion model image analysis we use the Ormel et al. (2011) opacities. These opacities are similar to the commonly assumed Ossenkopf & Henning (1994) (“OH5”; see below) opacities but include both the scattering and absorption components at short wavelengths, needed for radiative transfer calculations. Specifically, we use the “icsgra2” Ormel et al. (2011) model opacities, which include icy silicates and bare graphites, with a coagulation time of 0.1 Myr. We assume the dust model from Ossenkopf & Henning (1994) for the long-wavelength modified black-body fits, specifically, their “OH5” opacities, corresponding to column 5 of their Table 1. These opacities reflect grains having thin ice man-

gles with  $10^5$  years of coagulation time at an assumed gas density of  $10^6 \text{ cm}^{-3}$ .

## 6.2. Spherically symmetric models: Comparison to photometry derived from model images

We use the Hyperion (Robitaille 2011) Monte Carlo radiative transfer code to investigate some basic properties of the PBRs. We run a series of spherically symmetric models under a range of very simple assumptions, and produce simulated images. As stated above, the dust model we assume is that of Ormel et al. (2011) (“icsgra2”). To explore which model assumptions might be reasonable for analyzing the properties of the reddest sources in Orion, we investigate a few limiting model scenarios. We therefore disregard the details of the individual source SEDs of the entire red sample and qualitatively compare the SEDs of the two sources with the smallest and largest values of  $L_{\text{bol}}$  and  $T_{\text{bol}}$  (sources 091016 and HOPS358, respectively; see Table 8) with photometry derived from model images.

We generate a series of model images that fall into four classes: i) a starless core at a constant temperature of 10 K (referred to here as the “core” model); ii) a starless core with an isotropic external radiation field (“core+external”); iii) a core with an internal source (“star” model); and finally, iv), a core with both an internal source and an isotropic external radiation field (“star+external”). For each of these classes of models, we test a range of density profile shapes and density normalizations. For the density profile shape we assume two values,  $\alpha = 1.5, 2.0$ , where  $\alpha$  is the radial density profile power law index:  $\rho(r) \propto r^{-\alpha}$ . For the absolute value of the (gas) density normalization at 1 AU we assume 5 values:  $\log(\rho_{1\text{AU}} / (\text{g cm}^{-3})) = -10$  to  $-14$ , in steps of  $\delta \log(\rho_{1\text{AU}} / (\text{g cm}^{-3})) = 1.0$ . For models with external heating, the bolometric strength of the interstellar radiation field (ISRF) is set to the value from Mathis et al. (1983) at the solar neighborhood ( $4\pi J_{\nu} = 0.0217 \text{ ergs/cm}^2/\text{s}$ ). The spectrum of the radiation field is assumed to be that at the solar neighborhood from Porter & Strong (2005), but reddened by  $A_V = 10$  using the Kim et al. (1994) extinction law. The ISRF model includes contributions from the stellar, PAH, and FIR thermal emission. The inner radius of the core is set to the radius at which the dust sublimates, assuming a sublimation temperature of 1,600 K, while the outer radius is set to 1 pc. The central source is taken to have  $10 L_{\odot}$  and a spectrum given by a Planck function at the effective temperature of the Sun (5778 K). The choice of the stellar temperature is arbitrary, and is unimportant for the modeling presented here, since all sources are deeply embedded and all stellar radiation is reprocessed — only the total bolometric luminosity is important (see e.g., Johnston et al. 2012, for a discussion of the  $R_{\text{star}}$  and  $T_{\text{star}}$  degeneracy).

The high levels of spatial filtering caused by our adopted aperture photometry scheme require us to assume such a central source luminosity to roughly match the flux levels in the observed SEDs. Furthermore, while a 1 pc sized envelope is larger than usually assumed, the high levels of spatial filtering inherent in the aperture photometry cause us to be insensitive to structure on scales larger than the assumed aperture sizes.

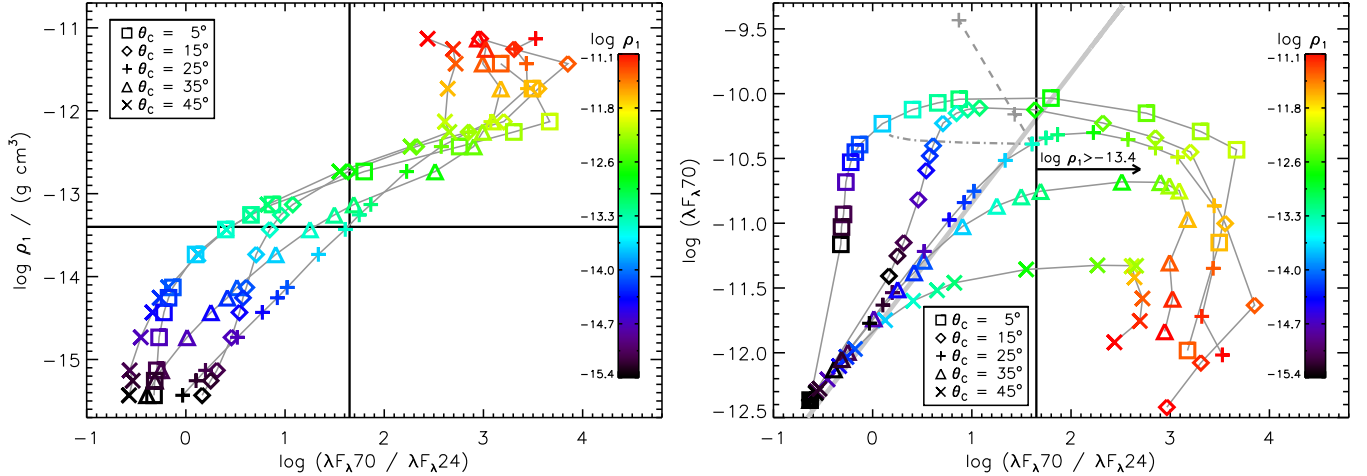


FIG. 11.— Left: Dependence of the model 70  $\mu\text{m}$  to 24  $\mu\text{m}$  flux ratio for *high inclination* orientations ( $87^\circ$ ) on envelope density ( $\rho_1$ ) for the 5 cavity opening angles in our grid. These model tracks assume an internal luminosity of  $1.05 L_\odot$ . The 70/24 color selection is indicated with the vertical black line, while the corresponding  $\log \rho_1 / (g \text{ cm}^{-3}) \sim -13.4$  (corresponding to an envelope infall rate of  $\dot{M}_{\text{env}} = 7.5 \times 10^{-6}$ ) threshold is indicated with a horizontal black line. Right: Model 70  $\mu\text{m}$  flux vs. 70  $\mu\text{m}$  to 24  $\mu\text{m}$  flux ratio for *high inclination* orientations ( $87^\circ$ ). For the model with a cavity opening angle of  $\theta_c = 25^\circ$  (+-symbols) and  $\log \rho_1 / (g \text{ cm}^{-3}) \sim -13.4$ , we show the effect of increasing the internal luminosity by two orders of magnitude with the dashed grey curve while the effect of decreasing the inclination to  $18^\circ$  is illustrated with the dot-dashed curve. All models with higher assumed values of  $\dot{M}_{\text{disk}}$  and lower inclination will have envelopes that are denser than  $\log \rho_1 / (g \text{ cm}^{-3}) \sim 13.3$ , the median value of  $\rho_1$  in our model grid; sources with redder 70 to 24  $\mu\text{m}$  colors cannot be explained by envelopes that are less dense than this threshold. The light grey thick line corresponds to a 24  $\mu\text{m}$  limit of 7 magnitudes, the imposed *Spitzer* protostar magnitude limit for identification of protostars.

The model images have a resolution of  $1'' \text{pix}^{-1}$ , or 420 AU at our assumed distance. We convolve these images with the azimuthally averaged PSFs provided by Aniano et al. (2011), except in the case of the SABOCA 350  $\mu\text{m}$  and LABOCA 870  $\mu\text{m}$  images. These wavelengths are convolved with Gaussian PSFs with FWHMs equal to  $7.4''$  and  $19''$  respectively, i.e., the nominal beam sizes for our observations. All model image photometry is then performed on the convolved model images using the same aperture and sky annulus parameters as those applied to the data. The use of such photometric aperture parameters can cause large amounts of spatial filtering due the small sizes of the apertures relative to the beam sizes and the extent of the core emission (see below).

We show our extracted model SEDs in Figure 12 and a subset of the corresponding model images in Figure 13. In general, we find that models without internal sources are very unlikely to match the observed PBRs properties, on the basis that their SEDs are less luminous and peak at longer wavelengths than the observed SEDs for all density profile shapes that we assume; see Figure 12, top panels. While the “core+external” models (top right panel) suffer from severe spatial filtering, it is unlikely that such models will well represent the data as these SEDs tend to also peak at longer wavelengths. For the two classes of models with internal sources we find better agreement with the data; see lower panels of Figure 12. While steeper envelope profiles may imply somewhat higher envelope densities, the range in plausible densities for  $\alpha = 1.5$  is  $\log \rho_1 \sim -12$  to  $-13$ , while for  $\alpha = 2.0$  values of  $\log \rho_1 \sim -12$  roughly agree with the shapes the observed SEDs. We note that we find very little difference between the “star+external” and the “star” model in the  $\lambda \lesssim 160 \mu\text{m}$  regime, possibly indicating that our assumed ISRF strength relative to the assumed internal source luminosity may be underestimated compared

to what we might expect to find regions like Orion.

### 6.3. Modified black-body fits to the PBRs

An individual detailed fit to each protostar is beyond the scope of this work considering the vast amount of parameter space needed to model protostellar SEDs (i.e., source luminosity, envelope density, envelope rotation, outflow cavity geometry, external heating, outer envelope structure). Furthermore, unlike most of the HOPS protostars, whose properties can be constrained from a combination of far-IR photometry, 5  $\mu\text{m}$  to 40  $\mu\text{m}$  *Spitzer*/IRS spectra, and Hubble near-IR imaging (Fischer et al. 2010, 2012), the properties of the SEDs must currently be derived from 5 to 6 photometry points at long wavelength. While the above modeling and analysis shows that the internal source is important, the longer wavelength fluxes are probing the bulk of the envelope mass, expected to mostly be at a single temperature. Furthermore, for density profiles in the range of  $\rho(r) \propto r^{-3/2}$  or  $r^{-2}$ , as assumed above, we expect that most of the envelope will be located at large radii. We therefore perform modified black-body fits to the  $\lambda \geq 70 \mu\text{m}$  SEDs listed in Tables 4 and 5. For this analysis we use the beam flux measurements for the sub-millimeter 350  $\mu\text{m}$  and 870  $\mu\text{m}$  portion of the SED. The results of the analysis are presented in Table 8 and the model SEDs are plotted with the data in Figure 9.

Before fitting the long-wavelength SEDs of the sources, we apply color corrections to the *Herschel* 70  $\mu\text{m}$ , 100  $\mu\text{m}$ , and 160  $\mu\text{m}$  fluxes. Following (Launhardt et al. 2012), these photometric color corrections have been derived iteratively from the slopes of the PACS SEDs, using polynomial fits to the values in Table 2 of the PACS calibration release note “PACS Photometer Passbands and Colour Correction Factors for Various Source SEDs” from April 12, 2011. The color corrections for the APEX

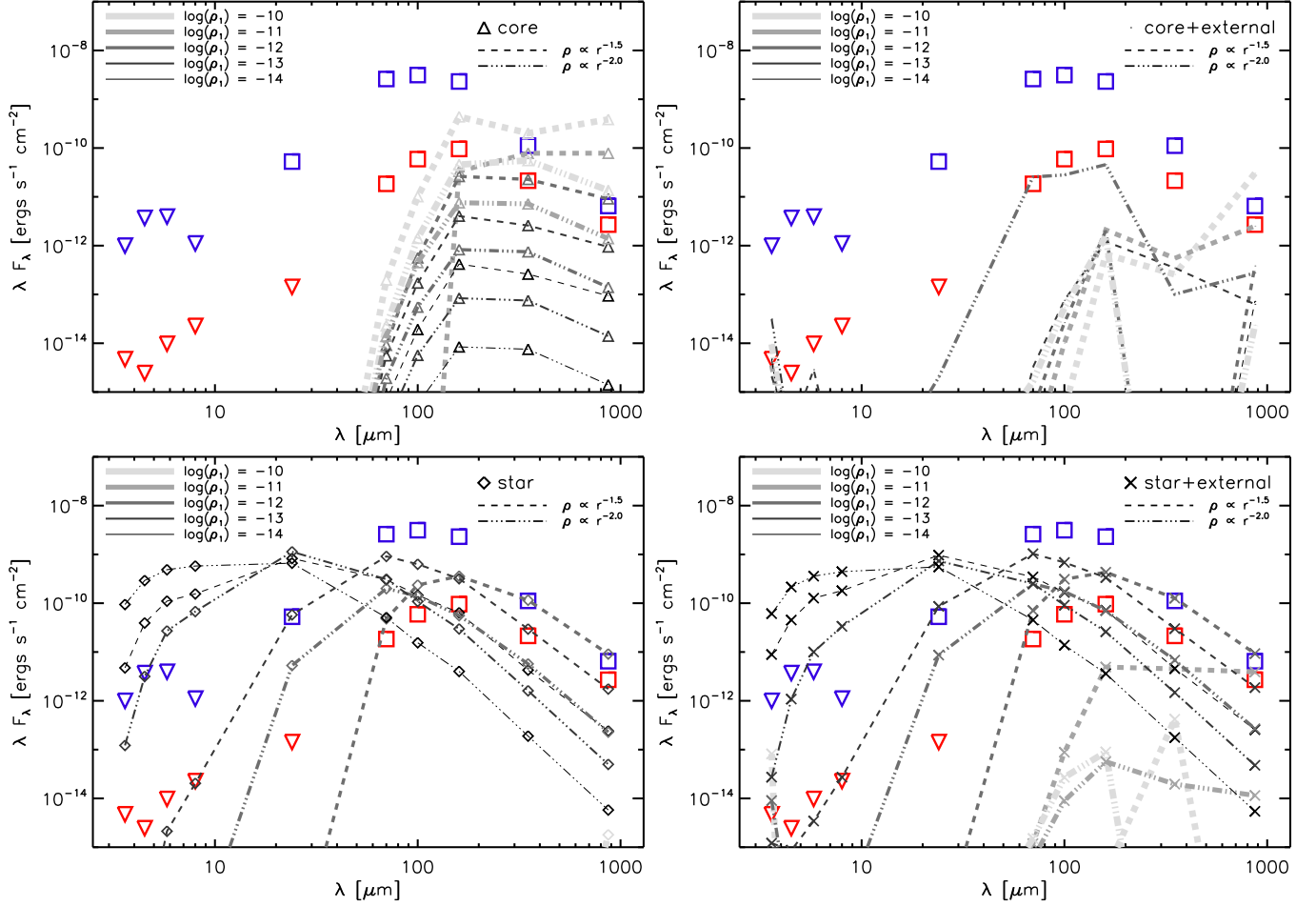


FIG. 12.— All panels show the SEDs of HOPS358 (blue;  $L_{\text{bol}} = 30.6 L_{\odot}$  and  $T_{\text{bol}} = 44.2$  K) and 091016 (red;  $L_{\text{bol}} = 0.65$  and  $T_{\text{bol}} = 29$  K), the extrema of the  $L_{\text{bol}}$  and  $T_{\text{bol}}$  distributions for the reddest sources, compared to spherical models. The two line styles indicate the different assumptions for the density profile shape while the shade of grey indicates the different model density  $\rho_1$  values. The four panels correspond to the four different models that we test (see text): *Top left*: the “core” model, a starless core; *Top right*: the “core+external” model, a starless core with external heating; *Bottom left*: the “star” model, a core with an internal source; and finally, *Bottom right*: the “star+external” model, consisting of a core with an internal source which is irradiated by an external radiation field. Severe spatial filtering due to our aperture photometry on the model images can be seen most notably in the two externally heated models (left column).

data are assumed to be negligible.

The form of the modified black-body function is given by

$$S_{\nu} = \Omega B_{\nu}(\nu, T_d) (1 - e^{-\tau(\nu)}), \quad (2)$$

where  $\Omega$  is the solid angle of the emitting element,  $B_{\nu}(T_d)$  is the Planck function at a dust temperature  $T_d$ , and  $\tau(\nu)$  is the optical depth at frequency  $\nu$ . Here, the optical depth is given by  $\tau(\nu) = N_H m_H R_{gd}^{-1} \kappa(\nu)$ , where  $N_H = 2 \times N(\text{H}_2) + N(\text{H})$  is the total hydrogen column density,  $m_H$  is the proton mass,  $\kappa_{\nu}$  is the assumed dust opacity law from Ossenkopf & Henning (1994), and  $R_{gd}$  is the gas-to-dust ratio, assumed to be 110 (Sodroski et al. 1997). The best-fit total masses  $M_{\text{tot}}$  reported in Table 8 have been multiplied by an additional factor of 1.36 to account for helium and metals. Furthermore, in Table 8 we also report the peak wavelength of the best-fit modified black-body model. Finally, we estimate  $L_{\text{smm}}$  from the model SED, where  $L_{\text{smm}}$  is integrated over  $\lambda \geq 350 \mu\text{m}$ .

If a given source SED has coverage over fewer than 4 long-wavelength points, we do not fit a model to the SED. While all the PBRs sources satisfy this criterion,

all the new candidate protostars and HOPS sources do not (see § 5.2) and are therefore not fitted. The errors on  $T_d$ ,  $M_{\text{tot}}$ , and the thermal component of the luminosity ( $L_{\text{MBB}}$ ) are estimated through a straight-forward Monte Carlo method<sup>12</sup>. For each source we generate 2000 synthetic SEDs drawn from a normal density with mean and standard deviation equal to those of the measured SED at each wavelength. We then fit each synthetic SED. The reported error is equal to the standard deviation of the resulting distribution of each parameter. These errors do not include systematics introduced by, e.g., our dust model assumption or variation in the gas-to-dust ratio.

We show the modified black-body fit results, along with the SEDs of the PBRs, in Figure 9. The resulting best-fit mass, luminosity, and temperature is also indicated for each source. The model fits the data surprising well considering that significant temperature gradients in the envelope are expected. Furthermore, in all cases the

<sup>12</sup> “Offered the choice between mastery of a five-foot shelf of analytical statistics books and middling ability at performing statistical Monte Carlo simulations, we would surely choose to have the latter skill.” Press, 1993, Numerical Recipes, page 686.

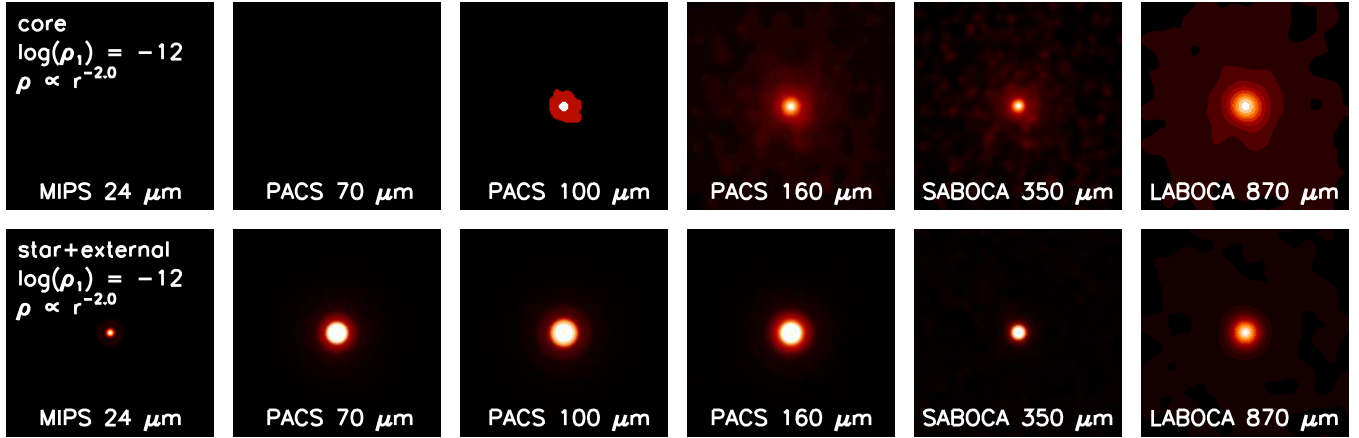


FIG. 13.— Convolved model images at the indicated wavelengths, shown on a log scale with the same minimum and maximum flux levels for all panels to illustrate the shape of the model SEDs. Each image is  $200''$  (or 84000 AU) on a side. The top row shows the “core” model images, with  $\log(\rho_1) = -12$  and a density profile shape of  $\rho \propto r^{-2.0}$ , corresponding to the top left panel in Figure 12. The bottom row shows the “star+external” model, with the same density parameters as the top row, corresponding to the bottom right panel in Figure 12.

$24 \mu\text{m}$  point, when detected, has a much higher flux level than the modified black-body model. We interpret this discrepancy as strong evidence for internal heating by a protostar.

Excluding the  $70 \mu\text{m}$  point and fitting only the  $\lambda \geq 100 \mu\text{m}$  SED has a minor effect on the resulting parameter values. Without  $70 \mu\text{m}$ , the masses systematically increase by 40%, the temperatures decrease by 5%, and the luminosities decrease by 7%. This small effect may be understood by the fact that the  $100 \mu\text{m}$  fluxes are well-correlated with the  $70 \mu\text{m}$  fluxes for this sample, tracing similar material near the protostars. The temperatures at  $100 \mu\text{m}$  and  $70 \mu\text{m}$  are not dramatically different, and most likely both points are dominated by optical-depth effects such that the  $\tau = 2/3$  surface is not significantly different between the two wavelengths. From Hartmann (2009), the radius of the  $\tau = 2/3$  surface can be roughly approximated as  $r_\lambda \propto \kappa_\lambda^{-2}$ ; this relation implies that  $r_{70}/r_{100} \sim 2.5$ .

Our best-fit modified black-body model always underestimates the observed  $870 \mu\text{m}$  flux of all sources. The model sub-millimeter SEDs are always bluer than the observed SEDs. We find that the discrepancy is at the  $0.83 \pm 0.26 \text{ Jy}$  level (or a factor of  $\sim 3$ ) excess, where the error bar represents the standard deviation in the residual distribution. It is likely that this discrepancy is dominated by the larger beam size of the  $870 \mu\text{m}$  observations which has the effect of mixing the source flux with that of the surrounding cold and possibly high-column environment. Contamination to the  $870 \mu\text{m}$  flux by disk emission may also increase this discrepancy. Jørgensen et al. (2009) find average disk masses of  $\sim 0.13 M_\odot$  (with a large scatter) across their sample of Class 0 sources. The sources in their sample that are comparable to our PBRs, however, are those with the lowest values of  $T_{\text{bol}}$ . For reference, they found that IRAS4A1, with a  $T_{\text{bol}} = 43 \text{ K}$ , has the largest disk mass of  $0.46 M_\odot$  in their sample; on the other hand, L1157, with a similar  $T_{\text{bol}} = 42 \text{ K}$ , has a disk mass about a factor of 4 smaller. We estimate that a  $30 \text{ K}$  disk of  $0.5 M_\odot$  would contribute  $\sim 0.6 \text{ Jy}$  to the beam flux at  $870 \mu\text{m}$  (assuming Ossenkopf & Henning

(1994) dust opacities, as above). Therefore, disk emission could indeed contribute to the observed  $870 \mu\text{m}$  flux but further detailed observations at high resolution are needed to disentangle the envelope component from the possible disk emission. Another possible source of ambiguity in interpreting the  $870 \mu\text{m}$  flux discrepancy is the model dust opacity assumption. Furthermore, we do not find an  $870 \mu\text{m}$  discrepancy in the analysis of model images presented in the previous section. This indicates that large disk masses may not be necessary to explain the sub-millimeter fluxes. We therefore emphasize that the disk masses inferred here from the  $870 \mu\text{m}$  excess should be regarded only as upper limits; further detailed investigation into the disk properties of our sources is deferred to future work.

Independent of these issues, it is clear that a more accurate treatment of the data would require all images to be convolved to a matched resolution; however, this approach would have the effect of causing non-detections for a majority of sources at the shorter wavelengths due to the relatively large limiting beam size of our data-set ( $\sim 19''$  at  $870 \mu\text{m}$ ). Homogeneously extracted SEDs are therefore not feasible for this data-set as a whole. Nevertheless, we test the effects of convolving the data before extracting the SEDs. We choose PBRs 119019 as a test source because it is isolated and has approximately median values for the best-fit modified black-body temperature, luminosity, and mass. Ignoring the  $870 \mu\text{m}$  data, this source is clearly detected at  $70 \mu\text{m}$ ,  $100 \mu\text{m}$ ,  $160 \mu\text{m}$ , and  $350 \mu\text{m}$ . For these four wavelengths, the largest beam size of  $\sim 12''$  corresponds to the  $160 \mu\text{m}$  data. We therefore convolve the  $70 \mu\text{m}$ ,  $100 \mu\text{m}$ , and  $350 \mu\text{m}$  data to a resolution matching the  $160 \mu\text{m}$  observations and extract a beam-smoothed SED. We then fit this SED in the same way as described above. Compared to the non-convolved SED modified black-body fitting results, we find that the temperature decreases by  $\sim 4\%$ , the luminosity increases by  $\sim 10\%$ , and the mass in the thermal component increases by  $\sim 30\%$ . These systematic shifts are similar to but somewhat larger than the errors quoted in Table 8 ( $\sim 2\%$  on the temperature,

$\sim 10\%$  on the luminosity, and  $\sim 30\%$  on the mass). We note, however, that the errors quoted in Table 8 are purely random and do not include any systematic component. We therefore conclude that extracting SEDs from images matched to a resolution of  $\sim 12''$  will not greatly affect our results.

Modified black-body fits provide a somewhat limited means of analysis of our sources since the model assumes a single temperature and density along the line of sight for the emitting material. We expect that the assumption of a single line-of-sight temperature will cause an underestimate of the source masses (e.g., Nielbock et al. 2012; Launhardt et al. 2012). However, radiative transfer models have large ambiguities in the assumed source temperature and density structure, leading to mass estimates that strongly model-dependent. Furthermore, the dust law that is assumed will introduce significant uncertainties into the derived masses, irrespective of the analysis method that is implemented. For example, the masses listed in Table 8 increase by a factor of  $\sim 4$  on average when we assume Draine & Lee (1984)  $R_V = 3.1$  ISM-like dust. These issues indicate that the masses derived here represent lower limits to the true envelope masses. Nevertheless, we consider the modified black-body fits to the measured photometry to provide the most robust estimates of the mass that we currently have.

We note that with only 5 SED flux points at best, fitting a multiple component (modified) black-body model cannot be justified. Since most of the mass is located at relatively large scales and expected to have cold temperatures, excluding the warmer shorter wavelength data arising from inner material will not significantly increase the masses we derive. The modified black-body fits thus to provide an approximate measurement of the optical-depth averaged gross properties of the envelopes being investigated. These issues point to the need for a more sophisticated modeling approach that will be carried out in future work.

## 7. DISCUSSION

As seen in Figure 11, the observed 70/24 colors of a protostar can be driven towards redder values through various strongly degenerate parameters. For example, the total column of material along the line-of-sight (LOS) towards a given protostar can have multiple contributions: the attenuation of the mid-IR emission by dense foreground material, the density of the envelope, the amount of envelope flattening, the opening angle of the outflow cavity, and the source inclination. Furthermore, the assumed model central protostar mass remains largely unconstrained by observations to date and can affect the interpretation of the 70/24 colors.

Foreground extinction can have various contributions, such as intervening dust between the observer and the cloud and dense material associated with the cloud itself, such as filamentary material. Of these two components, the first is expected to be relatively small, while the latter can be expected to vary from source to source by relatively large amounts, with a corresponding effect on the observed colors. For example, some PBRs are located in filamentary regions (e.g., Figures 7 and 8), while others appear more isolated (e.g., see Appendix for Figure 20). We have estimated the effects of foreground extinction levels up to a level of  $A_V = 40$  mag, and find that the

values of  $L_{\text{bol}}$ ,  $L_{\text{smm}}$ , and  $T_{\text{bol}}$  not significantly affected.

On the other hand, the effects of source inclination are not as straightforward to assess. When considering the presence of flattened rotating envelopes, disks, and outflow cavities, the source inclination will have a large effect on the observed source SED, as illustrated by the model tracks shown in Figure 11 (see also, e.g., Whitney et al. 2003a; De Buizer et al. 2005; Offner et al. 2012).

Therefore, it appears that the very red PBRs can be explained by multiple effects that all result in increasingly red observed 70/24 colors. These very red colors may be driven by elevated envelope densities (or equivalently,  $\dot{M}_{\text{env}}$ ), high source inclinations, or elevated levels of extinction associated with structures larger than the envelope-protostar system. The current data and SED coverage do not allow us to break these degeneracies conclusively. Furthermore, we consider it likely that the red observed colors are not driven any single cause, but instead are the result of several.

We have, however, designed our PBRs selection to find the densest envelopes in Orion (c.f., Figure 11). Furthermore, the effect of external foreground extinction is not expected to be large at these long wavelengths, even with elevated levels of material along the LOS (see above). Indeed, we have also shown that the PBRs require a central heating source, indicating that the detection of a  $70 \mu\text{m}$  point source drives the interpretation of the sample as Class 0 sources, irrespective of source inclination. However, we note that if the central masses are significantly different than the assumed value of  $0.5 M_{\odot}$ , then for a fixed reference envelope density the inferred envelope infall rates need to be scaled accordingly (see Equation 1).

To further investigate the evolutionary state of the PBRs, in Figure 14 we show the values of  $L_{\text{bol}}$ ,  $T_{\text{bol}}$ , and  $L_{\text{smm}}/L_{\text{bol}}$  for the entire sample of new candidate protostars and the previously identified *Spitzer* HOPS sample (Fischer et al. in preparation). In the left panel, we show  $L_{\text{bol}}$  vs.  $T_{\text{bol}}$  for the entire sample of new protostar candidates, including those flagged as possible extra-galactic contamination. We also show the four reference Class 0 sources presented in Table 8. The PBRs sample in particular, and the entire sample of new candidate protostars, are generally clustered around low  $T_{\text{bol}}$  values. Ignoring inclination degeneracies and other considerations, these low  $T_{\text{bol}}$  values indicate that the PBRs sample is indeed composed of young Class 0 sources. In the right panel, we show  $T_{\text{bol}}$  vs.  $L_{\text{smm}}/L_{\text{bol}}$  for the sources with sufficient coverage to estimate  $L_{\text{smm}}$  (see § 6.2). The PBRs, as expected if the sample can be explained as Class 0 sources, cluster around larger values of  $L_{\text{smm}}/L_{\text{bol}}$  compared to the rest of the sample. André et al. (2000) proposed the  $L_{\text{smm}}/L_{\text{bol}} > 0.5\%$  threshold for Class 0 sources, and all but one of the new candidate protostars for which we can estimate  $L_{\text{smm}}$  fall into this category. Irrespective of the evolutionary indicator that is chosen ( $T_{\text{bol}}$  or  $L_{\text{smm}}/L_{\text{bol}}$ ), all of the new candidate protostars in both the reliable and lower probability categories (green and yellow points, respectively), would be considered of Class 0 status. Finally, while the PBRs 70/24  $> 1.65$  color criterion causes some sources with very low values of  $T_{\text{bol}}$  and very high values of  $L_{\text{smm}}/L_{\text{bol}}$  to be missed, the color selection is able to capture the vast majority of the most extreme Class 0

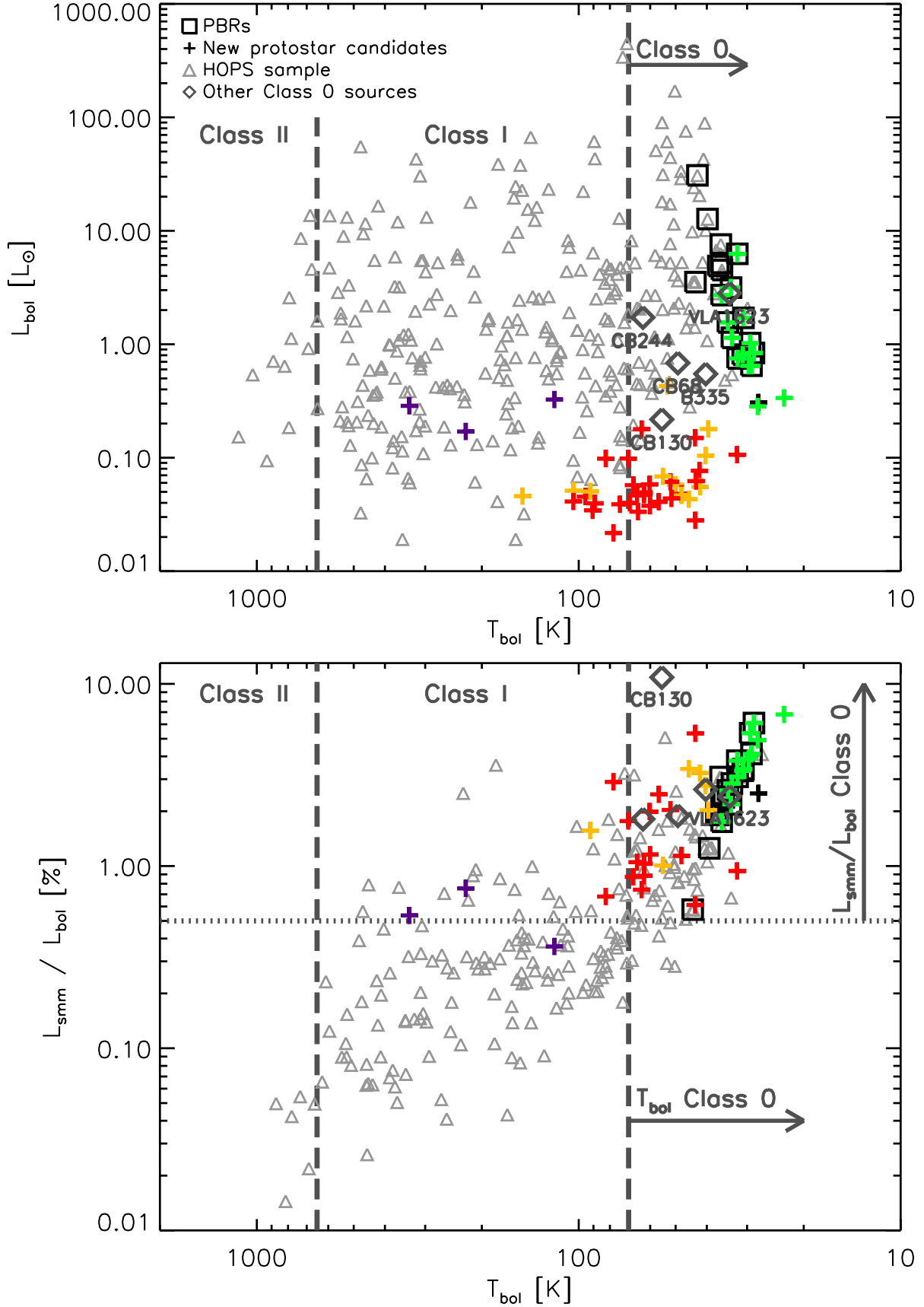


FIG. 14.— Left: Bolometric luminosity vs. bolometric temperature for the new candidate protostars (+-symbols) and the HOPS protostars (light-grey triangles). The squares indicate the PBRs sample, drawn from both the new candidate protostar sample and the HOPS protostar sample. The dashed lines indicate the canonical  $T_{\text{bol}}$  divisions between protostellar Classes. Right:  $L_{\text{smm}}/L_{\text{bol}}$  vs bolometric temperature for the subset of sources shown in the left panel for which we have sufficient submillimeter coverage to estimate  $L_{\text{smm}}$  (see text). The horizontal dotted line indicates the André et al. (2000) proposed  $L_{\text{smm}}/L_{\text{bol}} > 0.5\%$  Class 0 threshold.



243. AMS kindly acknowledges helpful and insightful discussions with Ralf Launhardt. The work of AMS was supported by the Deutsche Forschungsgemeinschaft priority program 1573 ("Physics of the Interstellar Medium"). JT acknowledges support provided by NASA through Hubble Fellowship grant #HST-HF-51300.01-A awarded by the Space Telescope Science Institute, which is operated by the Association of Universities for Research in Astronomy, Inc., for NASA, under contract NAS 5-26555. The National Radio Astronomy Observatory is a facility of the National Science Foundation operated under cooperative agreement by Associated Universities, Inc. This publication is based on data acquired with the Atacama Pathfinder Experiment (APEX). APEX is a collaboration between the Max-Planck-Institut für Radioastronomie, the European Southern Observatory, and the Onsala Space Observatory. The *Herschel* spacecraft was designed, built, tested, and launched under a contract to ESA managed by the Herschel/Planck Project team by an industrial consortium under the overall responsibility of the prime contractor Thales Alenia Space (Cannes), and including Astrium (Friedrichshafen) responsible for the payload module and for system testing at spacecraft level, Thales Alenia Space (Turin) responsible for the service mod-

ule, and Astrium (Toulouse) responsible for the telescope, with in excess of a hundred subcontractors. PACS has been developed by a consortium of institutes led by MPE (Germany) and including UVIE (Austria); KU Leuven, CSL, IMEC (Belgium); CEA, LAM (France); MPIA (Germany); INAF-IFSI/OAA/OAP/OAT, LENS, SISSA (Italy); IAC (Spain). This development has been supported by the funding agencies BMVIT (Austria), ESA-PRODEX (Belgium), CEA/CNES (France), DLR (Germany), ASI/INAF (Italy), and CICYT/MCYT (Spain). HCSS / HSpot / HIPE is a joint development (are joint developments) by the Herschel Science Ground Segment Consortium, consisting of ESA, the NASA Herschel Science Center, and the HIFI, PACS and SPIRE consortia. We also use the Spitzer Space Telescope and the Infrared Processing and Analysis Center (IPAC) Infrared Science Archive, which are operated by JPL/Caltech under a contract with NASA. This research has made use of the SIMBAD database and Vizier catalogue access tool, operated at CDS, Strasbourg, France. Support for this work was provided by the National Aeronautics and Space Administration (NASA) through awards issued by the Jet Propulsion Laboratory, California Institute of Technology (JPL/Caltech).

## REFERENCES

- Ali, B., Tobin, J. J., Fischer, W. J., et al. 2010, *A&A*, 518, L119  
 Allen, L. E., Calvet, N., D'Alessio, P., et al. 2004, *ApJS*, 154, 363  
 André, P., Ward-Thompson, D., & Barsony, M. 1993, *ApJ*, 406, 122  
 —. 2000, *Protostars and Planets IV*, 59  
 André, P., Men'shchikov, A., Bontemps, S., et al. 2010, *A&A*, 518, L102  
 Aniano, G., Draine, B. T., Gordon, K. D., & Sandstrom, K. 2011, *PASP*, 123, 1218  
 Arce, H. G., & Sargent, A. I. 2006, *ApJ*, 646, 1070  
 Bally, J., Walawender, J., Reipurth, B., & Megeath, S. T. 2009, *AJ*, 137, 3843  
 Bourke, T. L., Myers, P. C., Evans, II, N. J., et al. 2006, *ApJ*, 649, L37  
 Cassen, P., & Moosman, A. 1981, *Icar*, 48, 353  
 Chen, X., Arce, H. G., Zhang, Q., et al. 2010, *ApJ*, 715, 1344  
 Chini, R., Reipurth, B., Ward-Thompson, D., et al. 1997, *ApJ*, 474, L135  
 Commerçon, B., Launhardt, R., Dullemond, C., & Henning, T. 2012, *A&A*, 545, A98  
 Da Rio, N., Robberto, M., Hillenbrand, L. A., Henning, T., & Stassun, K. G. 2012, *ApJ*, 748, 14  
 Davis, C. J., Dent, W. R. F., Matthews, H. E., Coulson, I. M., & McCaughrean, M. J. 2000, *MNRAS*, 318, 952  
 Davis, C. J., Froebrich, D., Stanke, T., et al. 2009, *A&A*, 496, 153  
 De Buizer, J. M., Osorio, M., & Calvet, N. 2005, *ApJ*, 635, 452  
 Di Francesco, J., Johnstone, D., Kirk, H., MacKenzie, T., & Ledwosinska, E. 2008, *ApJS*, 175, 277  
 Draine, B. T., & Lee, H. M. 1984, *ApJ*, 285, 89  
 Dunham, M. M., Crapsi, A., Evans, II, N. J., et al. 2008, *ApJS*, 179, 249  
 Dunham, M. M., Evans, II, N. J., Terebey, S., Dullemond, C. P., & Young, C. H. 2010, *ApJ*, 710, 470  
 Dunham, M. M., Evans, II, N. J., Bourke, T. L., et al. 2006, *ApJ*, 651, 945  
 Enoch, M. L., Evans, II, N. J., Sargent, A. I., & Glenn, J. 2009, *ApJ*, 692, 973  
 Enoch, M. L., Lee, J.-E., Harvey, P., Dunham, M. M., & Schnee, S. 2010, *ApJ*, 722, L33  
 Evans, II, N. J., Dunham, M. M., Jørgensen, J. K., et al. 2009, *ApJS*, 181, 321  
 Fang, M., van Boekel, R., Wang, W., et al. 2009, *A&A*, 504, 461  
 Fischer, W. J., Megeath, S. T., Ali, B., et al. 2010, *A&A*, 518, L122  
 Fischer, W. J., Megeath, S. T., Tobin, J. J., et al. 2012, *ApJ*, 756, 99  
 Flaherty, K. M., & Muzerolle, J. 2008, *AJ*, 135, 966  
 Flaherty, K. M., Pipher, J. L., Megeath, S. T., et al. 2007, *ApJ*, 663, 1069  
 Furlan, E., McClure, M., Calvet, N., et al. 2008, *ApJS*, 176, 184  
 Gibb, A. G., & Little, L. T. 2000, *MNRAS*, 313, 663  
 Gordon, K. D., et al. 2005, *PASP*, 117, 503  
 Gutermuth, R. A., Megeath, S. T., Myers, P. C., et al. 2009, *ApJS*, 184, 18  
 Gutermuth, R. A., Myers, P. C., Megeath, S. T., et al. 2008, *ApJ*, 674, 336  
 Hartmann, L. 2009, *Accretion Processes in Star Formation: Second Edition* (Cambridge University Press)  
 Harvey, P., Merin, B., Huard, T. L., et al. 2007, *ApJ*, 663, 1149  
 Haschick, A. D., Moran, J. M., Rodriguez, L. F., & Ho, P. T. P. 1983, *ApJ*, 265, 281  
 Hatchell, J., Fuller, G. A., Richer, J. S., Harries, T. J., & Ladd, E. F. 2007, *A&A*, 468, 1009  
 Hirota, T., Bushimata, T., Choi, Y. K., et al. 2007, *PASJ*, 59, 897  
 Hsu, W.-H., Hartmann, L., Allen, L., et al. 2012, *ApJ*, 752, 59  
 Johnston, K. G., Shepherd, D. S., Robitaille, T. P., & Wood, K. 2012, *A&A*, in press.  
 Johnstone, D., & Bally, J. 2006, *ApJ*, 653, 383  
 Johnstone, D., Fich, M., Mitchell, G. F., & Moriarty-Schieven, G. 2001, *ApJ*, 559, 307  
 Jørgensen, J. K., Johnstone, D., Kirk, H., & Myers, P. C. 2007, *ApJ*, 656, 293  
 Jørgensen, J. K., van Dishoeck, E. F., Visser, R., et al. 2009, *A&A*, 507, 861  
 Kenyon, S. J., & Hartmann, L. W. 1990, *ApJ*, 349, 197  
 Kenyon, S. J., Whitney, B. A., Gomez, M., & Hartmann, L. 1993, *ApJ*  
 Kim, S.-H., Martin, P. G., & Hendry, P. D. 1994, *ApJ*, 422, 164  
 Könyves, V., André, P., Men'shchikov, A., et al. 2010, *A&A*, 518, L106  
 Kryukova, E., Megeath, S. T., Gutermuth, R. A., et al. 2012, *AJ*, 144, 31  
 Lada, C. J. 1987, in *IAU Symposium, Vol. 115, Star Forming Regions*, ed. M. Peimbert & J. Jugaku, 1–17  
 Lada, E. A. 1992, *ApJ*, 393, L25  
 Lada, E. A., Bally, J., & Stark, A. A. 1991a, *ApJ*, 368, 432  
 Lada, E. A., Depoy, D. L., Evans, II, N. J., & Gatley, I. 1991b, *ApJ*

- Lada, E. A., Evans, II, N. J., & Falgarone, E. 1997, *ApJ*, 488, 286
- Larson, R. B. 1969, *MNRAS*, 145, 271
- Launhardt, R., Mezger, P. G., Haslam, C. G. T., et al. 1996, *A&A*, 312, 569
- Launhardt, R., Stutz, A., Schmiedeke, A., et al. 2012, *A&A*, in press.
- Launhardt, R., Nutter, D., Ward-Thompson, D., et al. 2010, *ApJS*, 188, 139
- Levreault, R. M. 1988, *ApJS*, 67, 283
- Lis, D. C., Menten, K. M., & Zylka, R. 1999, *ApJ*, 527, 856
- Manoj, P., Watson, D. M., Neufeld, D. A., et al. 2012, *ApJ*, in press.
- Mathis, J. S., Mezger, P. G., & Panagia, N. 1983, *A&A*, 128, 212
- Megeath, S. T., Allen, L. E., Gutermuth, R. A., et al. 2004, *ApJS*, 154, 367
- Megeath, S. T., et al. 2012, Accepted to *ApJ*
- Men'shchikov, A., André, P., Didelon, P., et al. 2010, *A&A*, 518, L103
- Menten, K. M., Reid, M. J., Forbrich, J., & Brunthaler, A. 2007, *A&A*, 474, 515
- Mezger, P. G., Zylka, R., & Wink, J. E. 1990, *A&A*, 228, 95
- Miettinen, O., Harju, J., Haikala, L. K., & Juvela, M. 2010, *A&A*, 524, A91
- . 2012, *A&A*, 538, A137
- Miettinen, O., Harju, J., Haikala, L. K., Kainulainen, J., & Johansson, L. E. B. 2009, *A&A*, 500, 845
- Mitchell, G. F., Johnstone, D., Moriarty-Schieven, G., Fich, M., & Tothill, N. F. H. 2001, *ApJ*, 556, 215
- Mookerjee, B., Sandell, G., Jarrett, T. H., & McMullin, J. P. 2009, *A&A*, 507, 1485
- Morgan, J. A., Schloerb, F. P., Snell, R. L., & Bally, J. 1991, *ApJ*, 376, 618
- Motte, F., André, P., Ward-Thompson, D., & Bontemps, S. 2001, *A&A*, 372, L41
- Myers, P. C., Adams, F. C., Chen, H., & Schaff, E. 1998, *ApJ*, 492, 703
- Myers, P. C., & Ladd, E. F. 1993, *ApJ*, 413, L47
- Nielbock, M., Chini, R., & Müller, S. A. H. 2003, *A&A*, 408, 245
- Nielbock, M., Launhardt, R., Steinacker, J., et al. 2012, *A&A*, 547, A11
- Noriega-Crespo, A., Moro-Martin, A., Carey, S., et al. 2004, *ApJS*, 154, 402
- Nutter, D., & Ward-Thompson, D. 2007, *MNRAS*, 374, 1413
- Ochsenbein, F., Bauer, P., & Marcout, J. 2000, *A&AS*, 143, 23
- Offner, S. S. R., & McKee, C. F. 2011, *ApJ*, 736, 53
- Offner, S. S. R., Robitaille, T. P., Hansen, C. E., McKee, C. F., & Klein, R. I. 2012, *ApJ*, 753, 98
- Ormel, C. W., Min, M., Tielens, A. G. G. M., Dominik, C., & Paszun, D. 2011, *A&A*, 532, A43
- Ossenkopf, V., & Henning, T. 1994, *A&A*, 291, 943
- Padgett, D. L., Brandner, W., Stapelfeldt, K. R., et al. 1999, *AJ*, 117, 1490
- Pezzuto, S., Elia, D., Schisano, E., et al. 2012, *A&A*, 547, A54
- Phillips, R. R., Gibb, A. G., & Little, L. T. 2001, *MNRAS*, 326, 927
- Pilbratt, G. L., Riedinger, J. R., Passvogel, T., et al. 2010, *A&A*, 518, L1
- Pineda, J. E., Arce, H. G., Schnee, S., et al. 2011, *ApJ*, 743, 201
- Poglitsch, A., Waelkens, C., Geis, N., et al. 2010, *A&A*, 518, L2
- Porter, T. A., & Strong, A. W. 2005, in *International Cosmic Ray Conference*, Vol. 4, International Cosmic Ray Conference, 77
- Price, D. J., Tricco, T. S., & Bate, M. R. 2012, *MNRAS*, 423, L45
- Ragan, S., Henning, T., Krause, O., et al. 2012, *A&A*, 547, A49
- Reggiani, M., Robberto, M., Da Rio, N., et al. 2011, *A&A*, 534, A83
- Reipurth, B., Megeath, S. T., Bally, J., & Walawender, J. 2008, *The L1617 and L1622 Cometary Clouds in Orion*, ed. B. Reipurth, 782
- Reipurth, B., Rodríguez, L. F., & Chini, R. 1999, *AJ*, 118, 983
- Robitaille, T. P. 2011, *A&A*, 536, A79
- Robitaille, T. P., Meade, M. R., Babler, B. L., et al. 2008, *AJ*, 136, 2413
- Roussel, H. 2012, *ArXiv e-prints*: 1205.2576, submitted to *PASP*
- Sadavoy, S. I., Di Francesco, J., Bontemps, S., et al. 2010, *ApJ*, 710, 1247
- Sandstrom, K. M., Peek, J. E. G., Bower, G. C., Bolatto, A. D., & Plambeck, R. L. 2007, *ApJ*, 667, 1161
- Savva, D., Little, L. T., Phillips, R. R., & Gibb, A. G. 2003, *MNRAS*, 343, 259
- Schuller, P., et al. 2012, in prep.
- Siringo, G., Kreysa, E., Kovács, A., et al. 2009, *A&A*, 497, 945
- Siringo, G., Kreysa, E., De Breuck, C., et al. 2010, *The Messenger*, 139, 20
- Sodroski, T. J., Odegard, N., Arendt, R. G., et al. 1997, *ApJ*, 480, 173
- Stanke, T., McCaughrean, M. J., & Zinnecker, H. 2002, *A&A*, 392, 239
- Stanke, T., Stutz, A. M., Tobin, J. J., et al. 2010, *A&A*, 518, L94
- Stern, D., Eisenhardt, P., Gorjian, V., et al. 2005, *ApJ*, 631, 163
- Strom, K. M., Strom, S. E., & Vrba, F. J. 1976, *AJ*, 81, 308
- Strom, K. M., Strom, S. E., Wolff, S. C., Morgan, J., & Wenz, M. 1986, *ApJS*, 62, 39
- Stutz, A., Launhardt, R., Linz, H., et al. 2010, *A&A*, 518, L87
- Stutz, A. M., et al. 2008, *ApJ*, 687, 389
- Terebey, S., Shu, F. H., & Cassen, P. 1984, *ApJ*, 286, 529
- Tobin, J. J., Hartmann, L., Chiang, H.-F., et al. 2012, *Nature*, 492, 83
- Tobin, J. J., Looney, L. W., Mundy, L. G., Kwon, W., & Hamidouche, M. 2007, *ApJ*, 659, 1404
- Tsujimoto, M., Koyama, K., Kobayashi, N., et al. 2003, *AJ*, 125, 1537
- Ulrich, R. K. 1976, *ApJ*, 210, 377
- Whitney, B. A., Wood, K., Bjorkman, J. E., & Cohen, M. 2003b, *ApJ*, 598, 1079
- Whitney, B. A., Wood, K., Bjorkman, J. E., & Wolff, M. J. 2003a, *ApJ*, 591, 1049
- Williams, J. P., & Cieza, L. A. 2011, *ARA&A*, 49, 67
- Winston, E., Megeath, S. T., Wolk, S. J., et al. 2007, *ApJ*, 669, 493
- Wu, Y., Wei, Y., Zhao, M., et al. 2004, *A&A*, 426, 503
- Young, C. H., & Evans, II, N. J. 2005, *ApJ*, 627, 293
- Zavagno, A., Molinari, S., Tommasi, E., Saraceno, P., & Griffin, M. 1997, *A&A*, 325, 685

## APPENDIX

## PREVIOUS PBRs DETECTIONS

We searched the SIMBAD and VizieR (Ochsenbein et al. 2000) services for previous identifications of the PBRs. We restricted our search to a radius of  $20''$  from the  $70\ \mu\text{m}$  source coordinates. The results are summarized in Table 6. This list is likely incomplete and is intended to provide a resource and rough guide to some of the previous detections of these sources.

- 061012, 119019, and 097002: None found.
- HOPS169: Known protostar and outflow bipolar outflow V380 Ori NE (e.g., Davis et al. 2000). Stanke et al. (2002) detected source 59 in their  $2.12\ \mu\text{m}$  catalog of Orion A, offset by  $6''$  from our source coordinates. Davis et al. (2009) also detected an outflow about  $2''$  away from our coordinates. Nutter & Ward-Thompson (2007) classified this source as hosting a young stellar object (YSO) and measured an  $850\ \mu\text{m}$ -flux-derived mass of  $2.8\ M_{\odot}$  (assuming a temperature of 20 K and a distance of 400 pc).
- 019003: Since this source is located in the very crowded and complex ONC filament, it is often not clear which previous identifications may be associated with it in particular. Tsujimoto et al. (2003) listed a near-IR source located

3.35'' away from our coordinates. Nutter & Ward-Thompson (2007) detected a source offset by 8.4''; they classified it as hosting a YSO and measure a mass of 6.2  $M_{\odot}$ . While it is not clear if the detection is associated with the PBRs we consider it probable. Chini et al. (1997) and Nielbock et al. (2003) likely detected this source in their 1.3 mm maps near FIR1a in OMC-2, although their beam sizes were too large identify the source unambiguously.

- 082005: This source was previously classified as a starless core (e.g., Johnstone & Bally 2006; Nutter & Ward-Thompson 2007; Mookerjee et al. 2009). The Nutter & Ward-Thompson (2007) location of the source is about 8'' away from our source with an associated mass of 3.3  $M_{\odot}$ . Mookerjee et al. (2009) measured a mass of 4.3  $M_{\odot}$  for this source.

- HOPS372 and 082012: These sources have coordinates that are significantly offset from the Nutter & Ward-Thompson (2007) coordinates; the two sources are unresolved and lie about 13'' away from their catalog entree, with a mass of 12.7  $M_{\odot}$ . The Mookerjee et al. (2009) analysis derived a mass of 1  $M_{\odot}$  for 082012 (MM1) and 7.4  $M_{\odot}$  for HOPS372 (MM2), from modified black-body fits to long-wavelength SEDs.

- 090003: Miettinen et al. (2009) detected this source (SMM3) in their 850  $\mu\text{m}$  map, and concluded that it is a promising Class 0 candidate based on the shape of the SED. They calculated a mass of about 7.5  $M_{\odot}$  for this source. Miettinen et al. (2010) and Miettinen et al. (2012) also observed this source in various molecular line transitions and with SABOCA at 350  $\mu\text{m}$ ; their measured flux for this source is  $S_{350}^{\text{peak}} = 3.63 \text{ Jy beam}^{-1}$ . We include their flux measurement and the 350  $\mu\text{m}$  map in our analysis.

- HOPS358: Strom et al. (1976), Strom et al. (1986), and (Reipurth et al. 1999) detected the Herbig-Haro complex HH24-26, with HH25 located about 10'' away from HOPS358. This source is also included in the Wu et al. (2004) high velocity outflow catalog. Nutter & Ward-Thompson (2007) classified a nearby source (11'' away) as a starless core with a mass of 6.3  $M_{\odot}$ .

- 091015 and 091016: These sources were detected by Lis et al. (e.g., 1999) at 1.3 mm and 350  $\mu\text{m}$  (as sources 5 and 6). The reported masses are  $\sim 2 M_{\odot}$  for each source. Both sources are classified as starless by Nutter & Ward-Thompson (2007), with catalog masses of 0.8  $M_{\odot}$  (091015) and 1.3  $M_{\odot}$  (091016).

- HOPS373 and 093005: Both sources were classified as starless by Nutter & Ward-Thompson (2007), with reported masses of 4.2  $M_{\odot}$  (HOPS373) and 3.9  $M_{\odot}$  (093005). Motte et al. (2001) observed this region at 450 and 850  $\mu\text{m}$  and also classified 093005 as a starless core, based on the lack of evidence for an embedded source. Source HOPS373, on the other hand, is known to be driving a CO outflow (Gibb & Little 2000), and therefore has been classified as a candidate Class 0 source. Furthermore, Haschick et al. (1983) identified a water maser near the HOPS373 location.

- 302002: Nutter & Ward-Thompson (2007) reported a mass of 2.7  $M_{\odot}$  and classified this source as protostellar. Phillips et al. (2001) classify this source (LBS18S) as pre-protostellar, however.

- HOPS359: Nutter & Ward-Thompson (2007) classified this source as protostellar and measure a mass of 2.7  $M_{\odot}$ .

- HOPS341: This source is strongly blended with HOPS340. We have listed some detections of the combined system in Table 6.

- HOPS354: Reipurth et al. (2008) described this source in the context of the L1622 cloud. Bally et al. (2009) also detected this source in their analysis of *Spitzer* IRAC images but did not analyze it in detail.

## GALLERY OF IMAGES OF PACS BRIGHT RED SOURCES

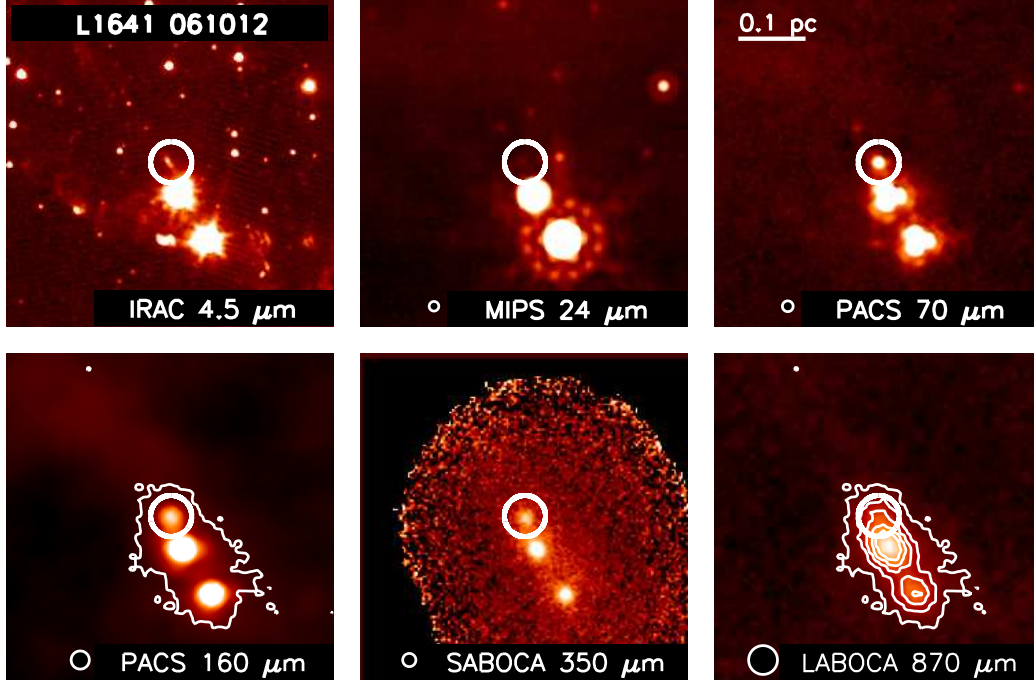


FIG. 15.— Same as Figure 7, showing  $4' \times 4'$  images of PBRs 061012. The IRAC-band emission associated with the source is clearly visible at  $4.5 \mu\text{m}$ . Contours indicate the  $870 \mu\text{m}$  emission levels at  $\{0.1, 0.25, 0.4, 0.55, 0.7\} \text{ Jy beam}^{-1}$ ; the long wavelength sum-mm data trace the cold envelope material associated with the source. The  $160 \mu\text{m}$  panel is shown with the lowest  $870 \mu\text{m}$  emission contour.

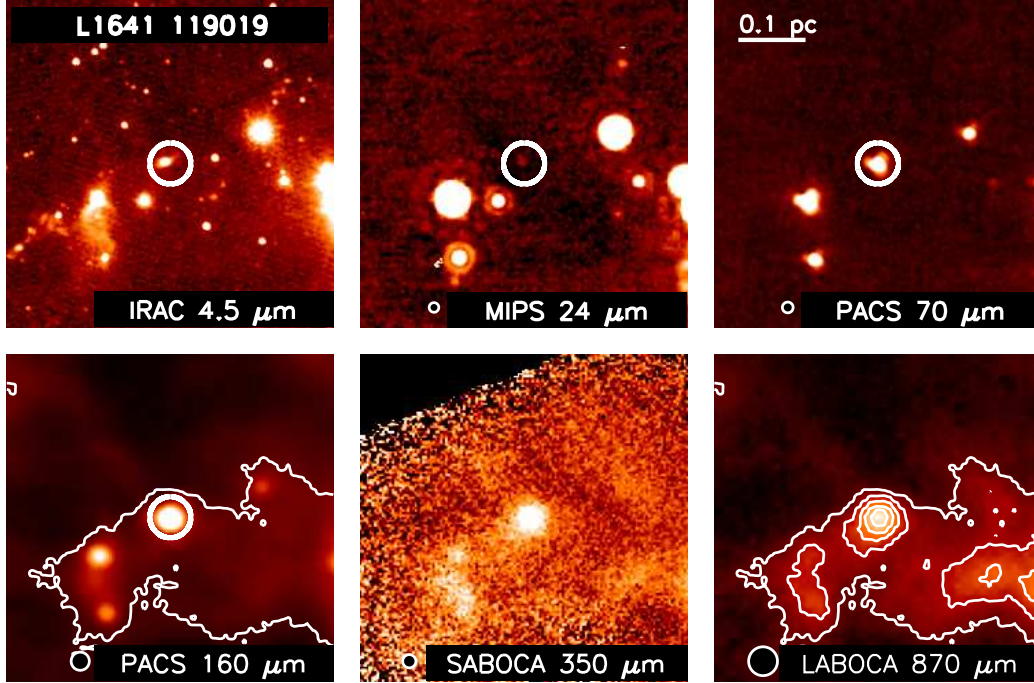


FIG. 16.— Same as Figure 7, showing  $4' \times 4'$  images and SED of PBRs 119019. Contours indicate the  $870 \mu\text{m}$  emission levels at  $\{0.1, 0.2, 0.3, 0.4, 0.5\} \text{ Jy beam}^{-1}$ . This source has prominent IRAC emission and is located in an IRAC  $8 \mu\text{m}$  and MIPS  $24 \mu\text{m}$  shadow.

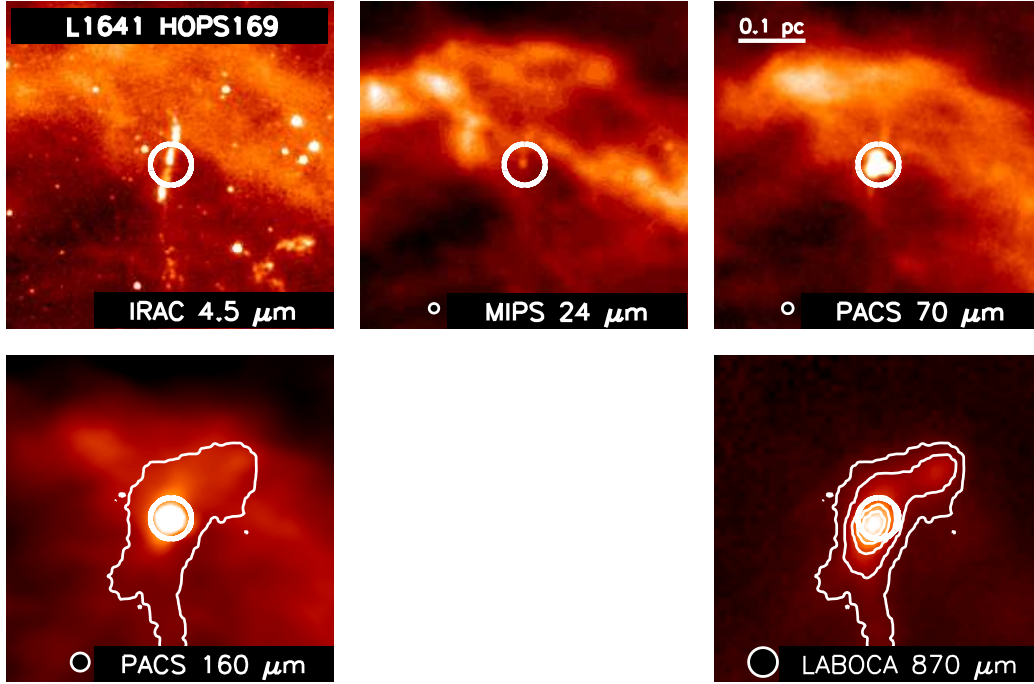


FIG. 17.— Same as Figure 7, showing  $4' \times 4'$  images and SED of HOPS169. Contours indicate the 870  $\mu\text{m}$  emission levels at  $\{0.1, 0.2, 0.4, 0.6, 0.8\}$   $\text{Jy beam}^{-1}$ . This source has clear outflow activity, traced by the IRAC emission, and appears to be at high inclination.

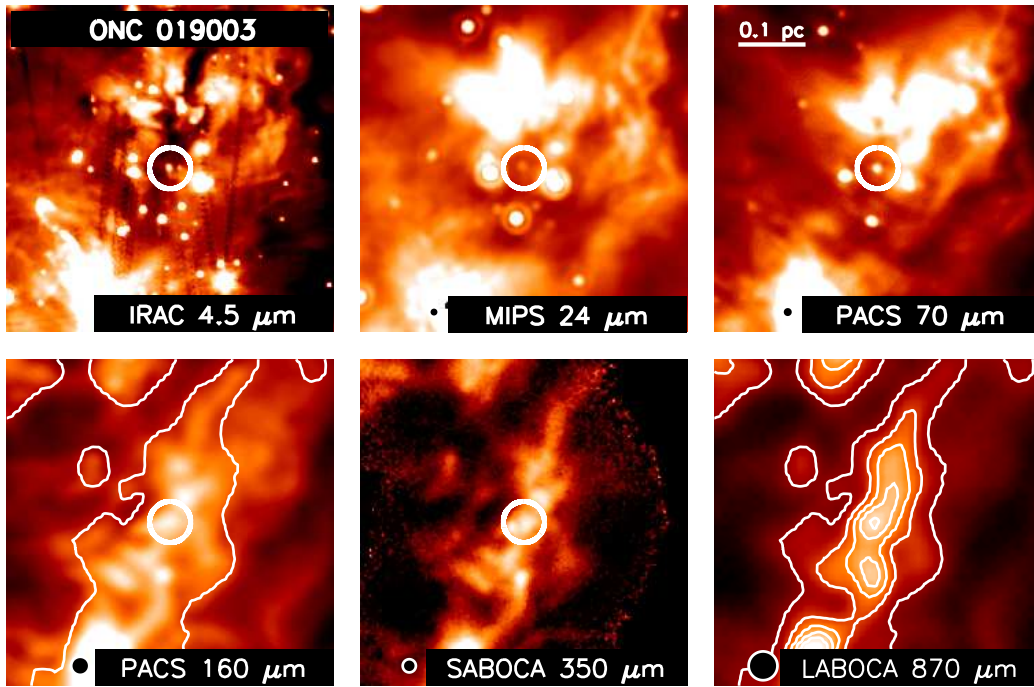


FIG. 18.— Same as Figure 7, showing  $4' \times 4'$  images and SED of PBR source 019003. Contours indicate the 870  $\mu\text{m}$  emission levels at  $\{0.5, 1.0, 1.5, 2.0, 2.5\}$   $\text{Jy beam}^{-1}$ . This source has indications outflow activity, as traced by the IRAC emission. The *Herschel* photometry may be strongly affected by blending due to the source location in a very dense filament.

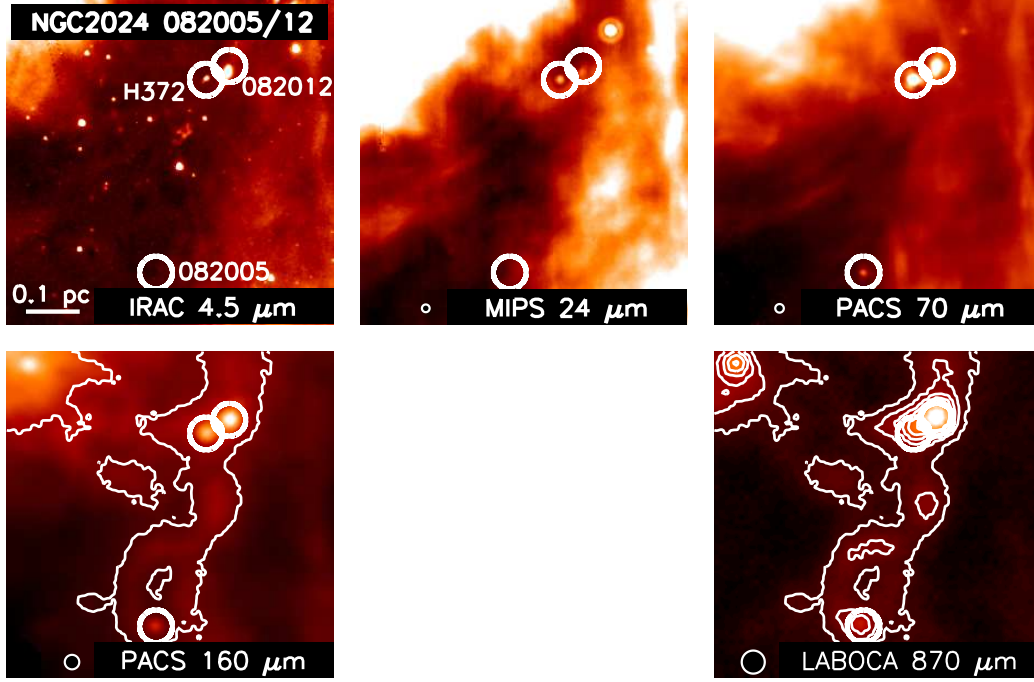


FIG. 19.— Top: Same as Figure 7, showing  $5' \times 5'$  images of three red sources: HOPS372 and 082012 (top) and 082005 (bottom). Contours indicate the 870  $\mu\text{m}$  emission levels at  $\{0.25, 0.5, 0.75, 1.0, 1.25, 1.5\}$  Jy beam $^{-1}$ . No IRAC emission is detected for 082005; however, this source is located in dense filamentary material traced by the sub-mm emission and an 8  $\mu\text{m}$  absorption feature.

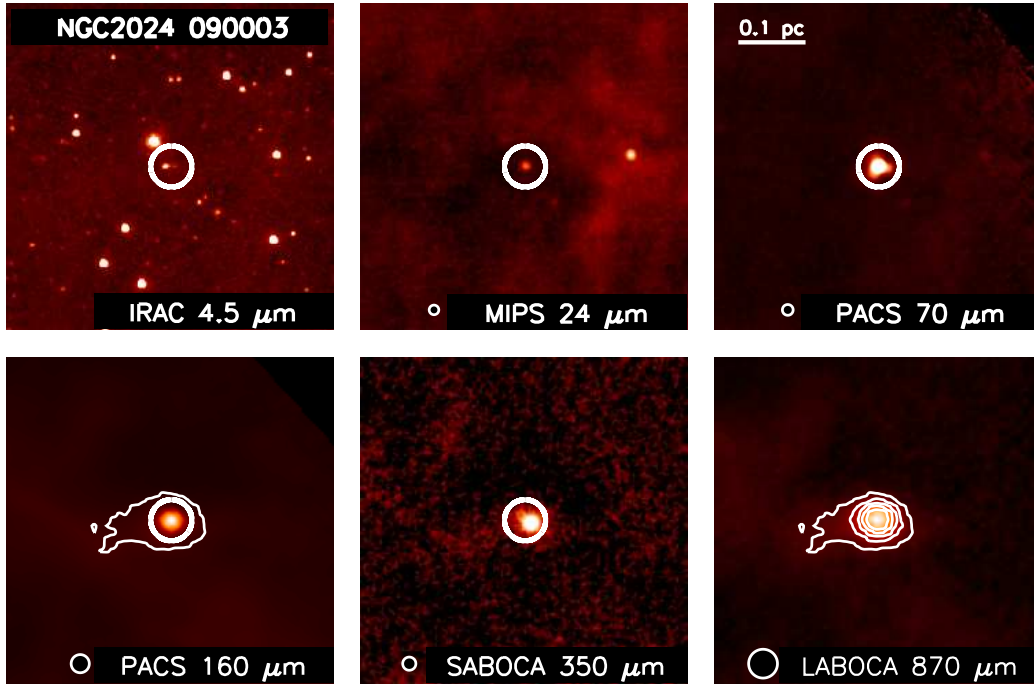


FIG. 20.— Same as Figure 7, showing  $4' \times 4'$  images and SED of PBRs 090003. Contours indicate the 870  $\mu\text{m}$  emission levels at  $\{0.25, 0.5, 0.75, 1.0, 1.25, 1.5\}$  Jy beam $^{-1}$ . The IRAC data show faint indications of extended emission, possibly associated with an outflow activity or a second source. The 350  $\mu\text{m}$  image and SED point are from Miettinen et al. (2012)

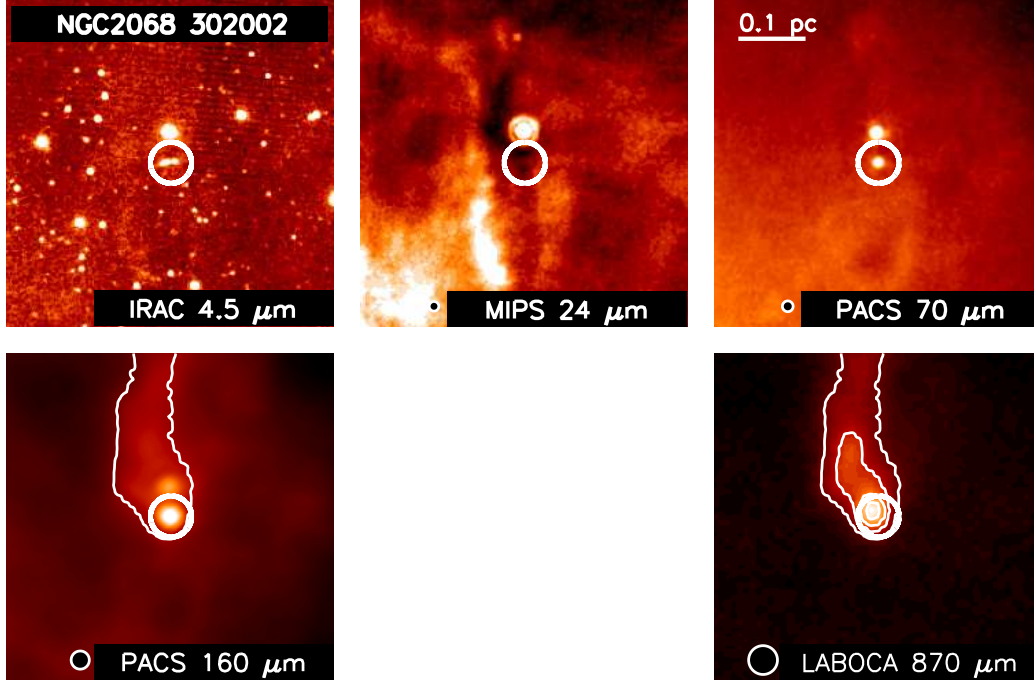


FIG. 21.— Same as Figure 7;  $4' \times 4'$  images of PBRs 302002. Contours indicate the  $870 \mu\text{m}$  emission levels at  $\{0.25, 0.5, 0.75, 1.0, 1.25, 1.5\} \text{ Jy beam}^{-1}$ , tracing the cometary globule shaped region. The IRAC data show indications of emission associated with outflow activity; furthermore, the  $4.5 \mu\text{m}$  data show evidence that this source is observed at high inclination. This source is the second most massive source in our sample, with a best-fit  $M_{\text{env}} = 1.7 M_{\odot}$ .

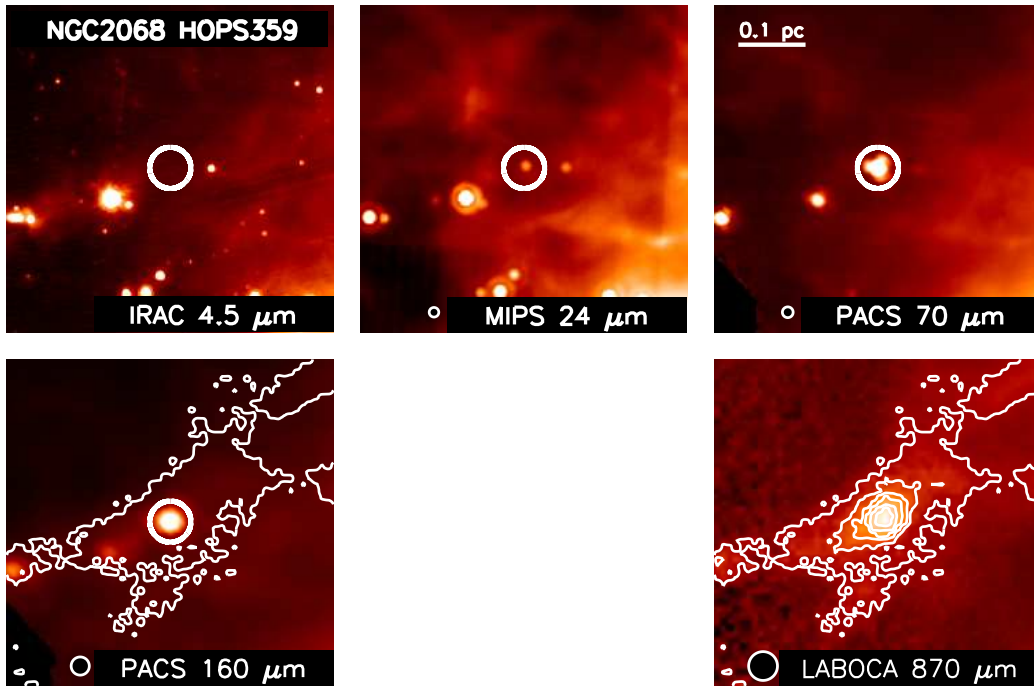


FIG. 22.— Same as Figure 7;  $4' \times 4'$  images of HOPS359. Contours indicate the  $870 \mu\text{m}$  emission levels at  $\{0.25, 0.5, 0.75, 1.0, 1.25, 1.5\} \text{ Jy beam}^{-1}$ .

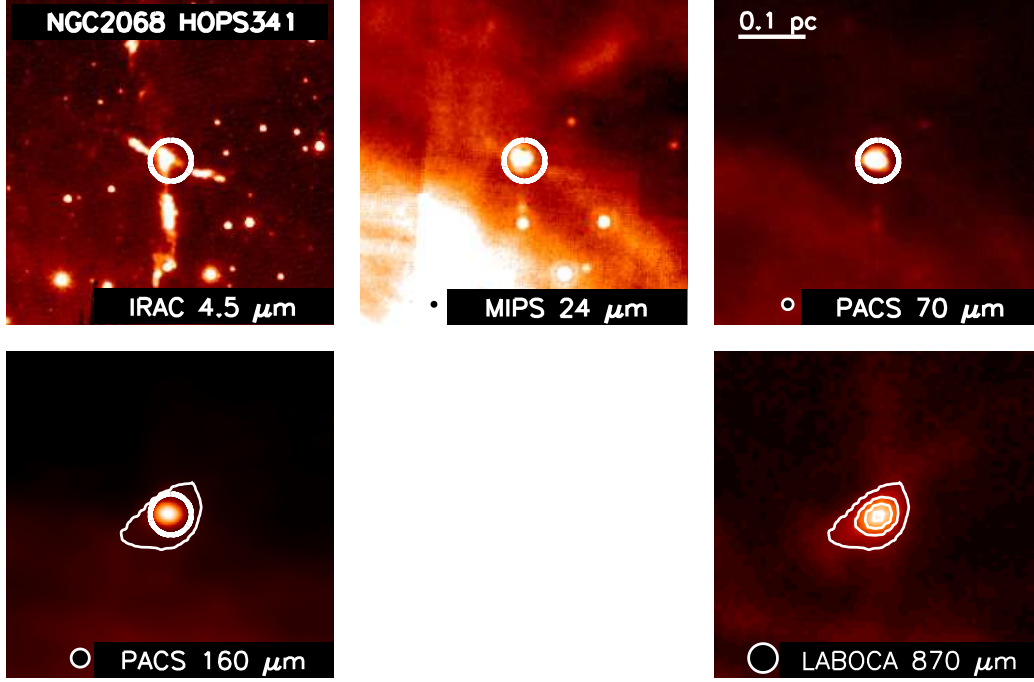


FIG. 23.— Same as Figure 7;  $4' \times 4'$  images of HOPS341. Contours indicate the  $870 \mu\text{m}$  emission levels at  $\{0.25, 0.5, 0.75, 1.0\} \text{ Jy beam}^{-1}$ . The x-shaped morphology of this source in the IRAC bands indicated that it is a binary. Indeed, the photometry of this source is strongly blended with HOPS340; nevertheless we include this source in our sample for completeness.

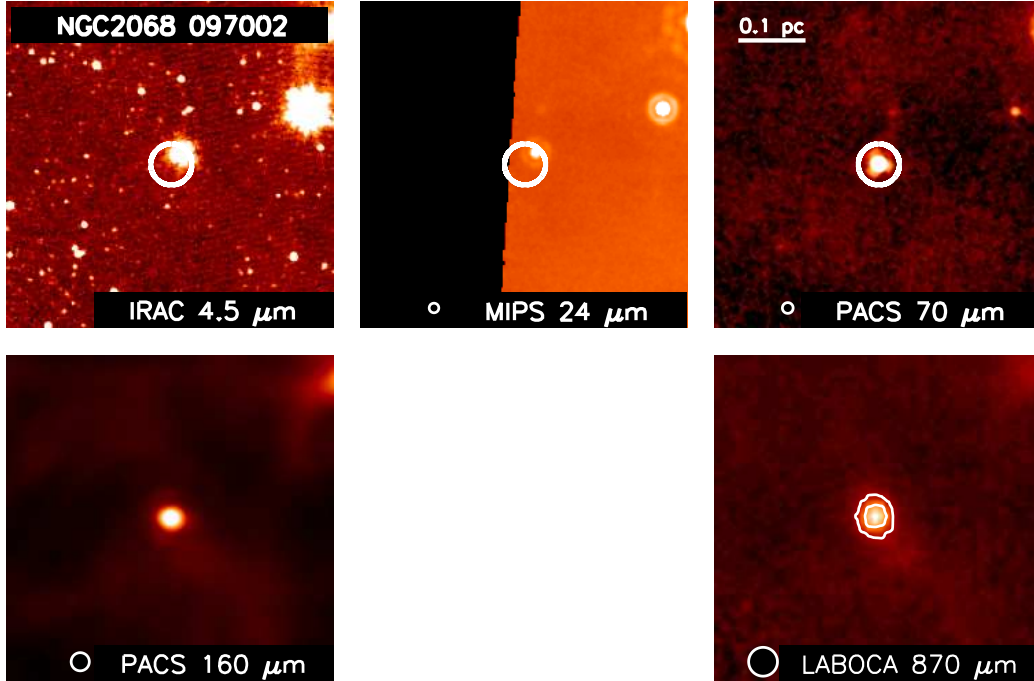


FIG. 24.— Same as Figure 7;  $4' \times 4'$  images of PBRs 097002. Contours indicate the  $870 \mu\text{m}$  emission levels at  $\{0.25, 0.5\} \text{ Jy beam}^{-1}$ .

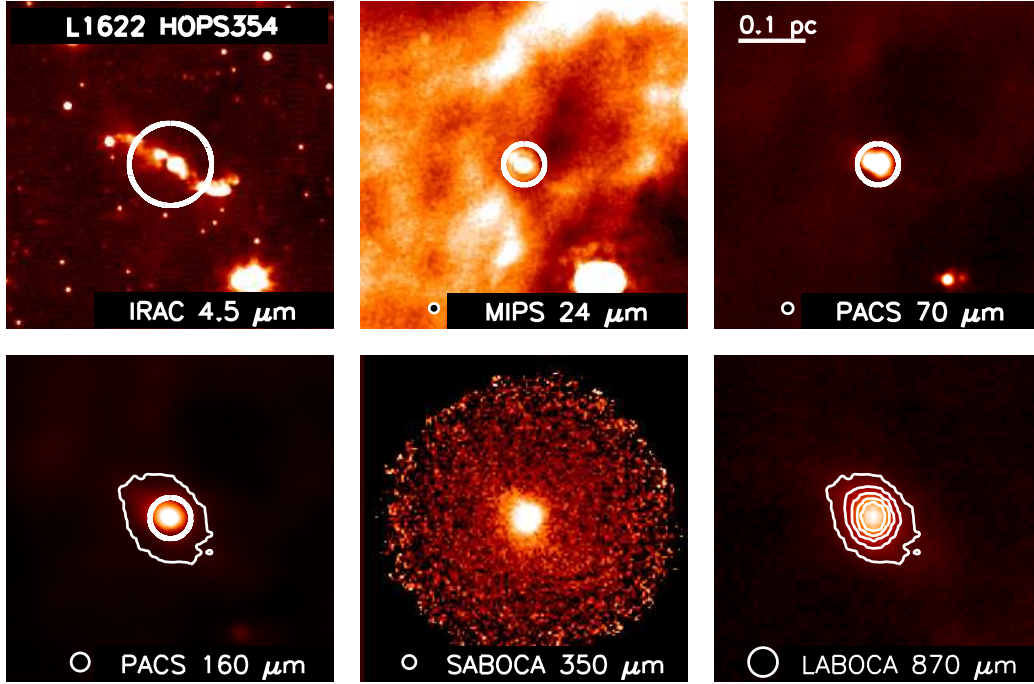


FIG. 25.— Same as Figure 7;  $4' \times 4'$  images of HOPS354. Contours indicate the 870  $\mu\text{m}$  emission levels at  $\{0.25, 0.5, 0.75, 1.0, 1.25\}$   $\text{Jy beam}^{-1}$ . The IRAC images display clear indications of outflow activity; furthermore the source appears highly inclined.

TABLE 1  
SUMMARY OF HOPS *Herschel* PACS L1641 OBSERVATIONS

HOPS group name	R.A. <sup>a</sup> h:m:s	Decl. <sup>a</sup> °:′:″	Field	AOR ID	OD	Map size ′ × ′
54	5:42:38.570	−8:50:18.67	L1641	1342218796(7)	704	8×8
53	5:43:06.770	−8:46:09.56	L1641	1342218735(6)	703	8×8
60	5:41:29.690	−8:41:28.59	L1641	1342215359(60)	662	8×8
55	5:42:50.490	−8:40:54.73	L1641	1342218798(9)	704	8×8
56	5:42:52.750	−8:37:20.98	L1641	1342205256(7)	502	8×8
117	5:41:33.250	−8:36:41.62	L1641	1342218790(1)	704	8×8
59	5:42:55.540	−8:32:48.26	L1641	1342218794(5)	704	8×8
58	5:43:09.580	−8:29:27.13	L1641	1342218788(9)	704	8×8
61	5:42:47.760	−8:16:50.72	L1641	1342205254(5)	502	8×8
67	5:40:20.130	−8:14:05.78	L1641	1342227078(9)	831	8×8
119	5:40:47.820	−8:10:28.38	L1641	1342206322(3)	516	8×8
62	5:42:47.370	−8:10:08.76	L1641	1342218792(3)	704	8×8
63	5:41:35.440	−8:08:22.49	L1641	1342218800(1)	704	8×8
66	5:40:54.500	−8:06:08.98	L1641	1342215361(2)	662	8×8
118	5:41:27.790	−8:04:03.70	L1641	1342205250(1)	502	8×8
78	5:38:51.480	−8:01:27.44	L1641	1342228169(70)	844	5×5
64	5:41:49.950	−8:01:26.51	L1641	1342205252(3)	502	5×5
69	5:40:38.330	−8:00:36.00	L1641	1342227080(1)	831	5×5
65	5:41:24.880	−8:00:02.34	L1641	1342215591(2)	663	8×8
72	5:40:20.710	−7:56:01.36	L1641	1342218733(4)	703	8×8
70	5:40:40.530	−7:54:39.82	L1641	1342228167(8)	844	5×5
121	5:41:23.440	−7:54:39.26	L1641	1342205248(9)	502	8×8
68	5:41:19.660	−7:50:41.03	L1641	1342227848(9)	842	5×5
74	5:40:17.690	−7:49:29.88	L1641	1342218731(2)	703	8×8
71	5:40:40.150	−7:49:18.71	L1641	1342228163(4)	844	8×8
320	5:40:58.890	−7:48:02.05	L1641	1342228165(6)	844	5×5
73	5:40:42.910	−7:45:01.91	L1641	1342228425(6)	847	5×5
75	5:40:24.620	−7:43:08.26	L1641	1342227082(3)	831	5×5
76	5:40:26.090	−7:37:32.02	L1641	1342205246(7)	502	5×5
79	5:39:57.200	−7:30:19.89	L1641	1342205244(5)	502	8×8
77	5:40:44.670	−7:29:54.46	L1641	1342228427(8)	847	5×5
123	5:40:08.780	−7:27:27.68	L1641	1342228161(2)	844	5×5
26	5:39:24.640	−7:26:13.81	L1641	1342218729(30)	703	8×8
25	5:39:56.200	−7:24:53.71	L1641	1342215589(90)	663	8×8
313	5:39:33.300	−7:22:57.36	L1641	1342227084(5)	831	5×5
28	5:38:56.470	−7:20:44.32	L1641	1342227086(7)	831	8×8
30	5:38:44.050	−7:11:49.89	L1641	1342204254(5)	484	8×8
29	5:39:06.710	−7:11:12.80	L1641	1342204252(3)	484	8×8
32	5:38:01.100	−7:07:37.01	L1641	1342227045(6)	830	8×8
312	5:38:46.540	−7:05:37.46	L1641	1342205242(3)	502	5×5
31	5:38:44.870	−7:00:37.03	L1641	1342204256(7)	484	8×8
33	5:38:20.090	−6:59:04.85	L1641	1342228171(2)	844	5×5
35	5:37:24.460	−6:58:32.77	L1641	1342227314(5)	833	5×5
34	5:37:59.990	−6:57:27.50	L1641	1342205240(1)	502	8×8
101	5:37:17.090	−6:49:49.33	L1641	1342227312(3)	833	5×5
36	5:37:52.390	−6:47:18.67	L1641	1342227088(9)	831	8×8
38	5:36:22.050	−6:45:41.23	L1641	1342205238(9)	502	8×8
40	5:36:26.650	−6:38:27.74	L1641	1342227094(5)	831	8×8
37	5:37:17.280	−6:36:18.18	L1641	1342227090(1)	831	8×8
43	5:35:50.020	−6:34:53.40	L1641	1342227310(1)	833	5×5
50	5:34:15.880	−6:34:32.70	L1641	1342217748(9)	686	8×8
39	5:36:41.330	−6:34:00.08	L1641	1342227092(3)	831	5×5
41	5:36:19.440	−6:29:06.79	L1641	1342227316(7)	833	5×5
45	5:35:34.120	−6:26:41.70	L1641	1342215593(4)	663	8×8
311	5:34:39.860	−6:25:14.16	L1641	1342203649(50)	470	5×5
42	5:36:22.460	−6:23:39.14	L1641	1342205236(7)	502	8×8
44	5:36:36.980	−6:14:57.98	L1641	1342204258(9)	484	5×5
51	5:35:22.180	−6:13:06.24	L1641	1342227318(9)	833	5×5
47	5:36:17.260	−6:11:11.00	L1641	1342227324(5)	833	5×5
49	5:35:52.000	−6:10:01.85	L1641	1342227322(3)	833	5×5
52	5:35:33.210	−6:06:09.65	L1641	1342227320(1)	833	5×5
48	5:36:31.360	−6:01:16.81	L1641	1342217444(5)	685	8×8
5	5:35:07.960	−5:56:56.40	L1641	1342204248(9)	484	8×8
6	5:35:24.560	−5:55:33.42	L1641	1342227328(9)	833	5×5
7	5:36:19.020	−5:55:25.46	L1641	1342227326(7)	833	5×5
8	5:35:04.400	−5:51:00.76	L1641	1342217446(7)	685	8×8
9	5:33:30.710	−5:50:41.03	L1641	1342217750(1)	686	8×8
10	5:36:10.100	−5:50:08.34	L1641	1342227096(7)	831	5×5
12	5:34:46.830	−5:42:28.72	L1641	1342204246(7)	484	8×8
13	5:35:17.340	−5:42:14.51	L1641	1342227098(9)	831	5×5
14	5:34:30.440	−5:37:47.44	L1641	1342204244(5)	484	8×8

<sup>a</sup> Field center coordinates.

TABLE 2  
SUMMARY OF HOPS *Herschel* PACS ONC, NGC2024, NGC2068, AND L1622  
OBSERVATIONS

HOPS group name	R.A. <sup>a</sup> h:m:s	Decl. <sup>a</sup> °:′:″	Region	AOR ID	OD	Map size ′ × ′
15	5:35:06.620	−5:35:05.68	ONC	1342205234(5)	502	8×8
308	5:33:45.870	−5:32:58.09	ONC	1342204433(4)	487	5×5
16	5:34:43.990	−5:32:11.21	ONC	1342217448(9)	685	8×8
17	5:35:16.320	−5:29:32.60	ONC	1342217450(1)	685	8×8
18	5:33:55.730	−5:22:39.97	ONC	1342217752(3)	686	8×8
200	5:35:19.270	−5:14:46.49	ONC	1342205232(3)	502	8×8
130	5:35:24.710	−5:09:06.02	ONC	1342205228(9)	502	8×8
135	5:35:26.280	−5:06:35.24	ONC	1342205226(7)	502	8×8
19	5:35:23.300	−5:00:35.73	ONC	1342204250(1)	484	8×8
20	5:35:13.770	−4:54:57.33	ONC	1342217758(9)	686	8×8
21	5:34:32.340	−4:53:54.26	ONC	1342217754(5)	686	8×8
306	5:35:32.280	−4:46:48.47	ONC	1342191970(1)	300	5×5
24	5:35:23.340	−4:40:10.45	ONC	1342217756(7)	686	8×8
80	5:40:51.710	−2:26:48.62	NGC2024	1342226729(30)	826	5×5
81	5:41:28.940	−2:23:19.36	NGC2024	1342226733(4)	826	5×5
82	5:41:23.740	−2:16:51.10	NGC2024	1342228913(4)	858	8×8
83	5:41:42.180	−2:16:26.20	NGC2024	1342227049(50)	830	8×8
85	5:42:02.620	−2:07:45.70	NGC2024	1342226735(6)	826	5×5
86	5:41:43.560	−1:53:28.42	NGC2024	1342227047(8)	830	8×8
89	5:42:27.680	−1:20:01.00	NGC2024	1342205220(1)	502	5×5
90	5:43:04.370	−1:16:11.60	NGC2024	1342228376(7)	849	8×8
91	5:46:06.690	−0:13:05.15	NGC2068	1342205218(9)	502	8×8
92	5:46:14.210	−0:05:26.84	NGC2068	1342205216(7)	502	5×5
93	5:46:40.830	+0:00:30.52	NGC2068	1342215363(4)	662	8×8
94	5:46:39.580	+0:04:16.61	NGC2068	1342228365(6)	848	5×5
302	5:46:28.320	+0:19:49.40	NGC2068	1342228374(5)	849	5×5
303	5:47:24.810	+0:20:59.68	NGC2068	1342227966(7)	843	8×8
96	5:47:08.970	+0:21:52.86	NGC2068	1342215587(8)	663	8×8
128	5:46:56.220	+0:23:42.41	NGC2068	1342218727(8)	703	8×8
301	5:45:53.590	+0:25:27.30	NGC2068	1342216450(1)	675	5×5
97	5:47:58.060	+0:35:30.12	NGC2068	1342227969(70)	843	8×8
98	5:47:31.850	+0:38:05.77	NGC2068	1342227971(2)	843	8×8
300	5:47:42.990	+0:40:57.50	NGC2068	1342205214(5)	502	5×5
0	5:54:15.240	+1:43:15.59	L1622	1342215365(6)	662	8×8
1	5:54:55.370	+1:45:03.08	L1622	1342218780(1)	704	8×8
3	5:54:23.540	+1:49:17.78	L1622	1342218703(4)	702	8×8
4	5:54:36.260	+1:53:54.00	L1622	1342218778(9)	704	8×8

NOTE. — Note: the ONC field contains the extended Orion Nebula region, the NGC1977 region, and OMC2/3; the NGC2024 field contains the NGC2024 HII region and the NGC2023 reflection nebula. The NGC2068 field includes the NGC2068 and NGC2071 reflection nebulae as well as LBS23 region.

<sup>a</sup> Field center coordinates.

TABLE 3  
*Herschel* PROTOSTAR CANDIDATE COORDINATES AND PHOTOMETRY

Source	group name	R.A. <sup>a</sup> h:m:s	Decl. <sup>a</sup> °:′:″	Field	24 $\mu$ m [mJy]	70 $\mu$ m [mJy]	160 $\mu$ m [mJy]	flag <sup>b</sup>	870 $\mu$ m detection <sup>c</sup>	T <sub>bol</sub> [K]	L <sub>bol</sub> [L <sub>☉</sub> ]
<b>061012</b>	061	05:42:48.87	−08:16:10.70	L1641	≤1.14	703±35	5634±845	1	...	32.1±0.9	0.75±0.06
<b>119019</b>	119	05:40:58.47	−08:05:36.10	L1641	1.46±0.2	1604±80.	10745±1612	1	Yes	34.4±0.8	1.56±0.14
026011	026	05:39:17.00	−07:24:26.64	L1641	≤1.30	78.4±3.9	2516±377	1	Yes	23.0±1.0	0.34±0.03
313006	313	05:39:30.75	−07:23:59.40	L1641	≤1.25	138±7.	2198±330	1	Yes	27.8±1.0	0.28±0.03
029003	029	05:39:13.15	−07:13:11.69	L1641	1.19±0.2	29.5±1.5	365±55	1	...	42.0±1.5	0.06±0.01
<b>019003</b>	019	05:35:23.92	−05:07:53.46	ONC	≤16.2	2506±127	31577±4737	1	Yes	33.6±1.1	3.16±0.31
<b>082005</b>	082	05:41:29.40	−02:21:17.06	NGC2024	≤3.13	506±25	9308±140	1	Yes	29.3±0.8	1.02±0.11
<b>082012</b>	082	05:41:24.94	−02:18:08.54	NGC2024	6.51±0.4	4571±229	51254±7688	1	Yes	32.2±0.9	6.27±0.65
<b>090003</b>	090	05:42:45.23	−01:16:14.18	NGC2024	4.74±0.3	3286±164	16937±2541	1	Yes	36.0±0.8	2.71±0.24
<b>091015</b>	091	05:46:07.65	−00:12:20.73	NGC2068	≤1.29	648±32	6615±992	1	Yes	30.9±0.8	0.81±0.07
<b>091016</b>	091	05:46:09.97	−00:12:16.85	NGC2068	≤1.14	431±22	5108±766	1	Yes	29.1±0.9	0.65±0.06
<b>093005</b>	093	05:46:27.75	−00:00:53.81	NGC2068	≤1.14	1427±71.	12131±1820	1	Yes	30.8±0.9	1.71±0.15
<b>302002</b>	302	05:46:28.24	00:19:27.00	NGC2068	≤1.14	302±15	7187±108	1	Yes	28.6±0.9	0.84±0.09
<b>097002</b>	097	05:48:07.76	00:33:50.79	NGC2068	≤1.14	1049±52.	7993±120	1	Yes	33.4±0.9	1.14±0.11
300001	300	05:47:43.36	00:38:22.43	NGC2068	≤7.19	478±24	5042±756	1	Yes	29.6±0.9	0.65±0.06
068006	068	05:41:11.79	−07:53:35.09	L1641	9.19±0.2	44.8±2.2	146±22	2	...	149.7±5.06	0.05±0.01
038002	038	05:36:11.11	−06:49:11.29	L1641	≤1.25	36.4±1.8	537±81	2	...	40.4±1.0	0.10±0.01
037003	037	05:37:00.35	−06:37:10.95	L1641	8.85±0.2	725±36	3798±570	2	...	53.1±1.7	0.43±0.03
037008	037	05:37:34.31	−06:35:20.33	L1641	≤1.39	27.7±1.4	321±48	2	...	45.5±1.9	0.04±0.01
092011	092	05:46:26.17	−00:04:45.31	NGC2068	2.31±0.2	77.8±3.9	363±54	2	...	104.1±5.63	0.05±0.01
093001	093	05:46:56.32	−00:03:14.73	NGC2068	≤1.14	21.8±1.1	217±33	2	Yes	47.9±0.7	0.05±0.01
302004	302	05:46:16.55	00:21:35.09	NGC2068	2.87±0.2	108±5.	283±42	2	...	54.8±1.8	0.07±0.01
096023	096	05:46:53.23	00:22:10.05	NGC2068	≤2.13	147±7.	1691±254	2	...	39.6±1.4	0.18±0.02
301003	301	05:46:02.15	00:23:29.86	NGC2068	8.08±0.2	42.6±2.1	231±35	2	...	92.1±3.8	0.05±0.01
000011	000	05:54:32.10	01:42:54.92	L1622	≤1.25	28.5±1.4	147±22	2	...	50.1±0.5	0.06±0.01
053002	053	05:43:24.07	−08:49:03.75	kOri	≤1.38	33.5±1.7	190±28	3	...	43.2±0.3	0.06±0.01
117004	117	05:41:40.40	−08:41:40.60	L1641	1.17±0.2	25.3±1.3	234±35	3	...	56.4±2.2	0.04±0.01
117014	117	05:41:29.28	−08:36:14.60	L1641	1.20±0.2	31.0±1.6	237±36	3	...	32.2±2.4	0.11±0.01
119016	119	05:40:40.54	−08:05:55.00	L1641	1.97±0.2	42.7±2.1	148±22	3	...	62.7±1.7	0.05±0.01
121011	121	05:41:37.90	−07:55:44.35	L1641	1.46±0.2	74.1±3.7	193±29	3	...	51.6±1.5	0.04±0.01
025044	025	05:39:56.80	−07:19:21.40	L1641	≤1.18	23.1±1.2	150±22	3	...	42.2±0.2	0.08±0.01
030013	030	05:38:59.58	−07:10:31.92	L1641	1.43±0.2	25.9±1.3	153±23	3	...	48.0±1.0	0.05±0.01
031003	031	05:38:55.35	−07:05:29.17	L1641	2.96±0.2	49.9±2.5	175±26	3	...	67.7±1.8	0.06±0.01
034010	034	05:37:54.76	−06:56:59.65	L1641	≤1.14	61.3±3.1	249±37	3	...	43.5±0.7	0.15±0.01
031037	031	05:38:28.20	−06:56:40.16	L1641	≤1.14	64.3±3.2	396±59	3	...	51.9±2.4	0.06±0.01
034014	034	05:38:14.92	−06:53:03.56	L1641	1.89±0.2	47.4±2.4	235±35	3	...	65.5±3.5	0.03±0.01
036003	036	05:38:05.97	−06:50:58.91	L1641	1.74±0.2	67.4±3.4	291±44	3	...	74.6±3.1	0.04±0.01
036006	036	05:37:45.07	−06:50:02.39	L1641	2.83±0.2	34.8±1.7	143±22	3	...	60.1±1.8	0.04±0.01
036011	036	05:37:42.72	−06:47:08.31	L1641	2.68±0.2	41.8±2.1	159±24	3	Yes	65.9±1.9	0.05±0.01
037011	037	05:37:37.80	−06:34:43.35	L1641	2.42±0.2	58.0±2.9	409±61	3	...	69.6±3.0	0.04±0.01
050006	050	05:34:23.01	−06:32:58.00	L1641	2.82±0.2	45.5±2.3	313±47	3	...	60.3±2.3	0.06±0.01
037013	037	05:37:22.00	−06:32:56.48	L1641	2.93±0.2	52.0±2.6	180±27	3	...	62.7±1.8	0.05±0.01
041001	041	05:36:28.68	−06:30:42.13	L1641	2.72±0.2	47.5±2.4	262±39	3	...	90.7±4.8	0.03±0.01
009001	009	05:33:32.55	−05:53:34.25	ONC	4.83±0.3	74.9±3.8	245±37	3	...	95.4±2.6	0.05±0.01
021010	021	05:34:19.63	−04:53:23.54	ONC	11.3±0.5	316±16	678±10	3	...	63.8±2.2	0.18±0.01
303017	303	05:47:49.01	00:20:26.47	NGC2068	4.64±0.2	107±5.	634±95	3	...	70.2±3.8	0.10±0.01
303023	303	05:47:45.58	00:21:14.68	NGC2068	4.36±0.2	65.9±3.3	234±35	3	...	104.1±4.81	0.04±0.01
098001	098	05:47:25.77	00:33:37.43	NGC2068	1.73±0.2	9.79±0.5	231±35	3	...	43.5±2.1	0.03±0.01
097003	097	05:47:45.88	00:34:12.71	NGC2068	1.37±0.2	13.0±0.7	137±21	3	...	78.1±4.4	0.02±0.01
000003	000	05:54:17.28	01:40:18.68	L1622	8.63±0.4	165±8.	386±58	3	...	82.5±3.3	0.10±0.01
000010	000	05:54:37.27	01:42:52.39	L1622	5.10±0.3	64.7±3.2	215±32	3	...	89.2±3.9	0.04±0.01
069001	069	05:40:46.20	−08:04:35.12	L1641	5.13±0.2	325±16	722±11	4	...	336.1±14.7	0.29±0.01
026001	026	05:39:18.49	−07:27:52.37	L1641	4.71±0.2	223±11	598±90	4	...	224.4±11.2	0.17±0.01
306004	306	05:35:24.66	−04:49:43.53	ONC	≤124	435±22	637±96	4	...	119.1±3.56	0.33±0.01
006006	006	05:35:11.47	−05:57:05.09	L1641	5.06±0.2	126±6.	4027±604	5	Yes	27.7±0.6	0.31±0.04

NOTE. — Note: the ONC field contains the extended Orion Nebula region, the NGC1977 region, and OMC2/3; the NGC2024 field contains the NGC2024 HII region and the NGC2023 reflection nebula. The NGC2068 field includes the NGC2068 and NGC2071 reflection nebulae as well as LBS23 region.

<sup>a</sup> PACS 70  $\mu$ m source coordinates.

<sup>b</sup> This column indicates if a source is flagged as a reliable protostar (value = 1), if the source is considered less likely be a protostar (value = 2), if the source is flagged as extragalactic contamination (value = 3), if the SED shape is with IRAC photospheric emission (value = 4), and finally, one source has no IRAC coverage (value = 5).

<sup>c</sup> This column indicates if the source has a strong 870  $\mu$ m detection; sources with no data are either assigned upper limits or have no coverage

TABLE 4  
*Spitzer* AND *Herschel* PHOTOMETRIC PROPERTIES OF PACS BRIGHT RED SOURCES

Source	HOPS group name	R.A. <sup>a</sup> h:m:s	Decl. <sup>a</sup> °:′:″	Field	24 $\mu$ m [mJy]	70 $\mu$ m [mJy]	100 $\mu$ m [mJy]	160 $\mu$ m [mJy]	log 70/24 <sup>b</sup>
061012	061	05:42:48.8	−08:16:10.70	L1641	≤1.14	703±35	2018±517	5634±845	≥2.31
119019	119	05:40:58.4	−08:05:36.10	L1641	1.46±0.2	1604±80.	5789±148	10745±1612	2.56
HOPS169	040	05:36:36.0	−06:38:54.02	L1641	4.80±0.5	5001±250	15753±4033	29975±4496	2.54
019003	019	05:35:23.9	−05:07:53.46	ONC	≤16.2	2506±127	4711±121	31577±4737	≥1.71
082005	082	05:41:29.4	−02:21:17.06	NGC2024	≤3.13	506±25	3003±769	9308±140	≥1.73
HOPS372	082	05:41:26.3	−02:18:21.08	NGC2024	12.0±1.2	6178±309	16217±4151	31090±4664	2.24
082012	082	05:41:24.9	−02:18:08.54	NGC2024	6.51±0.4	4571±229	20357±5211	51254±7688	2.37
090003	090	05:42:45.2	−01:16:14.18	NGC2024	4.74±0.3	3286±164	10914±2794	16937±2541	2.36
HOPS358	091	05:46:07.2	−00:13:30.86	NGC2068	422±42	60681±3041	104322±26706	123207±18481	1.68
091015	091	05:46:07.6	−00:12:20.73	NGC2068	≤1.29	648±32	2543±651	6615±992	≥2.22
091016	091	05:46:09.9	−00:12:16.85	NGC2068	≤1.14	431±22	1977±506	5108±766	≥2.10
HOPS373	093	05:46:30.7	−00:02:36.80	NGC2068	14.1±1.4	5258±263	20188±5168	36724±5509	2.10
093005	093	05:46:27.7	−00:00:53.81	NGC2068	≤1.14	1427±71.	5373±138	12131±1820	≥2.62
302002	302	05:46:28.2	00:19:27.00	NGC2068	≤1.14	302±15	3101±794	7187±108	≥1.95
HOPS359	303	05:47:24.8	00:20:58.24	NGC2068	22.8±2.3	20758±1039	43592±1116	60409±9061	2.48
HOPS341	128	05:47:00.9	00:26:20.76	NGC2068	14.0±1.4	3001±301	15138±3875	25213±3782	1.86
097002	097	05:48:07.7	00:33:50.79	NGC2068	≤1.14	1049±52.	4163±107	7993±120	≥2.49
HOPS354	000	05:54:24.1	01:44:20.15	L1622	28.9±2.9	8492±426	37423±9580	39258±5889	1.99

NOTE. — Note: the ONC field contains the extended Orion Nebula region, the NGC1977 region, and OMC2/3; the NGC2024 field contains the NGC2024 HII region and the NGC2023 reflection nebula. The NGC2068 field includes the NGC2068 and NGC2071 reflection nebulae as well as LBS23 region.

<sup>a</sup> Object coordinates are derived from the PACS 70  $\mu$ m images.

<sup>b</sup>  $\log \lambda F_{\lambda 70} / \lambda F_{\lambda 24}$

TABLE 5  
 APEX 350 AND 870  $\mu$ m PHOTOMETRY OF PACS BRIGHT RED SOURCES

Source	350 $\mu$ m [Jy beam <sup>−1</sup> ]	350 $\mu$ m <sup>a</sup> [Jy]	350 $\mu$ m <sup>b</sup> [Jy]	870 $\mu$ m [Jy beam <sup>−1</sup> ]	870 $\mu$ m <sup>a</sup> [Jy]	870 $\mu$ m <sup>b</sup> [Jy]
061012	2.60	3.93	2.53	≤0.7	≤1.3	≤1.3
119019	3.38	5.27	3.63	0.5	0.9	0.6
HOPS169	...	...	...	1.0	1.6	1.4
019003	8.29	19.6	7.18	2.5	5.0	3.0
082005	...	...	...	0.8	1.6	1.0
HOPS372	...	...	...	≤1.4	≤4.0	≤4.0
082012	...	...	...	2.7	4.3	3.6
090003	3.63 <sup>c</sup>	...	...	1.7	2.2	1.9
HOPS358	13.0	22.4	17.3	1.8	3.3	2.6
091015	2.14	3.15	2.26	0.6	1.3	0.5
091016	2.50	3.76	2.81	0.7	1.2	0.8
HOPS373	9.02	12.9	10.5	1.5	2.5	2.0
093005	6.58	10.1	6.74	1.4	2.6	1.6
302002	...	...	...	1.1	1.7	1.5
HOPS359	...	...	...	1.8	2.9	2.2
HOPS341	...	...	...	1.0	1.5	1.3
097002	...	...	...	0.6	0.9	0.8
HOPS354	13.8	25.9	18.7	1.5	2.7	2.2

<sup>a</sup> Source flux measured in an aperture with radius equal to  $1 \times \text{FWHM}$ , where the  $\text{FWHM} = 7.34''$  and  $19.0''$  at 350 and 870  $\mu$ m, respectively.

<sup>b</sup> Source flux measured in the same aperture as (a) but with local sky subtraction over radii equal to  $\{1.5, 2.0\} \times \text{FWHM}$ .

<sup>c</sup> 350  $\mu$ m point from Miettinen et al. (2012).

TABLE 6  
ORION PBRs OBSERVED PROPERTIES: DETECTIONS, ENVIRONMENT, AND PREVIOUS DETECTIONS

Source	R.A. h:m:s	Decl. °:':"	4.5 $\mu$ m detection	High incl. <sup>a</sup>	24 $\mu$ m detection	Note <sup>b</sup>	Selected references
061012	05:42:48.8	−08:16:10.7	yes	...	no	ns	...
119019	05:40:58.4	−08:05:36.1	yes	...	yes	f,i	...
HOPS169	05:36:36.0	−06:38:54.0	yes	yes	yes	f,i	Le88, Mo91, Za97, Da00, St02, Jo06, Nu07, Ba09, Me12
019003	05:35:24.0	−05:07:50.1	yes	...	no	f,c	Me90, Ch97, Ni03, Ts03, Nu07, Me12
082005	05:41:29.4	−02:21:17.1	no	...	no	f,i	La91, La96, Mo99, Jo06, Nu07
HOPS372	05:41:26.3	−02:18:21.1	yes	...	yes	f,ns	La91, La96, Mo99, Jo06, Nu07, Me12
082012	05:41:24.9	−02:18:08.5	no	...	yes	f,ns	La91, La96, Mo99, Wu04, Jo06, Nu07
090003	05:42:45.2	−01:16:14.2	yes	...	yes	i	Mi09
HOPS358	05:46:07.2	−00:13:30.9	yes	...	yes	f,c	St86, Li99, Re99, Mi01, Wu04, Nu07, Me12
091015	05:46:07.7	−00:12:19.1	no	...	no	f,ns	Li99, Mi01, Nu07
091016	05:46:10.0	−00:12:15.4	no	...	no	f,ns	Li99, Mi01, Nu07
HOPS373	05:46:30.7	−00:02:36.8	yes	...	yes	f,i	Ha83, La91, Gi00, Mo01, Mi01, Nu07, Me12
093005	05:46:27.7	−00:00:51.5	yes	...	no	f,i	La91, Mo01, Mi01, Nu07
302002	05:46:28.2	+00:19:28.4	yes	yes	no	f,ns	La91, Jo01, Ph01, Mo01, Sa03, Nu07
HOPS359	05:47:24.8	+00:20:58.2	no	...	yes	f,i	La91, Mo01, Nu07, Me12
HOPS341	05:47:00.9	+00:26:20.8	yes	yes	yes	b	Jo01, Mo01, Nu07, Sa10, Me12
097002	05:48:07.7	+00:33:52.7	no	...	no	b/ns	...
HOPS354	05:54:24.2	+01:44:20.1	yes	yes	yes	b	Re08, Ba09, Me12

NOTE. — Le88: Levreault (1988); Mo91: Morgan et al. (1991); ZA97: Zavagno et al. (1997); Da00: Davis et al. (2000); St02: Stanke et al. (2002); Da02: Davis et al. (2009); Nu07: Nutter & Ward-Thompson (2007) and (Di Francesco et al. 2008); Jo06: Johnstone & Bally (2006); Ts03: Tsujimoto et al. (2003); Ch97: Chini et al. (1997); Ni03: Nielbock et al. (2003); Me90: Mezger et al. (1990); Mo99: Mookerjee et al. (2009); La96: Launhardt et al. (1996); La91: Lada et al. (1991a); Wu04: Wu et al. (2004); Mi09: Miettinen et al. (2009); Re99 Reipurth et al. (1999); St86: Strom et al. (1986); Li99: Lis et al. (1999); Mi01: Mitchell et al. (2001); Mo01: Motte et al. (2001); Gi00: Gibb & Little (2000); Ha83: Haschick et al. (1983); Ph01: Phillips et al. (2001); Sa03: Savva et al. (2003); Jo01: Johnstone et al. (2001); Re08: Reipurth et al. (2008); Ba09: Bally et al. (2009); Sa10: Sadavoy et al. (2010); Me12: Megeath et al. (2012)

<sup>a</sup> Sources with indications of an observed high inclination orientation from the 4.5  $\mu$ m images.

<sup>b</sup> ns = nearby source and indicates that we find a source close ( $\lesssim 30''$ ) to the target; f = filament and indicates that a significant level of elongation or extended emission is seen in the 870  $\mu$ m data; i = isolated and indicates that no near-by source is observed; c = crowded, indicating that the source resides in region possibly with multiple sources, extended emission, or both and whose photometry may be affected by source blending; finally, b = binary, are sources that may have an unresolved secondary source and therefore blended photometry.

TABLE 7  
NUMBERS AND FRACTIONS OF NEW SOURCES AND RED PBRs FOUND  
BY REGION

Region	Field	Total number	New number	New %	PBRs number	PBRs %
All		355	56	16%	18	5%
Orion A		274	35	13%	4	1%
	L1641 <sup>a</sup>	200	31	16%	3	2%
	ONC	74	4	5%	1	1%
Orion B		81	21	26%	14	17%
	NGC2024	17	3	18%	4	24%
	NGC2068	52	15	29%	9	17%
	L1622	12	3	25%	1	8%

<sup>a</sup>  $\kappa$ Ori sources have been included here.

TABLE 8  
ORION PBRs AND COMPARISON CLASS 0 SOURCES: OBSERVED PROPERTIES AND MODIFIED BLACK-BODY FIT  
PARAMETERS

Source	$T_{\text{bol}}$ [K]	$L_{\text{bol}}$ [ $L_{\odot}$ ]	$L_{\text{smm}}/L_{\text{bol}}^a$ %	$T_{\text{MBB}}^b$ [K]	$L_{\text{MBB}}^b$ [ $L_{\odot}$ ]	$M_{\text{MBB}}^{b,c}$ [ $M_{\odot}$ ]	$\lambda_{\text{peak,MBB}}^b$ [ $\mu\text{m}$ ]
061012 <sup>d</sup>	32.1±0.9	0.75±0.06	3.1	19.2±0.4	0.68±0.07	0.20±0.04	133
119019	34.4±0.9	1.56±0.14	2.6	19.9±0.4	1.35±0.11	0.32±0.06	127
HOPS169	35.4±0.9	4.50±0.42	2.4	20.4±0.5	3.85±0.41	0.81±0.20	127
019003 <sup>d</sup>	33.6±1.1	3.16±0.29	1.1	21.4±0.8	1.52±0.30	0.24±0.18	121
082005 <sup>d</sup>	29.3±0.8	1.02±0.11	5.4	17.0±0.4	1.02±0.13	0.61±0.15	151
HOPS372	36.9±1.0	4.90±0.45	1.9	21.3±0.6	3.96±0.43	0.65±0.17	121
082012	32.2±0.9	6.27±0.65	3.8	18.6±0.4	5.89±0.71	2.20±0.52	139
090003	36.0±0.8	2.71±0.24	1.8	21.4±0.4	2.06±0.15	0.33±0.06	121
HOPS358	44.3±0.9	30.6±2.21	0.6	27.2±1.0	19.5±1.23	0.78±0.14	88.
091015 <sup>d</sup>	30.9±0.9	0.81±0.07	3.3	18.7±0.4	0.72±0.06	0.24±0.04	136
091016 <sup>d</sup>	29.1±0.9	0.65±0.06	4.1	17.9±0.3	0.61±0.06	0.26±0.05	142
HOPS373	36.0±0.9	5.20±0.48	2.3	20.2±0.4	4.21±0.32	0.93±0.16	127
093005 <sup>d</sup>	30.8±0.9	1.71±0.15	3.4	18.8±0.4	1.57±0.15	0.52±0.10	136
302002 <sup>d</sup>	28.6±0.9	0.84±0.10	6.1	16.2±0.3	0.82±0.11	0.63±0.15	157
HOPS359	39.3±0.9	12.6±1.00	1.3	23.4±0.7	9.56±0.84	0.91±0.23	115
HOPS341	36.3±1.1	3.62±0.37	3.1	19.1±0.5	3.16±0.35	0.97±0.24	133
097002 <sup>d</sup>	33.4±0.9	1.14±0.11	2.8	19.4±0.5	0.99±0.11	0.27±0.07	130
HOPS354	37.4±0.8	7.53±0.74	1.9	21.0±0.4	5.84±0.45	1.05±0.19	124
B 335 <sup>e</sup>	40.3±1.3	0.55±0.04	2.6	20.0±0.7	0.47±0.04	0.11±0.02	130
CB 130 <sup>e</sup>	55.2±3.3	0.22±0.01	10.9	12.7±0.5	0.17±0.01	0.55±0.11	199
CB 244-SMM1 <sup>e</sup>	63.2±2.6	1.72±0.14	1.8	20.3±0.8	1.10±0.11	0.24±0.04	127
CB 68 <sup>e</sup>	49.2±1.4	0.68±0.06	1.9	19.8±1.1	0.42±0.05	0.10±0.02	130
VLA1623-243 <sup>f</sup>	34.0±1.2	2.82±0.32	2.4	21.3±0.5	2.55±0.24	0.48±0.09	124

<sup>a</sup> Our  $L_{\text{smm}}/L_{\text{bol}}$  may be underestimated as the  $L_{\text{smm}}$  values are measured from the modified black-body fits to the SEDs (see text).

<sup>b</sup> Best-fit modified black-body parameters; the parameters shown here are derived from fitting the  $\lambda \geq 70 \mu\text{m}$  SED points. Excluding the  $70 \mu\text{m}$  point and fitting only the  $\lambda \geq 100 \mu\text{m}$  points systematically increases the derived masses by 20% on average, decreases the temperature by 5% on average, and decreases the luminosity by 7% on average.

<sup>c</sup> The masses derived here will increase by a factor of  $\sim 4$  if we assume an ISM-type dust model (Draine & Lee 1984). Furthermore, we assume a gas-to-dust ratio of 110 (see text).

<sup>d</sup> The values of  $T_{\text{bol}}$  and  $L_{\text{bol}}$  for these sources should be considered upper limits because we include the  $24 \mu\text{m}$  upper limits in our analysis for these sources.

<sup>e</sup> Additional well-studied isolated Class 0 sources from Launhardt et al. (2012) and Stutz et al. (2010) are shown for comparison; the distances to these sources lie between 100 pc and 250 pc.

<sup>f</sup> SED from J. Green and DIGIT team, private communication, 2012, and Green et al., in prep.